Titre: Title:	Metasurface Analysis Using Finite Difference Techniques
Auteur: Author:	Yousef Vahabzadeh Jamairan
Date:	2019
Type:	Mémoire ou thèse / Dissertation or Thesis
Référence: Citation:	Vahabzadeh Jamairan, Y. (2019). Metasurface Analysis Using Finite Difference Techniques [Thèse de doctorat, Polytechnique Montréal]. PolyPublie. https://publications.polymtl.ca/3921/

UNIVERSITÉ DE MONTRÉAL

METASURFACE ANALYSIS USING FINITE DIFFERENCE TECHNIQUES

YOUSEF VAHABZADEH JAMAIRAN
DÉPARTEMENT DE GÉNIE ÉLECTRIQUE
ÉCOLE POLYTECHNIQUE DE MONTRÉAL

THÈSE PRÉSENTÉE EN VUE DE L'OBTENTION
DU DIPLÔME DE PHILOSOPHIÆ DOCTOR
(GÉNIE ÉLECTRIQUE)
JUIN 2019

UNIVERSITÉ DE MONTRÉAL

ÉCOLE POLYTECHNIQUE DE MONTRÉAL

Cette thèse intitulée :

METASURFACE ANALYSIS USING FINITE DIFFERENCE TECHNIQUES

présentée par: VAHABZADEH JAMAIRAN Yousef
en vue de l'obtention du diplôme de: Philosophiæ Doctor
a été dûment acceptée par le jury d'examen constitué de :

M. LAURIN Jean-Jacques, Ph. D., président
M. CALOZ Christophe, Ph. D., membre et directeur de recherche
M. SEBAK Abdel Razik, Ph. D., membre
Mme POPOVICH Milica, Ph. D., membre externe

DEDICATION

À tous mes amis du labos,
vous me manquerez...

ACKNOWLEDGEMENTS

I would like to express my sincere gratitude to my supervisor Prof. Christophe Caloz for his continuous support and motivation. I dedicate all my success and achievements to his exceptional support and advise. I also highly appreciate him for his patience. It happened a lot that I missed his comments when preparing documents and doing my projects, but he kindly renotified to me.

I acknowledge so much the jury members, Prof. Jean Jacques Laurin, Prof. Abdel Razik Sebak and Prof. Milica Popovic for their precious time and comments.

Many thanks to the people I had collaboration during these years, including Dr. Karim Achouri, Dr. Nima Chamanara, Guillaume Lavigne, Ashutosh Patri, Dr. Luzhou Chen, Cespedes Vincente Oscar, Dr. Alireza Akbarzadeh, Xiaoyi Wang, Xiao Jia and all others who helped me to accomplish this work.

RÉSUMÉ

Les métasurfaces sont des structures très minces par rapport à la longueur d'onde de fonctionnement et des dimensions des métamatériaux tridimensionnels. Ils sont réalisés par la juxtaposition de cellule-unitaire en dessous de la longueur d'onde. Tout en étant légers et offrant moins de pertes, ils offrent une gamme d'applications plus étendue que les métamatériaux 3D classiques. Étant capables de modifier l'amplitude, la polarisation, la phase et la fréquence des ondes, leurs applications vont des fréquences radio aux optiques dans la formation de faisceaux, radômes, capes, lentilles, structures non réciproques et hologrammes, pour n'en nommer que quelques-uns.

En général, les métasurfaces sont des structures bianisotropes, qui, par le fait même, présentent des discontinuités spatiales et temporelles très complexes. Leur synthèse est basée sur les conditions généralisées de transition de feuille (GSTC) qui sont calculées à l'aide de la théorie de la distribution. Suivant cette théorie, ils sont modélisés comme une structure d'épaisseur nulle. Cependant, dans le calcul des particules diffusantes, l'utilisation des paramètres S ou des matrices d'impédance permet de les cartographier dans des inclusions de cellules unitaires appropriées avec une dimension inférieure à longueur d'onde. La bianisotropie et l'épaisseur nulle impliquent une discontinuité à la fois des champs électriques et magnétiques qui est connues sous le nom de problème général de discontinuité électromagnétique. Cela rend donc leur analyse très compliquée et impossible à faire avec les techniques numériques conventionnelles. Par conséquent, ce manuscrit traitera du manque significatif de méthode d'analyse précise et entièrement numérique.

Dans cette thèse, nous effectuons un examen approfondi des conditions aux limites classiques et discutons de leurs limites et de leurs conditions d'applicabilité. Les GSTC sont dérivés, et leur utilité est discutée. Ensuite, nous développons des techniques de calcul dans le schéma des différences finies (FD) pour l'analyse de discontinuité électromagnétique générale. Nous prouvons que les techniques numériques développées pour discontinuité simple, discontinuité du champ électrique ou magnétique, constituent un cas particulier de notre développement. Les formulations sont effectuées dans les domaines temporel et fréquentiel et sont étendues au cas général des métasurfaces dispersives, bianisotropes, variant dans le temps et l'espace. Nous présentons l'interprétation physique des équations dérivées. À chaque chapitre, nous étendons la méthode du chapitre précédent et le prouvons par de nombreux exemples illustratifs, dans lesquels les résultats sont comparés aux solutions analytiques, aux champs spécifiés ou au résultat approximatif du logiciel de simulation.

ABSTRACT

Metasurfaces are very thin structures compared to the operating wavelength and dimensional reduction of three-dimensional metamaterials. They are realized by the juxtaposition of sub-wavelength scattering particles. While being lightweight and less lossy, they offer a broader range of applications than the conventional 3D metamaterials. Being capable of altering the wave amplitude, polarization, phase, and frequency, their application range from radio frequencies to optics in beam-forming, radomes, cloaks, lenses, non-reciprocal structures, and holograms, to name a few.

In general, metasurfaces are bianisotropic structures, thus, representing very complex spatial and temporal discontinuity. Their synthesis is based on the generalized sheet transition conditions (GSTCs), which is calculated using distribution theory. As a result of this theory, they are modeled as a zero thickness structure. However, in the calculation of the scattering particles, using S-parameters or impedance matrices, they are mapped into proper unit-cell inclusions with sub-wavelength dimension. Bianisotropy and zero thickness imply discontinuity on both electric and magnetic fields, which is known as the general electromagnetic discontinuity problem. This consequence makes their analysis very complicated and undoable using conventional numerical techniques. Consequently, there has been a significant lack of an accurate and fully-numeric analysis method, which is covered by this manuscript.

In this thesis, we perform an in-depth review of the classical boundary conditions and discuss their limitations and conditions of applicability. GSTCs are derived and their usefulness is discussed. Then, we develop computational techniques in Finite Difference (FD) scheme for the analysis of the general electromagnetic discontinuity. We prove that the numerical techniques developed for the simple discontinuity, only electric field or magnetic field discontinuity, is a particular case of our development. The formulations are performed in both of the time and frequency domains and extended to the general case of dispersive, bianisotropic, space-time varying metasurfaces. We present the physical interpretation of the derived equations. At each chapter, we extend the method of the previous chapter and prove them by numerous illustrative examples, where the results are compared with the analytic solutions, specified fields or the approximate result of simulation software.

TABLE OF CONTENTS

LIST OF TABLES

LIST OF FIGURES

LIST OF SYMBOLS AND ACRONYMS

SYMBOLS

c_0	speed of light in free-space
λ	Wavelength
λ_0	Free-space wavelength
f	frequency
k_0	free-space wavenumber
η_0	free-space intrinsic impedance
μ_0	free-space magnetic permeability
μ_r	magnetic permeability
ε_0	free-space permittivity
ε_r	Dielectric constant
Δt	Time step
Δx	Space step in x direction
χ_{ee}	Electric susceptibility tensor
χ_{mm}	Magnetic susceptibility tensor
χ_{em}	Electro-magnetic susceptibility tensor
χ_{me}	Magneto-electric susceptibility tensor

ACRONYMS

BC	Boundary Condition
FD	Finite Difference
TF	Total-Field
SF	Scattered-Field
TFSF	Total-Field Scattered-Field
FDTD	Finite Difference Time Domain
FDFD	Finite Difference Frequency Domain
FEM	Finite Element Method
MoM	Method of Moment
IE	Integral Equation
SDIE	Spectral Domain Integral equation
IBC	Impedance Boundary Condition

FSS	Frequency-Selective Surface
STC	Sheet Transition Condition
GSTCs	Generalized Sheet Transition Conditions
PEC	Perfect Electric Conductor
ADE	Auxiliary Differential Equation
PLRC	Piece-wise Linear Recursive Convolution
PMC	Perfect Magnetic Conductor
PEMC	Perfect Electromagnetic Conductor
TC	Transition Condition
DNG	Double Negative Material
PML	Perfectly Matched Layer
PBC	Periodic boundary Condition

LIST OF APPENDICES

CHAPTER 1 INTRODUCTION

In this chapter, we start with the classification of different materials based on their electromagnetic properties. Then, we discuss a brief history of metamaterials and the demands that led to the emergence of metasurfaces. Next, the objectives and motivations of the thesis are presented. Finally, the contribution and organization of the thesis are discussed.

1.1 Background on Metamaterials and Metasurfaces

It is known that every material is composed of atoms which determine its behavior when illuminated by an electromagnetic wave. Depending on the atoms configuration and type, different interactions may occur, such as reflection and refraction from dielectrics or absorption in magnetic materials under particular conditions. To pave the way to predict and understand these phenomena and exploit them to create novel structures, macroscopic quantities such as relative electric permittivity (ε_r) and relative magnetic permeability μ_r are defined and used in electromagnetics. A classification of the materials based on their macroscopic electromagnetic characteristics, i.e. ε_r and μ_r, is shown in Fig. 1.1. Macroscopic description of the materials provides a simplified homogeneous model without getting into the complicated details of the atoms and molecules configuration and properties.

Materials with $\varepsilon_r > 0$ and $\mu_r > 0$, such as glass, are vastly available in nature, known as double positive materials (DPM). Materials with only $\varepsilon_r < 0$ or $\mu_r < 0$ are also naturally available. For example, the dielectric constant of a plasma medium $\varepsilon_r = 1 - \frac{\omega_0^2}{\omega^2}$, where ω is the angular frequency, shows $\varepsilon_r < 0$ below the plasma frequency ω_0 [8]. Antiferromagnetic salts such as CoF_2 and FeF_2 [9] have negative μ_r. Note that the causality deduced from Kramers-Kronig relation should be valid for any ε and μ to be physical [10, 11].

However, the materials with both $\mu_r < 0$ and $\varepsilon_r < 0$, which are known as double negative (DNG) materials, cannot be found naturally. The main property of these materials is the antiparallel group and phase velocity, which was noted by Horace Lamb at the early 20th century [12], but its physical realization was thought to be impossible. Although, later on, negative permittivity and permeability were observed in the study of crystals and excitons by many research groups [13–15], however, the primary theoretical foundation for these materials was constructed later on by V.G. Veselago's paper on 1967 [16]. He proposed *negative index* or *left-handed* materials and its first realization was made using the split ring resonators [17,18]. Its unit-cells are significantly small compared to the operating wavelength, and they mimic

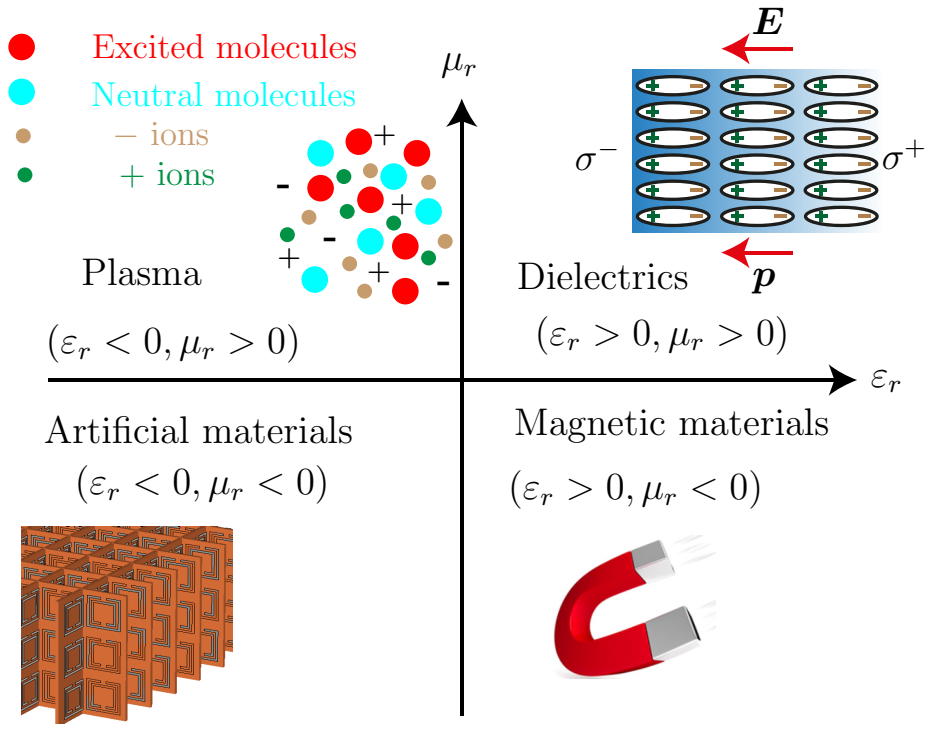

Figure 1.1 Materials classification based on their dielectric permittivity (ε_r) and magnetic permeability μ_r.

nature's atom on a larger scale.

Realization of these materials was a challenge initially. The main reason was the lack of fast computing technology to perform the required simulations. Secondly, all negative index materials should be dispersive [16]. This stems from the positive value condition on the total energy. For the materials without frequency dispersion, the total energy is

$$\tilde{W} = \varepsilon|\tilde{\boldsymbol{E}}|^2 + \mu|\tilde{\boldsymbol{H}}|^2, \tag{1.1}$$

where $\tilde{\boldsymbol{E}}$ and $\tilde{\boldsymbol{H}}$ are the electric and magnetic fields in the frequency domain, respectively. Throughout this thesis, the bold face font will indicate a vector and the operator $\sim$ will be used for the frequency domain quantities. Thus, ε and μ cannot be negative simultaneously as it leads to $0 > \tilde{W}$. For the frequency dispersive materials, the energy W in (1.1) will be

$$\tilde{W} = \frac{\partial\,(\varepsilon\omega)}{\partial\omega}|\tilde{\boldsymbol{E}}|^2 + \frac{\partial\,(\mu\omega)}{\partial\omega}|\tilde{\boldsymbol{H}}|^2, \tag{1.2}$$

where ω is the angular frequency. In this equation, the $\tilde{W} > 0$ condition implies $\frac{\partial(\varepsilon\omega)}{\partial\omega} > 0$

and $\frac{\partial(\mu\omega)}{\partial\omega} > 0$. These requirements made creating such materials challenging. With the advent of fast computers and gradual improvement of the researcher's understanding from the physics of negative index materials, these limitations were obviated about 33 years after the introduction of the negative index materials.

The term metamaterials coined by Rodger Walser [19, 20] which means the materials with behaviors unavailable in nature [21]. As shown in Fig. 1.1, metamaterials are double negative structures, where the electric permittivity and magnetic permeability are negative simultaneously. These three dimensional artificial materials have numerous applications such as, for example, magnetless non-reciprocal materials [22], electromagnetic cloaks [23, 24], dispersion control [25–27] antenna miniaturization [28].

In spite of many advantages and benefits of the metamaterials, their fabrication is challenging, which makes it costly, and requires long analysis time. This complexity in fabrication is due to the bianisotropic ε and μ, consequently 3D structures as shown in Fig. 1.2, requirement in the metamaterial design [29]. Although techniques have been developed to ease their fabrication [30], still the 3D fabrication complexity and scalability regarding mass production are the biggest challenges [31]. Another challenge is the metamaterials loss, significantly limiting their practical applications [32, 33]. Therefore, 2D planar structures developed to tackle these issues.

Numerous planar structures have been developed with increased functionality and reduced complexity compared to the metamaterials, some of them even preceding metamaterials but with limited functionalities and doing simple operations. The concept of reflection and transmission from simple periodic metallic strips [34] and patches [35], frequency selective surfaces [36, 37] and transmit arrays [38–40] and reflect arrays [41, 42] are a few examples.

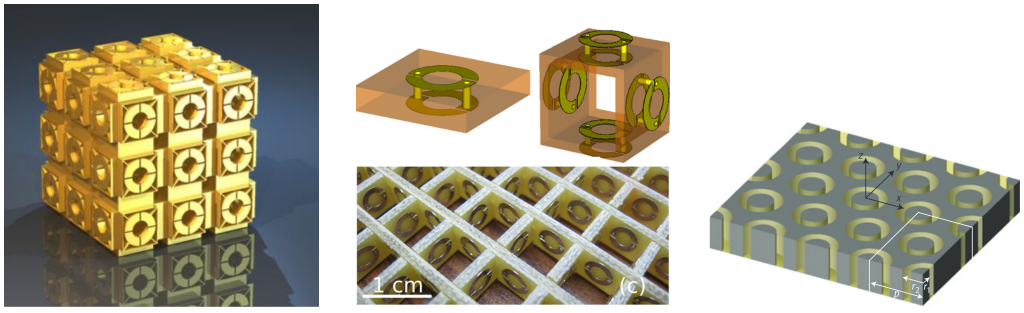

(a) (b) (c)

Figure 1.2 Examples of three dimensional metamaterials. (a) Intra-connected cubic-symmetry isotropic metamaterial [1]. (b) Split-ring resonator chiral metamaterial [2]. (c) Hexagonal array of coaxial waveguide [3].

These structures enable modification of phase, amplitude, and polarization of its incident wave. Metasurfaces, shown in Fig. 1.3, are also planar 2D structures, but with even more functionalities and physical insight compared to the mentioned 2D structures, and significantly reduced complexity compared to the 3D metamaterials. They exhibit arbitrary bianisotropy represented by four 3×3 surface susceptibility tensors which may vary both in space and time. These surface susceptibility tensors, $\bar{\bar{\chi}}_{\rm ee}$, $\bar{\bar{\chi}}_{\rm mm}$, $\bar{\bar{\chi}}_{\rm me}$ and $\bar{\bar{\chi}}_{\rm em}$, are the $\bar{\bar{\epsilon}}$, $\bar{\bar{\mu}}$, $\bar{\bar{\zeta}}$ and $\bar{\bar{\xi}}$ counterparts of the conventional bulky materials, respectively, [43]. The fact that makes metasurfaces unique compared to the other conventional electromagnetic structures is that they are modeled as a zero thickness sheet satisfying a particular boundary condition [44,45]. It is clear that for any set of incident, reflected and transmitted waves there are surface currents determined by the electromagnetic boundary condition requirements [46,47]. Since these currents may have different phases and amplitudes in different directions, a metasurface is bianisotropic in general. The majority of the designed metasurfaces in the literature are periodic, however, as we will see later, this is not correct in general.

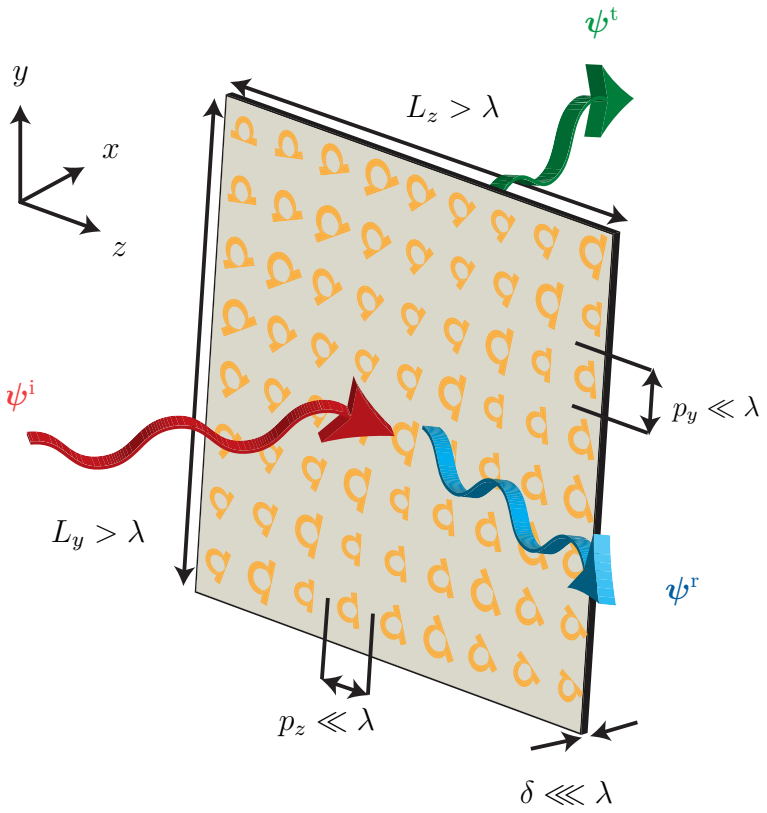

Figure 1.3 A metasurface, composed of subwavelength unit-cells with negligible thickness, transforming an incident wave $\boldsymbol{\psi}^{\rm i}$ into a reflected wave $\boldsymbol{\psi}^{\rm r}$ and a transmitted wave $\boldsymbol{\psi}^{\rm t}$.

The general law of reflection and refraction [48–50] surpassed the conventional accumulation

phase shift technique by introducing gradient of phase discontinuity along an interface, thus, replacing the traditional phase accumulated bulky structures with phase gradient metasurfaces. However, in many applications, along with the phase, other incident field characteristics should be modified as well to achieve the desired transmitted and reflected fields. Therefore, generalized sheet boundary condition (GSTC) [44–46] is used to develop a homogenized bianisotropic susceptibility tensor model for the metasurfaces [51–53]. Alternative models based on impedance and polarizability have also been developed [54–59]. The later models, useful only for normal excitations, are deductible from the GSTC model and they provide less physical insight into the problem and properties of the required metasurface such as, for example, loss, gain, ε and μ variation.

As a result of being low loss, low profile structure and advanced design techniques, metasurfaces have been investigated vastly within a decade. This amount of research brought numerous applications from RF to optics, where some of them were thought to be impossible just a few years ago. They are used in the design of wide-band miniaturized antennas [60,61], holograms [62–64], lenses [65,66], cloaks [67,68], orbital angular momentum generation [69–71] and beam-forming [72,73], to name a few.

1.2 Motivation and Objectives

Due to the aforementioned unique properties of the metasurfaces, it is a challenge to model them. In general, a metasurface design procedure is composed of two operations, namely synthesis and analysis, as shown in Fig. 1.4. The synthesis consists of two major sub-operations: First, extracting the metasurface susceptibilities, $\overline{\overline{\chi}}(x,y)$, using developed models [① in Fig. 1.4]. Second, realizing $\overline{\overline{\chi}}(x,y)$ and making a physical structure, [② in Fig. 1.4]. The analysis, which is the opposite of the synthesis, consists in determining the reflected and transmitted fields and it can be decomposed in two complementary operations. The first operation is the calculation of the surface susceptibility tensor functions $\overline{\overline{\chi}}(x,y)$ from a physical metasurface [③ in Fig. 1.4]. The second operation is the succeeding computation of the scattered fields [④ in Fig. 1.4] [74,75]. The surface susceptibility of a realized metasurface can be obtained numerically by calculating S-parameters of each cell or a few juxtaposed cells making a super-cell [76] and, then, converting them into corresponding surface impedance or susceptibility tensors following the details in [77–79]. This thesis deals with the last [④] of the analysis operations, which is important for the synthesis operation as well and provides deep insight into the physics of the metasurfaces. Note that a significant problem of analysis remains unaddressed and the available commercial softwares are not useful, as will be elaborated upon in the following chapter. This is due to the metasurfaces unique features such

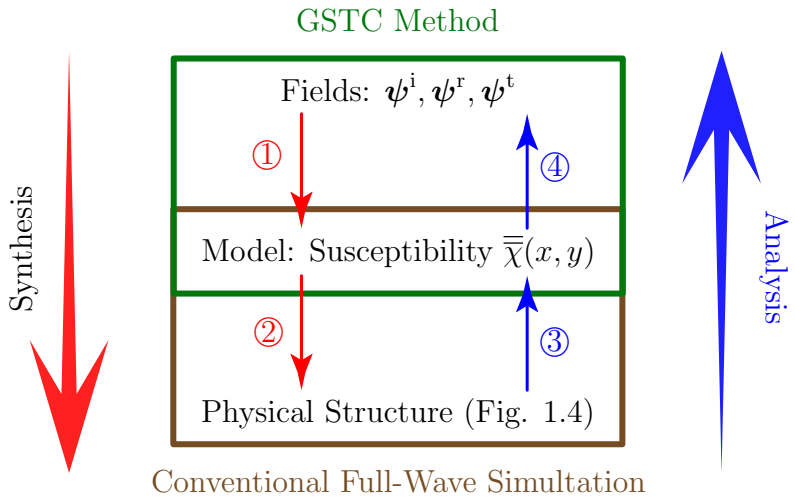

Figure 1.4 Metasurface holistic design.

as zero-thickness, introduction of a general discontinuity on the electromagnetic fields and a very complex relation between the electric and magnetic fields.

The GSTC, which is perfect for the metasurface synthesis, does not provide complete metasurface analysis tool. For example, for a metasurface in the presence of a scatterer, not only the GSTC but the commercial software and developed techniques are unable to simulate them. Other research groups have proposed methods for the metasurface analysis, however, they have used slab approximation, which is not accurate and will be discussed in the next chapter. Moreover, their method does not support surface wave propagation and is usually applied to only transmitting or only reflecting metasurfaces.

Therefore, our primary objective is to develop analysis tools in finite-difference frequency-domain (FDFD) and finite-difference time-domain (FDTD) schemes for any given metasurface susceptibilities and excitations by integrating GSTCs with them. Our developed GSTC-FDFD technique is capable of simulating any dispersive and non-linear metasurfaces at a single frequency. The GSTC-FDTD is multi-chromatic and can be used in the simulation of any space-time varying, dispersive and non-linear metasurface.

The selection of the time or frequency domain technique depends on the problem type. Having only the frequency domain or time domain solution, it is possible to use Fourier transform and obtain the solution in the other domain. However, this is not an efficient solution unless in the particular condition of single frequency excitation, non-dispersive and time invariant metasurface. FDFD is the best choice for a dispersive metasurface under

monochromatic excitation. For the broadband and transient-time simulations, time domain techniques should be selected. This is due to the unavailability of the transient-time data in the frequency domain simulations.

Moreover, the solution in multiple frequencies requires a repeated calculation for each frequency using FDFD and usually a large matrix inversion at each iteration. For the monochromatic analysis, because of the march-on-time nature of the time-domain techniques, they require more simulation time, while, frequency domain techniques can provide the solution in a single run. For the resonator problems, the frequency domain techniques are the best selection because in time-domain long simulation time is needed for the steady-state solutions. Finally, a time-varying metasurface analysis obviously requires a time-domain technique.

1.3 Thesis Contribution and Organization

The contribution of this thesis is the introduction of novel computational schemes, both in the frequency domain and in the time domain, for the analysis of a general metasurface [1] by introducing the concept of virtual nodes and grafting GSTC equations into conventional computationl algorithms. Since the frequency domain formulation of the Maxwell equations, does not include time derivations, thus, they are simplified. For this reason, we first develop a GSTC-FDFD technique for the simulation of bianisotropic and dispersive metasurfaces. Then, we generalize our method into the time domain to simulate any space-time varying but non-dispersive metasurfaces by introducing the virtual node concept in this domain. This is not straight-forward due to the staggered nature of the Yee-grid both in space and time. We prove that the GSTC-FDTD is the generalization of the conventional FDTD technique that is used for the simulation of bulk materials. Finally, we will make a complete development by introducing dispersion in the time domain equations. With the later development, one can simulate any bianisotropic dispersive space-time varying metasurface. We also demonstrate that the resulted field update equations are generalization of the classical computational methods and conventional approximate schemes used for the simulation of metasurfaces.

The contribution of our developed model-based analysis, [④] in Fig. 1.5, are the following [4]:

- Fig 1.5a: For a synthesized metasurface, [①], ④ allows the designer to verify the metasurface functionality by comparing the specified fields with the resulted fields from the analysis. Moreover, it enables the metasurface characterization for the parameters other than the specified ones, for example, illumination angle, frequency, and polarization, waveform of the incident wave and metasurface size.

[1] A general metasurface is a bianisotropic, dispersive and space-time varying.

- Fig 1.5b: It allows iterative synthesis-analysis procedure toward an efficient design. For instance, if the outcome of ① does not fulfill the expectations (e.g. undesired scattered fields under different illumination, high loss, unpractical susceptibilities, electrically fast varying S-parameters, active synthesis, etc.), ④ allows an alternative design by adjusting the design specifications (e.g. from monoisotropic to bianisotropic [80], etc.). Once the result of this iterative procedure is found satisfactory, the physical realization [②] begins.

- Fig 1.5c: ④ is also useful when characterizing a metasurface for the parameters other than the specified ones based on the extracted susceptibility parameters of a physically known metasurface. Except for the highly spatial dispersive metasurfaces, this will reduce the simulation complexity significantly as only susceptibility tensors are used in the simulation instead of a complex physical structure.

- Fig 1.5d: When scattering objects co-exist with the metasurface, it accelerates the analysis and eliminates the extra burden that could be caused by the metasurface. This advantage will be noticeable in an iterative synthesis-analysis procedure of Fig 1.5b.

The organization of this thesis is as follows:

Chapter 2 is the literature review. We introduce different forms of electromagnetic boundary condition (BC) and recall GSTC BC. The differences between the GSTC and sheet transition condition (STC) is also discussed, and we show that GSTC is the most general form of BC. Then, different metasurface synthesis techniques and calculation of unit-cell shapes are presented. Finally, early metasurface analysis techniques and their limitations are discussed.

GSTC-FDFD is discussed in Chapter 3, where the concept of the virtual node is introduced and applied to the 1D and 2D FDFD problems. Then, our development is proved by many illustrative examples, and the results are compared with COMSOL and analytical solutions. We have skipped the 3D formulation as it is straightforward but tedious and results in long equations.

Chapter 4 discusses GSTC-FDTD technique and virtual node concept in the time domain by performing the formulation in 1D and 2D FDTD grids. This section is followed by the physical interpretation of the resulted equations. Finally, five illustrative examples are used for the benchmark.

The most general formulation of the GSTC-FDTD is given in Chapter 5. In this chapter, we enhance the GSTC-FDTD capabilities for the simulation of space-time varying, dispersive and bianisotropic metasurfaces, thus, filling the gap between frequency domain and time

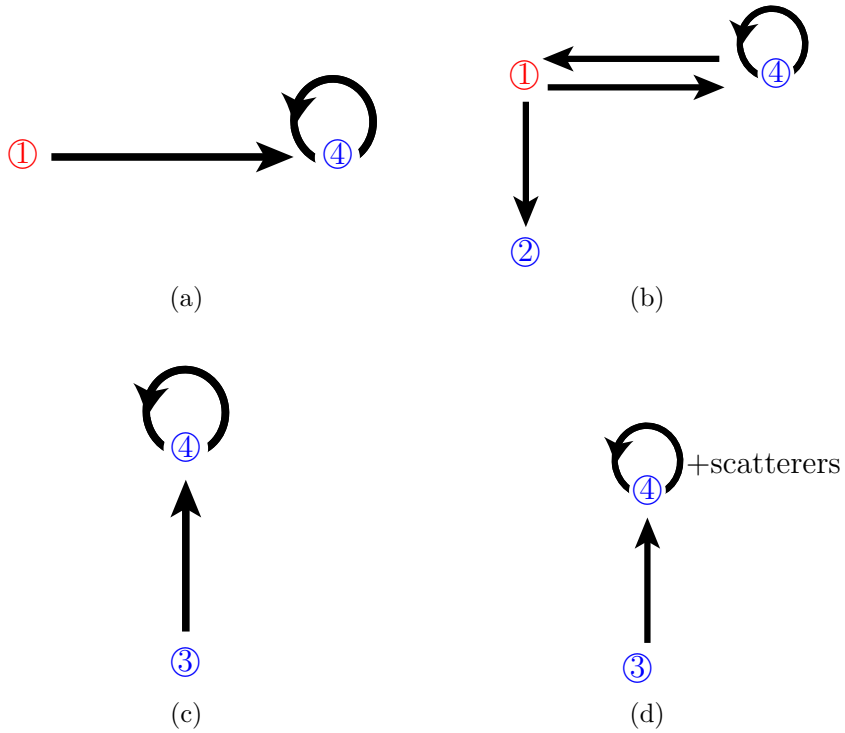

Figure 1.5 Contribution of our model-based analysis [④ in Fig. 1.4]. (a) Synthesis verification and characterization. (b) Synthesis by synthesis-analysis iterations. (c) Analysis and characterization from extracted susceptibilities. (d) Same as (c) but in the presence of scatterers [4].

domain techniques in the previous chapters and making a complete metasurface analysis tool. In this chapter, we present four illustrative examples to prove the applicability and robustness of our technique.

Finally, we draw a conclusion in Chapter 6 and discuss the limitations and possible future works on the topic.

CHAPTER 2 LITERATURE REVIEW

In this chapter the electromagnetic BCs and their applicability conditions are discussed. We will show that GSTCs is the generalization of the conventional BCs. Then, we discuss different metasurface synthesis techniques and a brief overview of the physical realization of its mathematical model. Finally, we review the literature on the metasurface analysis and discuss their limitations.

2.1 Classical Electromagnetic Boundary Conditions

It is well known that the fields everywhere inside a perfectly electric conductor (PEC), $\sigma_{\mathrm{e}} \to \infty$, is zero ($\mathbf{E}_{\mathrm{PEC}} = 0$), where $\mathbf{E}$ is a vectorial electric field. From this and the continuity of the tangential electric field ($\mathbf{E}_{\mathrm{t}}$) at the interface of any two media, $\boldsymbol{E}_{\mathrm{t}} = 0$ can be inferred at the interface of a PEC and any material [1], which is the simplest electromagnetic BC. The duality theorem [81, 82] exhibits that the tangential component of the magnetic field is zero ($\mathbf{H}_{\mathrm{t}} = 0$) on a perfect magnetic conductor [2] (PMC), $\sigma_{\mathrm{m}} \to \infty$.

The aforementioned BC is particular form of the general Leontovich BC [85, 86]. Leontovich BC is a classical BC that corresponds to the discontinuity created by juxtaposition of two different media. Assuming $\hat{\boldsymbol{x}}$ is the unit vector perpendicular to the interface, they are determined from the Maxwell equations as [87]

$$\hat{\boldsymbol{x}} \times \Delta \boldsymbol{H} = \boldsymbol{J}_{\mathrm{s}}, \tag{2.1a}$$

$$\Delta \boldsymbol{E} \times \hat{\boldsymbol{x}} = \boldsymbol{K}_{\mathrm{s}}, \tag{2.1b}$$

$$\hat{\boldsymbol{x}} \cdot \Delta \boldsymbol{D} = \rho_{\mathrm{s}}^{\mathrm{e}}, \tag{2.1c}$$

$$\hat{\boldsymbol{x}} \cdot \Delta \boldsymbol{B} = \rho_{\mathrm{s}}^{\mathrm{m}}, \tag{2.1d}$$

with $\boldsymbol{J}_{\mathrm{s}}$, $\boldsymbol{K}_{\mathrm{s}}$, $\rho_{\mathrm{s}}^{\mathrm{e}}$ and $\rho_{\mathrm{s}}^{\mathrm{m}}$ are the surface electric current, surface magnetic current, surface electric charge and surface magnetic charge densities, respectively, impressed on the interface. The operator Δ denotes the fields difference on both sides of the interface, $\Delta\psi = \psi^{\mathrm{t}} - (\psi^{\mathrm{i}} + \psi^{\mathrm{r}})$ with ψ any component of the $\boldsymbol{E}$ or $\boldsymbol{H}$ fields and t, i and r the transmitted, incident and reflected fields, respectively.

[1] Otherwise, $\boldsymbol{E}_{\mathrm{t}} \neq 0$ will cause an electric potential on the PEC surface. This, in turn, creates a surface current to neutralize the electric potential, which will lead to $\boldsymbol{E}_{\mathrm{t}} = 0$ in the steady-state.

[2] A PMC does not exist naturally. However, it can be constructed artificially using, for example, mushroom unit-cells [83, 84].

Applying Stokes theorem along the path of a closed contour across the interface gives (2.1a) and (2.1b) and Gauss theorem, also known as the divergence theorem, over the surface area of a volume containing the interface of the two media gives (2.1c) and (2.1d).

As pointed out by Schelkunoff [88], these conventional BCs are not rigourously applicable to an interface supporting currents and charges. To clarify this point, consider (2.1c), for example. We assume $\rho_{\mathrm{e}}^{s} = \delta(x)$, i.e. non-zero surface electric charges at the interface. This implies discontinuity of $\boldsymbol{D}$ and it is in contrast with the Gauss theorem [Fig. 2.1], which requires continuity of its integrand and its first order derivative. Same argument holds for other BCs in (2.1) and Stokes theorem [Fig. 2.1]. Therefore, equation (2.1) is applicable everywhere except at $x = 0$. On the other hand, in the absence of sources on the surface, $\boldsymbol{D}$ is continuous and it cannot take into account the effect of excitable dipoles or higher-order multipoles on the interface. However, a sheet discontinuity is modeled by surface electric and magnetic currents and, in general, they include higher order mulipoles[3]. Consequently, classical BCs cannot properly describe a sheet discontinuity. Therefore, transition conditions (TCs) are developed.

Transition conditions, such as impedance boundary condition (IBC) or admittance boundary condition (ABC), are used to mathematically model subwavelength structures such as frequency selective surfaces [37], coating films [89] and two-dimensional materials (graphene, black phosphorous, electron gas sheets, etc.) [7, 90–93]. These models take different forms depending on the structure and the computation method.

Penetrable surfaces, such as conducting dielectric coated bodies, can be modeled as IBC or ABC [94, 95]. The mathematical representation of these BCs are [96]

$$\mathbf{E}_{\mathrm{t}} = \overline{\overline{\mathbf{Z}}}_{\mathrm{s}} \bullet (\hat{n} \times \mathbf{H}) \,, \tag{2.2a}$$

$$\mathbf{H}_{\mathrm{t}} = \overline{\overline{\mathbf{Y}}}_{\mathrm{s}} \bullet (\hat{n} \times \mathbf{E}) \,, \tag{2.2b}$$

respectively, with $\hat{n}$ the normal outward unit vector of the interface. $\overline{\overline{\mathbf{Z}}}_{\mathrm{s}}$ and $\overline{\overline{\mathbf{Y}}}_{\mathrm{s}}$ are 2×2 surface impedance and admittance, respectively, satisfying $\hat{n} \bullet \overline{\overline{\mathbf{Z}}}_{\mathrm{s}} = \hat{n} \bullet \overline{\overline{\mathbf{Y}}}_{\mathrm{s}} = 0$ and $\overline{\overline{\mathbf{Z}}}_{\mathrm{s}} = \overline{\overline{\mathbf{Y}}}_{\mathrm{s}}^{-1}$ relations. It is simple to prove that IBC is the 2D extension of the Ohm's law and it satisfies uniqueness of the electromagnetic boundary value problem's solution [97]. Asymptotic behaviour of IBC and ABC for $\overline{\overline{\mathbf{Z}}}_{\mathrm{s}} = 0$ and $\overline{\overline{\mathbf{Y}}}_{\mathrm{s}} = 0$ yields PEC and PMC BCs, respectively. Generalized tensorial IBC and ABC and their higher order forms account for the non-local BC by field's spatial derivatives [97].

[3]Note that higher order multipoles cannot be considered as a superposition of monopoles, since different orders of the delta function are orthonormal.

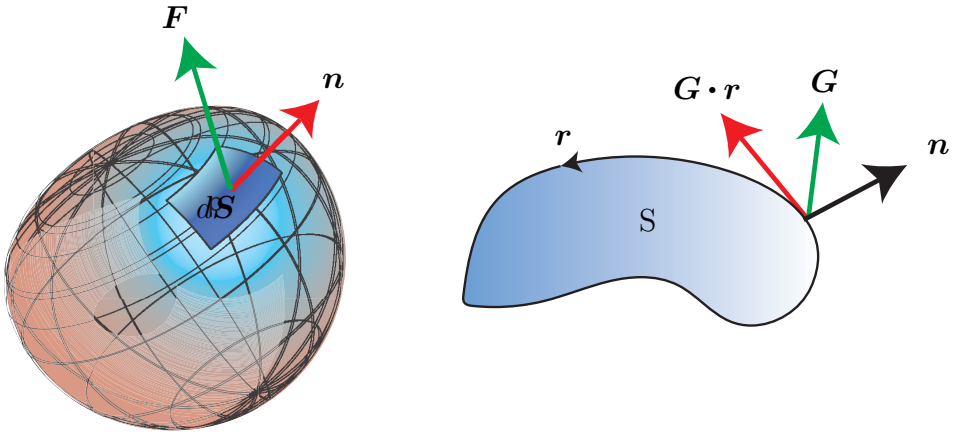

$$\oint_s \boldsymbol{F} \cdot \boldsymbol{n} dS = \int_V \nabla \cdot \boldsymbol{F} dv \qquad \oint_c \boldsymbol{G} \cdot d\boldsymbol{r} = \int \int_S (\nabla \times \boldsymbol{G}) \cdot \boldsymbol{n} dS$$

Figure 2.1 Representation of the Gauss (left) and Stockes (right) theorem, with $\boldsymbol{n}$ the normal vector, dS a surface element on the surface S covering the volume V, $\boldsymbol{r}$ is a closed path surrounding surface S and $\boldsymbol{G}$ and $\boldsymbol{F}$ are continuous functions.

Perfect electromagnetic conductor (PEMC) is the simplified version of these two boundary conditions [98], which reads

$$\hat{n} \times (\mathbf{H} + M\mathbf{E}) = 0, \quad \hat{n} \times (\mathbf{D} - M\mathbf{B}) = 0, \tag{2.3}$$

where M is the admittance of the PEMC BC. In this relation, $M = 0$ and $M \longrightarrow \infty$ corresponds to PMC and PEC BCs, respectively. Unlike the PEC and PMC BCs, PEMC represents non-reciprocity when M takes a finite value. Non-reciprocity of PEMC is demonstrated by investigating the polarization of the reflected wave. Depending on the value of the admittance parameter M, cross-polarized reflected field can be observed, which is a manifestation of non-reciprocity [99]. By simple mathematics, PEMC BC can be inferred from IBC, too.

Therefore, unlike classical BCs, TCs are fictitious models representing sheet discontinuity and they may seem capable of modeling metasurfaces. However, they can *only* take into account discontinuity in the electric field or magnetic field, i.e. simple discontinuity, while metasurfaces essentially represent a general discontinuity, simultaneous electric and magnetic fields discontinuity. Furthermore, they are bianisotropic in general, which is not compatible with the aforementioned mathematical models.

2.2 Generalized Sheet Transition Boundary Condition (GSTC)

Inapplicability of BCs and classical TCs inspired to develop an advanced form of TCs. This novel TC is known as the generalized sheet transition conditions (GSTCs) and were developed by Idemen [46]. Using distribution theory [100] a discontinuous function $f(x)$ can be expanded in terms of derivatives of the Dirac delta function [100]. Assuming a discontinuity at $x = 0$, such an expansion yields

$$f(x) = \{f(x)\} + \sum_{k=0}^{N} f_k \delta^{(k)}(x), \tag{2.4}$$

where $f(x)$ can be any field or current quantity in Maxwell equations, $\delta^{(k)}$ represents the k-th derivative of the Dirac delta function. In (2.4), $\{f(x)\}$ is the continuous part of the function $f(x)$, corresponding to $f(x)$ everywhere in space except at $x = 0$, and the sum term corresponds to the singular part of the function $f(x)$ and represents the value of $f(x)$ precisely at $x = 0$.

Expanding all the fields and sources in the form of (2.4) and their substitution in the Maxwell equations give two different sets of relations, namely, universal boundary conditions and compatibility relations, as detailed in [44, 46]. Equating different Delta function order (k) in the compatibility relation and its recursive solving gives the frequency domain GSTC as

$$\hat{\boldsymbol{n}} \times \Delta\tilde{\boldsymbol{H}}_{\text{act}} = \tilde{\boldsymbol{J}}_{\text{s}} + j\omega\tilde{\boldsymbol{P}}_{\parallel} - \hat{\boldsymbol{n}} \times \nabla_{\parallel}\tilde{M}_n, \tag{2.5a}$$

$$\Delta\tilde{\boldsymbol{E}}_{\text{act}} \times \hat{\boldsymbol{n}} = \tilde{\boldsymbol{K}}_{\text{s}} + j\omega\mu_0\tilde{\boldsymbol{M}}_{\parallel} - \nabla_{\parallel}\left(\frac{\tilde{P}_n}{\epsilon_0}\right) \times \hat{\boldsymbol{n}}, \tag{2.5b}$$

$$\hat{\boldsymbol{n}} \cdot \Delta\tilde{\boldsymbol{D}}_{\text{act}} = \tilde{\rho}_{\text{s}}^{\text{e}} - \nabla \cdot \tilde{\boldsymbol{P}}_{\parallel}, \tag{2.5c}$$

$$\hat{\boldsymbol{n}} \cdot \Delta\tilde{\boldsymbol{B}}_{\text{act}} = \tilde{\rho}_{\text{s}}^{\text{m}} - \mu_0\nabla \cdot \tilde{\boldsymbol{M}}_{\parallel}, \tag{2.5d}$$

where $\tilde{\boldsymbol{M}}$ and $\tilde{\boldsymbol{P}}$ are represented in the context of a sheet (not bulk) material, act is the acting field on the metasurface and the tilde symbol indicates frequency domain quantities. In this thesis, $\hat{\boldsymbol{n}} = \hat{\boldsymbol{x}}$ is the normal direction to the discontinuity. The corresponding time-domain GSTCs is obtained upon replacing $j\omega$ by $\frac{\partial}{\partial t}$. In (2.5), the electric and magnetic fields are rigorously the fields *acting* at $x = 0$, where the metasurface is located. Using $\overline{\overline{\chi}}_{\text{ee}}$, $\overline{\overline{\chi}}_{\text{mm}}$, $\overline{\overline{\chi}}_{\text{em}}$ and $\overline{\overline{\chi}}_{\text{me}}$ (e: electric and m: magnetic) susceptibility tensors, the surface electric and

magnetic polarization densities[4], $\tilde{\boldsymbol{P}}$ and $\tilde{\boldsymbol{M}}$, are related to the acting fields using

$$\tilde{\boldsymbol{P}} = \epsilon_0 \overline{\overline{\tilde{\chi}}}_{\mathrm{ee}} \cdot \tilde{\boldsymbol{E}}_{\mathrm{act}} + \frac{1}{c_0} \overline{\overline{\tilde{\chi}}}_{\mathrm{em}} \cdot \tilde{\boldsymbol{H}}_{\mathrm{act}}, \tag{2.6a}$$

$$\tilde{\boldsymbol{M}} = \overline{\overline{\tilde{\chi}}}_{\mathrm{mm}} \cdot \tilde{\boldsymbol{H}}_{\mathrm{act}} + \frac{1}{\eta_0} \overline{\overline{\tilde{\chi}}}_{\mathrm{me}} \cdot \tilde{\boldsymbol{E}}_{\mathrm{act}}, \tag{2.6b}$$

Next, we approximate the acting fields by the arithmetic average of the fields before ($x = 0^-$) and after ($x = 0^+$) the metasurface, i.e. $\tilde{\boldsymbol{\psi}}_{\mathrm{act}} \approx \tilde{\boldsymbol{\psi}}_{\mathrm{av}} = (\tilde{\boldsymbol{\psi}}_{\mathrm{inc}} + \tilde{\boldsymbol{\psi}}_{\mathrm{r}} + \tilde{\boldsymbol{\psi}}_{\mathrm{tr}})/2 = \tilde{\boldsymbol{\psi}}$ with inc, r and tr expressing incident, reflected and transmitted fields. Note that one may write the constitutive relation between the fields and the polarizations using polarizability tensors ($\overline{\overline{\tilde{\boldsymbol{\alpha}}}}_{\mathrm{ee}}$, $\overline{\overline{\tilde{\boldsymbol{\alpha}}}}_{\mathrm{em}}$, $\overline{\overline{\tilde{\boldsymbol{\alpha}}}}_{\mathrm{mm}}$ and $\overline{\overline{\tilde{\boldsymbol{\alpha}}}}_{\mathrm{me}}$) approach

$$\tilde{\boldsymbol{P}} = \overline{\overline{\tilde{\boldsymbol{\alpha}}}}_{\mathrm{ee}} . \boldsymbol{E}^{\mathrm{inc}} + \overline{\overline{\tilde{\boldsymbol{\alpha}}}}_{\mathrm{em}} . \boldsymbol{H}^{\mathrm{inc}}, \tag{2.7}$$

$$\tilde{\boldsymbol{M}} = \overline{\overline{\tilde{\boldsymbol{\alpha}}}}_{\mathrm{mm}} . \boldsymbol{H}_{\mathrm{inc}} + \overline{\overline{\tilde{\boldsymbol{\alpha}}}}_{\mathrm{me}} . \boldsymbol{E}^{\mathrm{inc}}. \tag{2.8}$$

We use the susceptibility description due to its generality and more physical insight that will be discussed later.

Since equation (2.4) contains infinite derivatives of the Dirac delta function, consequently, the field quantities in (2.5) involves infinite order of discontinuity. However, for most metasurface it is sufficient to reduce the sum in (2.4) and use the first term corresponding to $k = 0$. As a result of this approximation, the TC will only take into account the discontinuity of the fields but not the discontinuities in their derivatives. Throughout this thesis we will use the first order GSTCs. Assuming $\tilde{\boldsymbol{J}}_{\mathrm{s}} = \tilde{\boldsymbol{K}}_{\mathrm{s}} = 0$, Equ. (2.5a) and (2.5b) reduces to

$$\hat{\boldsymbol{x}} \times \Delta\tilde{\boldsymbol{H}} = j\omega\varepsilon_0 \overline{\overline{\tilde{\chi}}}_{\mathrm{ee}} \cdot \tilde{\boldsymbol{E}}_{\mathrm{av},\parallel} + jk_0 \overline{\overline{\tilde{\chi}}}_{\mathrm{em}} \cdot \tilde{\boldsymbol{H}}_{\mathrm{av},\parallel} - \hat{\boldsymbol{x}} \times \nabla_{\parallel} \tilde{M}_x, \tag{2.9a}$$

$$\Delta\tilde{\boldsymbol{E}} \times \hat{\boldsymbol{x}} = j\omega\mu_0 \overline{\overline{\tilde{\chi}}}_{\mathrm{mm}} \cdot \tilde{\boldsymbol{H}}_{\mathrm{av},\parallel} + jk_0 \overline{\overline{\tilde{\chi}}}_{\mathrm{me}} \cdot \tilde{\boldsymbol{E}}_{\mathrm{av},\parallel} - \nabla_{\parallel} \left(\frac{\tilde{P}_x}{\epsilon_0} \right) \times \hat{\boldsymbol{x}}, \tag{2.9b}$$

where $\parallel$ is the tangential component of the vector.

As we mentioned earlier, GSTCs are the extended version of classical BCs. Therefore, all other BCs and TCs should be expressible using the GSTCs. For example, assume isotropic χ_{ee} and $\Im(\chi_{\mathrm{ee}}) \to -\infty$, where the sign $\Im(\chi_{\mathrm{ee}})$ shows the imaginary part of the quantity χ_{ee}. Since the fields cannot be infinite, thus, in (2.9a) $\overline{\overline{\tilde{\chi}}}_{\mathrm{ee}} \cdot \tilde{\boldsymbol{E}}_{\mathrm{av},\parallel}$ should be finite. This is established only if $\tilde{\boldsymbol{E}}_{\mathrm{av},\parallel} \to 0$, which is the PEC BC. Similar argument for χ_{mm} gives PMC

[4]Unlike to the unit-less volume susceptibilities, the *surface* susceptibilities are measured in meters, which can be understood by comparing (2.5) and (2.6).

BC. The general comparison can be made clear by comparing (2.5) or (2.9) and (2.1). Finally, in (2.9), when the discontinuity is removed ($\overline{\overline{\tilde{\chi}}} = P_x = M_x = 0$), $\Delta \boldsymbol{E} = \Delta \boldsymbol{H} = 0$, stating continuity of the fields at the interface as expected. Comparison of the GSTCs [Eqs. (2.5)] and IBCs [Eqs. (2.2)] reveals that GSTCs are more complete and rigorous than IBCs as they include normal susceptibility components, through P_x and M_x, while IBCs ignore this and consider only tangential component of the impedance or admittance. Furthermore, GSTCs take into account the nonlinear and higher order discontinuity [101], while IBCs cannot.

From the surface equivalent theorem [102], normal component of any wave ($\psi_\perp = \psi_\mathrm{n}$) can be expressed in terms of its tangential components ($\boldsymbol{\psi}_\parallel = \boldsymbol{\psi}_\mathrm{t}$), leading to the expansion of the normal polarization densities in terms of its tangential components. The relation between the normal and transverse components of the fields are [78]

$$\tilde{E}_\mathrm{n} = \pm \frac{1}{\omega \varepsilon_\pm} \overline{\overline{\tilde{k}}}_\mathrm{t} . \left(\tilde{\boldsymbol{Z}}_\pm^{-1} . \overline{\overline{\tilde{E}}}_\mathrm{t} \right), \tag{2.10}$$

$$\tilde{H}_\mathrm{n} = -\frac{1}{\tilde{k}_{n,\pm}} \overline{\overline{\tilde{k}}}_\mathrm{t} . \left(\overline{\overline{n}} \times \tilde{\tilde{\boldsymbol{Z}}}_\pm^{-1} . \overline{\overline{\tilde{E}}}_\mathrm{t} \right), \tag{2.11}$$

and

$$\overline{\overline{\tilde{Z}}}_l = \eta_l \sqrt{1 - \frac{\tilde{k}_\mathrm{t}}{\tilde{k}_l}} \frac{\tilde{\boldsymbol{k}}_\mathrm{t} \tilde{\boldsymbol{k}}_\mathrm{t}}{\tilde{k}_\mathrm{t}^2} + \frac{\eta_l}{\sqrt{1 - \frac{\tilde{k}_\mathrm{t}}{\tilde{k}_l}}} \frac{(\boldsymbol{n} \times \tilde{\boldsymbol{k}}_\mathrm{t})(\boldsymbol{n} \times \tilde{\boldsymbol{k}}_\mathrm{t})}{\tilde{k}_\mathrm{t}^2}, \tag{2.12}$$

where $\tilde{k}_{n,\mathrm{l}} = \sqrt{\omega^2 \mu_l \varepsilon_l - \tilde{k}_\mathrm{t}^2}$ and $l = +, -$. Thus, in (2.9), the normal polarization densities will lead to redundant solutions, unless one wishes to design a metasurface with different specified fields to different excitations. The case $\tilde{M}_x, \tilde{P}_x \neq 0$ leads to differential equations and is therefore more problematic [44].

Under $\tilde{M}_x = \tilde{P}_x = 0$ assumption, the surface susceptibility tensors become 2×2 transverse tensors. Its substitution in (2.5) and performing the matrix products gives

$$\begin{pmatrix} -\Delta \tilde{H}_z \\ \Delta \tilde{H}_y \end{pmatrix} = j\omega\varepsilon_0 \begin{pmatrix} \tilde{\chi}_\mathrm{ee}^{yy} & \tilde{\chi}_\mathrm{ee}^{yz} \\ \tilde{\chi}_\mathrm{ee}^{zy} & \tilde{\chi}_\mathrm{ee}^{zz} \end{pmatrix} \begin{pmatrix} \tilde{E}_{y,\mathrm{av}} \\ \tilde{E}_{z,\mathrm{av}} \end{pmatrix} + jk_0 \begin{pmatrix} \tilde{\chi}_\mathrm{em}^{yy} & \tilde{\chi}_\mathrm{em}^{yz} \\ \tilde{\chi}_\mathrm{em}^{zy} & \tilde{\chi}_\mathrm{em}^{zz} \end{pmatrix} \begin{pmatrix} \tilde{H}_{y,\mathrm{av}} \\ \tilde{H}_{z,\mathrm{av}} \end{pmatrix}, \tag{2.13a}$$

$$\begin{pmatrix} -\Delta \tilde{E}_y \\ \Delta \tilde{E}_z \end{pmatrix} = j\omega\mu_0 \begin{pmatrix} \tilde{\chi}_\mathrm{mm}^{zz} & \tilde{\chi}_\mathrm{mm}^{zy} \\ \tilde{\chi}_\mathrm{mm}^{yz} & \tilde{\chi}_\mathrm{mm}^{yy} \end{pmatrix} \begin{pmatrix} \tilde{H}_{z,\mathrm{av}} \\ \tilde{H}_{y,\mathrm{av}} \end{pmatrix} + jk_0 \begin{pmatrix} \tilde{\chi}_\mathrm{me}^{zz} & \tilde{\chi}_\mathrm{me}^{zy} \\ \tilde{\chi}_\mathrm{me}^{yz} & \tilde{\chi}_\mathrm{me}^{yy} \end{pmatrix} \begin{pmatrix} \tilde{E}_{z,\mathrm{av}} \\ \tilde{E}_{y,\mathrm{av}} \end{pmatrix}. \tag{2.13b}$$

Equation (2.13) provides the susceptibilities required for a transformation in terms of the specified incident, reflected and transmitted fields. For a single, double or triple transformation multiple solutions are possible, as discussed in [44]. This relation can be calculated

in a very concise manner without using distribution theory. We can simply separate the transverse and normal components of the fields and polarizations in Maxwell equation and obtain

$$\nabla_{\mathrm{t}} \times \boldsymbol{x}\tilde{E}_n + \frac{\partial}{\partial x}(\boldsymbol{x} \times \tilde{\boldsymbol{E}}_{\mathrm{t}}) = -j\omega\mu\tilde{\boldsymbol{H}}_{\mathrm{t}} - j\omega\tilde{\boldsymbol{M}}_{\mathrm{t}}\delta(x), \tag{2.14}$$

$$\nabla_{\mathrm{t}} \times \boldsymbol{x}\tilde{H}_n + \frac{\partial}{\partial x}(\boldsymbol{x} \times \tilde{\boldsymbol{H}}_{\mathrm{t}}) = -j\omega\mu\tilde{\boldsymbol{H}}_{\mathrm{t}} - j\omega\tilde{\boldsymbol{P}}_{\mathrm{t}}\delta(x), \tag{2.15}$$

At this steps, without having any prior knowledge of (2.9), we can argue that normal polarization creation requires bulk material and also substitution of (2.6) into (2.14) and (2.15) will require their space derivatives, thus, we set them zero. This will result in their simplification. Next, using the definition of space derivative [5], we will have

$$\boldsymbol{x} \times \Big[\tilde{\boldsymbol{E}}_{\mathrm{t}}(\Delta x/2) - \tilde{\boldsymbol{E}}_{\mathrm{t}}(-\Delta x/2)\Big] = -j\Delta x\omega\mu\tilde{\boldsymbol{H}}_{\mathrm{t}} - j\omega\tilde{\boldsymbol{M}}_{\mathrm{t}}\Delta x\delta(x), \tag{2.16}$$

$$\boldsymbol{x} \times \Big[\tilde{\boldsymbol{H}}_{\mathrm{t}}(\Delta x/2) - \tilde{\boldsymbol{H}}_{\mathrm{t}}(-\Delta x/2)\Big] = -j\Delta x\omega\mu\tilde{\boldsymbol{H}}_{\mathrm{t}} - j\omega\tilde{\boldsymbol{P}}_{\mathrm{t}}\Delta x\delta(x), \tag{2.17}$$

Since the fields cannot be infinite and $\Delta x \to 0$, $\Delta x\tilde{\boldsymbol{H}}_{\mathrm{t}} = \Delta x\tilde{\boldsymbol{E}}_{\mathrm{t}} = 0$. On the other hand, from the delta function definition, $\Delta x\delta(x) = 1$. Finally, replacing $\psi(\pm\Delta x/2)$ by $\psi(0^{\pm})$ and representing their subtraction by Δ, yields

$$\boldsymbol{x} \times \Delta\tilde{\boldsymbol{E}}_{\mathrm{t}} = -j\omega\mu_0\tilde{\boldsymbol{M}}_{\mathrm{t}}, \tag{2.18}$$

$$\boldsymbol{x} \times \Delta\tilde{\boldsymbol{H}}_{\mathrm{t}} = -j\omega\tilde{\boldsymbol{P}}_{\mathrm{t}}. \tag{2.19}$$

Substitution of constitutive relation from (2.6) and its simplification results (2.13). A similar method to achieve this is presented in the appendix of [78] where they are using more sophisticated steps than what we presented here.

2.3 Description of the Susceptibility Solutions of the GSTCs

Equation (2.13) does not provide any warranty on the physicality and realizability of the resulted susceptibilities. However, it provides information on the characteristics of the required metasurface such as loss, gain, reciprocity and etc. The Lorentz reciprocity for a

[5] $$\frac{\partial f}{\partial x} = \lim_{\Delta x \to 0} \frac{f(\Delta x/2) - f(-\Delta x/2)}{\Delta x}$$

bianisotropic medium is [103]

$$\overline{\overline{\tilde{\chi}}}_{\mathrm{ee}}^{\mathrm{T}} = \overline{\overline{\tilde{\chi}}}_{\mathrm{ee}}, \quad \overline{\overline{\tilde{\chi}}}_{\mathrm{mm}}^{\mathrm{T}} = \overline{\overline{\tilde{\chi}}}_{\mathrm{mm}}, \quad \overline{\overline{\tilde{\chi}}}_{\mathrm{me}}^{\mathrm{T}} = -\overline{\overline{\tilde{\chi}}}_{\mathrm{em}} \tag{2.20}$$

with T denoting the transpose operation. Following the calculations of [104], the susceptibility condition for a simultaneously passive, lossless and reciprocal metasurface reads as

$$\overline{\overline{\tilde{\chi}}}_{\mathrm{ee}}^{\mathrm{T}} = \overline{\overline{\tilde{\chi}}}_{\mathrm{ee}}^{*}, \quad \overline{\overline{\tilde{\chi}}}_{\mathrm{mm}}^{\mathrm{T}} = \overline{\overline{\tilde{\chi}}}_{\mathrm{mm}}^{*}, \quad \overline{\overline{\tilde{\chi}}}_{\mathrm{me}}^{\mathrm{T}} = \overline{\overline{\tilde{\chi}}}_{\mathrm{em}}^{*} \tag{2.21}$$

with $*$ the complex conjugate value. Equations (2.20) and (2.21) shows that a simultaneously passive, lossless and reciprocal metasurface have real $\overline{\overline{\tilde{\chi}}}_{\mathrm{ee}}$ and $\overline{\overline{\tilde{\chi}}}_{\mathrm{mm}}$ and pure imaginary $\overline{\overline{\tilde{\chi}}}_{\mathrm{me}}$ and $\overline{\overline{\tilde{\chi}}}_{\mathrm{em}}$. Equation (2.13) permits maximum of 8 transformations. With the above-mentioned conditions on the reciprocity, lossless and passive metasurface, the maximum available transformations will be limited.

Equation (2.13) also provides information on the type of the required metasurface unit-cell shape. For the design of a reflective metasurface ($T = 0$), one may use a PEC-backed unit-cells, an example of which is shown Fig. 2.2a [105]. While an anisotropic metasurface requires symmetric unit-cell, a bianisotropic should be designed using asymmetric unit-cells. If bianisotropic susceptibility terms are involved in an application, then, the selected unit-cell must generate a magnetic response to electric field stimulation and vice versa. Unit-cell of Fig. 2.2a is unable to create such response, and the type of the unit-cell should be selected depending on the magnetoelectric coupling term and reciprocity of the transformation [57, 106]. For example, for omega bianisotropy, a loop-shaped inclusion such as the one shown in Fig. 2.2b is useful [78]. This unit-cell, when normally excited by a parallel-polarized (p-polarized) plane-wave, creates a net magnetic field through the induced circulating current on the ring. A transformation requiring 360° of phase variation involves a minimum of three metallic layers (two substrate layers), and one may reduce the number of layers depending on the required phase range [107]. Dog-bone unit-cell shown in Fig. 2.2c is a possible choice for achieving 360° phase variation.

The reflection and transmission from an anisotropic metasurface is [44]

$$\tilde{T}_z = \frac{4 + \tilde{\chi}_{\mathrm{ee}}^{zz}\tilde{\chi}_{\mathrm{mm}}^{yy}k_0^2}{\left(2 + jk_0\tilde{\chi}_{\mathrm{ee}}^{zz}\right)\left(2 + jk_0\tilde{\chi}_{\mathrm{mm}}^{yy}\right)}, \tag{2.22}$$

$$\tilde{R}_z = \frac{2jk_0\left(\tilde{\chi}_{\mathrm{mm}}^{yy} - \tilde{\chi}_{\mathrm{ee}}^{zz}\right)}{\left(2 + jk_0\tilde{\chi}_{\mathrm{ee}}^{zz}\right)\left(2 + jk_0\tilde{\chi}_{\mathrm{mm}}^{yy}\right)}, \tag{2.23}$$

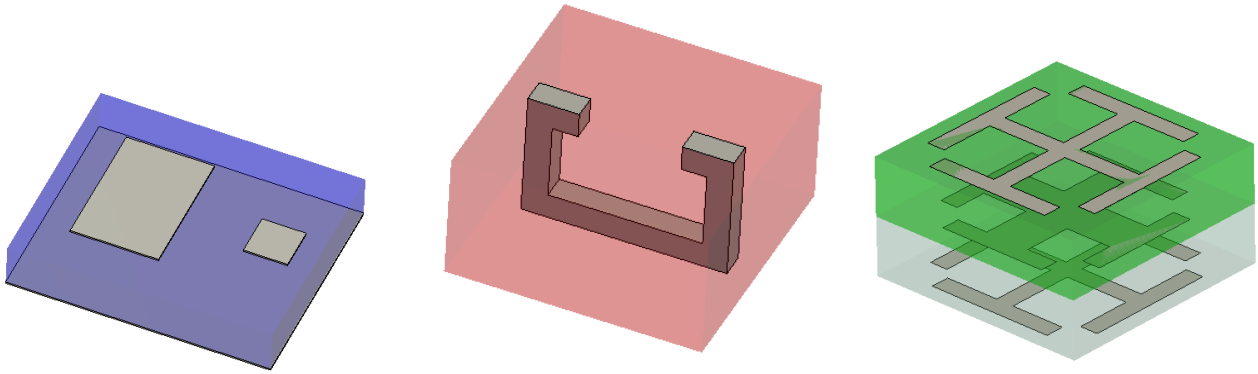

(a) (b) (c)

Figure 2.2 Metasurface unit-cells corresponding to different susceptibility specifications. All of these unit-cells are illuminated from the top. (a) PEC backed unit-cell. (b) Split-ring resonator for omega bianisotropic metasurface when illuminated by a p-polarized plane wave. (c) Three layer Jerusalem cross unit-cell giving 360° phase variation.

for a normally-polarized ($x-$polarized) wave and

$$\tilde{T}_y = \frac{4 + \tilde{\chi}_{\mathrm{ee}}^{yy}\tilde{\chi}_{\mathrm{mm}}^{zz}k_0^2}{\left(2 + jk_0\tilde{\chi}_{\mathrm{ee}}^{yy}\right)\left(2 + jk_0\tilde{\chi}_{\mathrm{mm}}^{zz}\right)}, \tag{2.24}$$

$$\tilde{R}_y = \frac{2jk_0\left(\tilde{\chi}_{\mathrm{mm}}^{zz} - \tilde{\chi}_{\mathrm{ee}}^{yy}\right)}{\left(2 + jk_0\tilde{\chi}_{\mathrm{ee}}^{yy}\right)\left(2 + jk_0\tilde{\chi}_{\mathrm{mm}}^{zz}\right)}, \tag{2.25}$$

for a parallel-polarized ($y-$polarized) wave. These relations express that for a non-reflective metasurface $\tilde{\chi}_{\mathrm{mm}}^{yy} = \tilde{\chi}_{\mathrm{ee}}^{zz}$ and $\tilde{\chi}_{\mathrm{mm}}^{zz} = \tilde{\chi}_{\mathrm{ee}}^{yy}$.

Therefore, the susceptibility synthesis method provides more physical insight to the problem than other techniques such as, impedance and polarizablility. In this thesis, we will use susceptibility technique and through mathematical manipulations, one can obtain the relation between these techniques as detailed in [78, 104].

2.4 GSTC Relation with Tensor Boundary Condition (TBC)

It is very important to note that GSTC boundary condition is different from the tensor boundary condition (TBC) [108]. To facilitate TBC comparison with GSTCs, TBC is simplified as [109]

$$\begin{pmatrix} \Delta\tilde{H}_y \\ -\Delta\tilde{H}_z \end{pmatrix} = -\frac{jk_0}{\eta_0}\upsilon_1 \begin{pmatrix} 1 & 0 \\ 0 & 1 \end{pmatrix} \begin{pmatrix} \tilde{E}_{z,\mathrm{av}} \\ \tilde{E}_{y,\mathrm{av}} \end{pmatrix} - jk_0\upsilon_2 \begin{pmatrix} 0 & -1 \\ 1 & 0 \end{pmatrix} \begin{pmatrix} \tilde{H}_{z,\mathrm{av}} \\ \tilde{H}_{y,\mathrm{av}} \end{pmatrix}, \tag{2.26a}$$

$$\begin{pmatrix} \Delta\tilde{E}_y \\ -\Delta\tilde{E}_z \end{pmatrix} = jk_0\eta_0 \begin{pmatrix} \frac{-1}{\eta_0} & 0 \\ 0 & \frac{-1}{\eta_0} \end{pmatrix} \begin{pmatrix} \tilde{H}_{z,\mathrm{av}} \\ \tilde{H}_{y,\mathrm{av}} \end{pmatrix} + jk_0\upsilon_2 \begin{pmatrix} 0 & -1 \\ 1 & 0 \end{pmatrix} \begin{pmatrix} \tilde{E}_{z,\mathrm{av}} \\ \tilde{E}_{y,\mathrm{av}} \end{pmatrix}, \tag{2.26b}$$

where $\upsilon_1 = j\frac{2\eta_0 R_\mathrm{m}}{k_0 D}, \upsilon_2 = j\frac{2R_\mathrm{c}}{k_0 D}, D = R_\mathrm{e}R_\mathrm{m} - R_\mathrm{c}^2$ and $R_\mathrm{e}, R_\mathrm{m}$ and R_c are scalar resistivity, scalar conductivity and cross-coupling terms, respectively, defined in [108]. This shows that TBC sheets are restricted form of GSTCs, for example, they are reciprocal and nongyrotropic sheets. Consequently, they have limited application compared to the metasurfaces. However, similar to the metasurfaces, they introduce discontinuity on both electric and magnetic fields.

2.5 Metasurface Synthesis

In general, a metasurface synthesis can be accomplished in three different ways depending on the region that the fields are specified. These methods are elaborated upon below.

2.5.1 Direct Susceptibility Method

In the most simple case where the fields are defined right after ($x = 0^+$) and before ($x = 0^-$) the metasurface, the susceptibilities can be directly calculated through (2.13). In this method, depending on the number of transformations and specifications, one may set to zero some of the susceptibilities in (2.13). For example, a single transformation can be obtained using an anisotropic metasurface as

$$\tilde{\chi}_\mathrm{ee}^{zz} = \frac{1}{j\omega\varepsilon_0}\frac{\Delta\tilde{H}_y}{\tilde{E}_{z,\mathrm{av}}}, \tag{2.27}$$

$$\tilde{\chi}_\mathrm{ee}^{yy} = \frac{1}{j\omega\varepsilon_0}\frac{-\Delta\tilde{H}_z}{\tilde{E}_{y,\mathrm{av}}}, \tag{2.28}$$

$$\tilde{\chi}_\mathrm{mm}^{zz} = \frac{1}{j\omega\mu_0}\frac{-\Delta\tilde{E}_y}{\tilde{H}_{z,\mathrm{av}}}, \tag{2.29}$$

$$\tilde{\chi}_\mathrm{mm}^{yy} = \frac{1}{j\omega\mu_0}\frac{-\Delta\tilde{E}_z}{\tilde{H}_{y,\mathrm{av}}}. \tag{2.30}$$

$$\tag{2.31}$$

However, one may use bianisotropic metasurface while a single transformation is specified. For example, an application may demand a diffraction-less refractive passive metasurface, which cannot be obtained using anisotropic metasurface. In this case, bianisotropic terms may be involved [80]. We will see its details in the following example.

For a better illustration of this synthesis technique, we show the case of a beam-splitting

metasurface at $f = 10.2$ GHz. Beam-splitter is a crucial component in quantum computers [110] and most interferometers [111]. It splits an incoming plane-wave $(\boldsymbol{E_1}, \boldsymbol{H_1})$ at θ^{inc} angle into two beams at $\theta^{\text{tr,a}}$ and $\theta^{\text{tr,b}}$ directions, as shown in Fig. 2.3a.

We choose a parallel polarized incident field where E_x, E_y and H_z are the nonzero field components, and $\theta^{\text{inc}} = -45°, \theta^{\text{tr,a}} = 45°$ and $\theta^{\text{tr,b}} = -60°$, measured clock-wise from the x-axis. For the specified field components, equation (2.13) reduces to

$$-\Delta\tilde{H}_z = j\omega\varepsilon_0\tilde{\chi}_{\text{ee}}^{yy}\tilde{E}_{y,\text{av}} + jk_0\tilde{\chi}_{\text{em}}^{yz}\tilde{H}_{z,\text{av}}, \tag{2.32a}$$

$$-\Delta\tilde{E}_y = j\omega\mu_0\tilde{\chi}_{\text{mm}}^{zz}\tilde{H}_{z,\text{av}} + jk_0\tilde{\chi}_{\text{me}}^{zy}\tilde{E}_{y,\text{av}}, \tag{2.32b}$$

The first synthesis steps is the calculation of $\tilde{\chi}$s in (2.32), which corresponds to the ① in Fig. 1.4. We divide the incident power equally between the two transmitted beams. To avoid undesired diffraction orders coming from the loss-gain combination of the anisotropic metasurface design, we synthesize a bianisotropic, reciprocal and passive metasurface. Due to the bianisotropy, as seen from (2.32), there are four unknowns and two equations. Thus, it is under-determined and a second transformation is essential for the synthesis. Following the synthesis technique of [80], we choose the second transformation as the reciprocal of the first transformation as depicted in Fig. 2.3b. For the reciprocal transformation, the fields $\boldsymbol{E}_2$ and $\boldsymbol{H}_2$ will be the time reversal of the fields $\boldsymbol{E}_1$ and $\boldsymbol{H}_1$, respectively, which are obtained via replacing j with $-j$ for the plane-wave. Therefore, the metasurface susceptibilities are found to be

$$\begin{bmatrix} \Delta\tilde{H}_{z1} & \Delta\tilde{H}_{z2} \\ \Delta\tilde{E}_{y1} & \Delta\tilde{E}_{y2} \end{bmatrix} = \begin{bmatrix} -j\omega\varepsilon_0\tilde{\chi}_{\text{ee}}^{yy} & -jk_0\tilde{\chi}_{\text{em}}^{yz} \\ -j\omega\varepsilon_0\tilde{\chi}_{\text{me}}^{zy} & -j\omega\mu_0\tilde{\chi}_{\text{mm}}^{zz} \end{bmatrix} \begin{bmatrix} \tilde{E}_{y1,\text{av}} & \tilde{E}_{y2,\text{av}} \\ \tilde{H}_{z1,\text{av}} & \tilde{H}_{z2,\text{av}} \end{bmatrix}. \tag{2.33}$$

Upon substituting the fields in (2.33), the susceptibilities are calculated and plotted in Fig. 2.4. As we mentioned in Sec. 2.3, the lossless condition have imposed $\Im(\tilde{\chi}_{\text{ee}}^{yy}) = \Im(\tilde{\chi}_{\text{mm}}^{zz}) = \Re(\tilde{\chi}_{\text{em}}^{yz}) = \Re(\tilde{\chi}_{\text{me}}^{zy}) = 0$ and the reciprocity resulted in $\Re(\tilde{\chi}_{\text{ee}}^{yy}) = \Re(\tilde{\chi}_{\text{mm}}^{zz})$ and $\Im(\tilde{\chi}_{\text{em}}^{yz}) = -\Im(\tilde{\chi}_{\text{me}}^{zy})$.

Next, we should find unit-cells that correspond to the calculated susceptibilities, which is ②

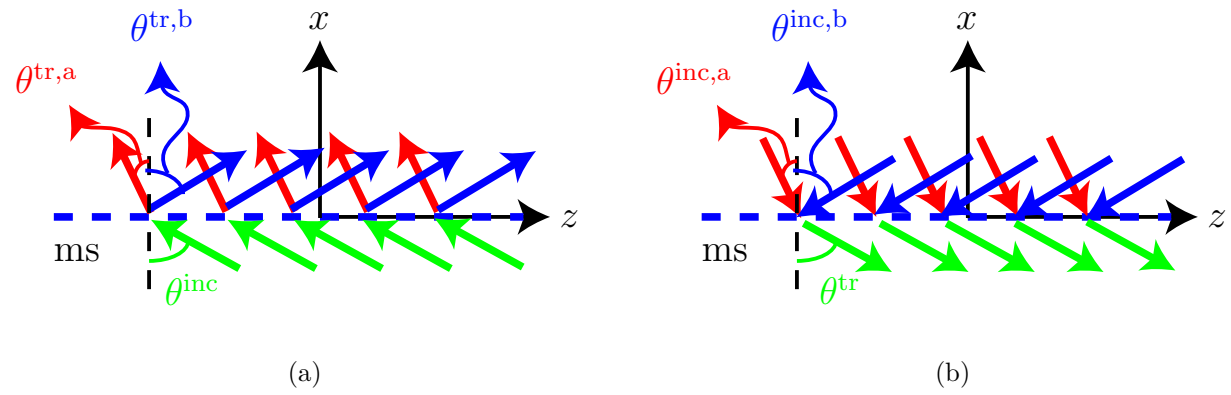

(a) (b)

Figure 2.3 Beam-splitting metasurface, dashed blue line, synthesis. (a) Direct problem with excitation from the bottom. (b) The reciprocal problem, where two plane-waves illuminate the metasurface from the top.

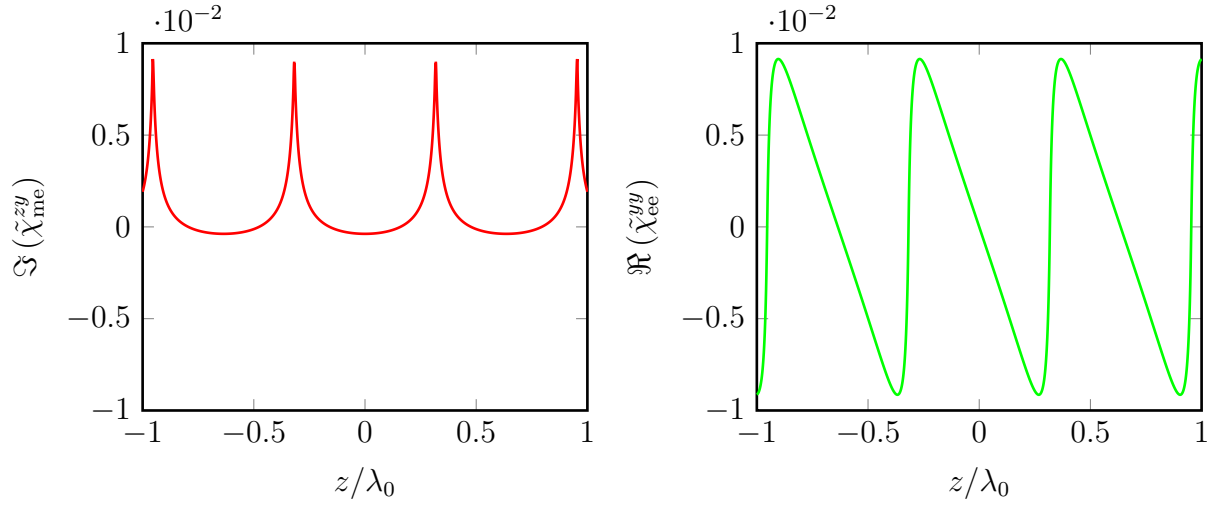

(a) (b)

Figure 2.4 Susceptibilities of the beam-splitting metasurface.

in Fig. 1.4. To this aim, we calculate the S-parameters through [44]

$$S^{yy}_{11} = -2j\frac{2k_0\eta_0\tilde{\chi}^{zy}_{\mathrm{me}} + \mu_0\omega\tilde{\chi}^{zz}_{\mathrm{mm}} - \eta_0^2\varepsilon_0\omega\tilde{\chi}^{yy}_{\mathrm{ee}}}{D^{yy}}, \tag{2.34}$$

$$S^{yy}_{22} = 2j\frac{2k_0\eta_0\tilde{\chi}^{zy}_{\mathrm{me}} - \mu_0\omega\tilde{\chi}^{zz}_{\mathrm{mm}} + \eta_0^2\varepsilon_0\omega\tilde{\chi}^{yy}_{\mathrm{ee}}}{D^{yy}}, \tag{2.35}$$

$$S^{yy}_{21} = S^{yy}_{12} = -j\eta_0\frac{4 + k_0^2\left(\tilde{\chi}^{zy}_{\mathrm{me}}\right)^2 + \mu_0\varepsilon_0\omega^2\tilde{\chi}^{yy}_{\mathrm{ee}}\chi^{zz}_{\mathrm{mm}}}{D^{yy}}, \tag{2.36}$$

where $D^{yy} = -2j\mu_0\omega\tilde{\chi}^{zz}_{\rm mm} + \eta_0\left[-4 + k_0^2\left(\tilde{\chi}^{zy}_{\rm me}\right)^2 + \varepsilon\omega\tilde{\chi}^{yy}_{\rm ee}\left(-2j\eta_0 + \mu_0\omega\tilde{\chi}^{zz}_{\rm mm}\right)\right]$. They have been plotted in Fig. 2.5. We assume $0.16\lambda_0$ unit-cell size and use the dog-bone unit-cell of Fig. 2.2c. Since periodicity of the S-parameters is $0.64\lambda_0$, thus, four unit-cells can fit at each period. Note that small unit-cell size will deteriorate the result as this makes difficult to gain large phase variation. We use the CST optimization and iterative simulation to find the dimension of each dog-bone cells such that the S-parameters of Fig. 2.5, sampled at $0.16\lambda_0$ distance points, are obtained. These dimensions are listed in Tab. 2.1.

Table 2.1 Unit-cells dimension (in mm) for the beam-splitting metasurface.

		w	l	g	s
Cell 1	Layer 1	3.034	0.419	3.55	0.552
	Layer 2	3.203	0.236	4.223	0.797
	Layer 3	3.2	0.626	4.1036	0.313
Cell 2	Layer 1	3.033	0.544	4.67	0.435
	Layer 2	2.88	0.665	3.906	0.647
	Layer 3	3.695	0.32	4.681	0.675
Cell 3	Layer 1	2.356	0.422	4.466	0.816
	Layer 2	3.123	0.48	4.304	0.558
	Layer 3	3.81	0.6	4.59	0.6
Cell 4	Layer 1	2.84	0.78	4.376	0.55
	Layer 2	3.84	0.172	4.334	0.234
	Layer 3	3.84	0.146	4.37	0.77

Finally, we juxtapose the unit-cells as shown in Fig. 2.6, and simulate the resulted super-cell with periodic BC. During the last step, another optimization may be required to obtain an efficient result.

The optimized simulation results are shown in Fig. 2.7. With $|S_{22}| > 0.63$ and $|S_{62}| > 0.63$ criteria [6], the frequency bandwidth is 630 MHz, measured by Fig. 2.7a and location of the ports are shown in Fig. 2.7c. By increasing the operation frequency, the power in $\theta^{\rm tr,b}$ direction or S_{62} remains constant, while, in $\theta^{\rm tr,a}$ direction decreases and the power is reflected almost equally in $S^{\rm r}_{22} = \theta^{\rm tr,a} + 180^\circ$ and $S^{\rm r}_{62} = \theta^{\rm tr,b} + 180^\circ$ directions. The fields in Fig. 2.7c are plotted at $f = 10.2$ GHz. The incident field comes from the left in $-x$ direction, and at the right of the metasurface, we see the transmitted fields. Fourier transform of transmitted field in Fig. 2.7b shows propagation at $\theta^{\rm tr,a} = 45^\circ$ and $\theta^{\rm tr,b} = 60^\circ$ directions, as expected.

[6] This criteria means at each of $\theta^{\rm tr,a}$ and $\theta^{\rm tr,b}$ directions, there is at least 43% of the total incident power and less than 5% of the total incident power lies in all other undesired directions.

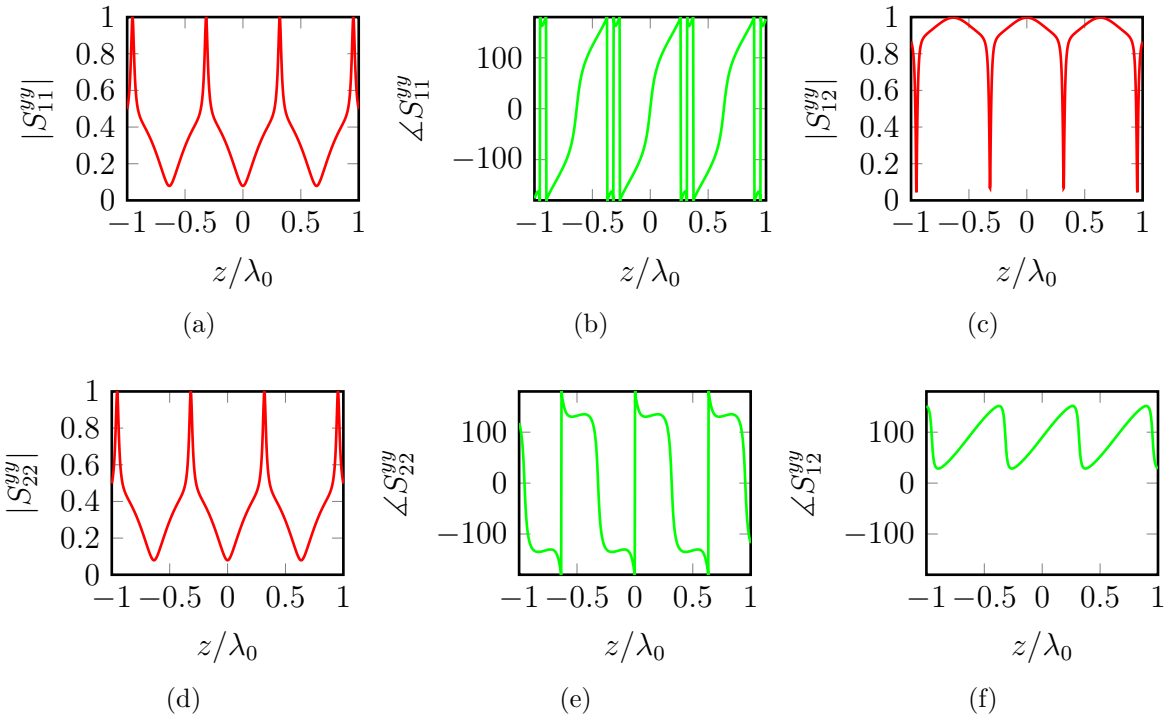

Figure 2.5 Beam-splitting metasurface S-parameters. (a) $|S_{11}^{yy}|$, (b) $\angle S_{11}^{yy}$, (c) $|S_{12}^{yy}|$, (d) $|S_{22}^{yy}|$, (e) $\angle S_{12}^{yy}$, (f) $\angle S_{12}^{yy}$.

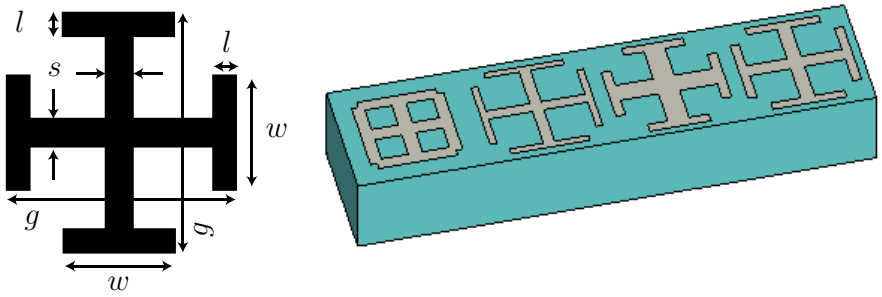

Figure 2.6 Super-cell and the related unit-cell of the beam-splitter metaurface simulated in CST with periodic boundary conditions.

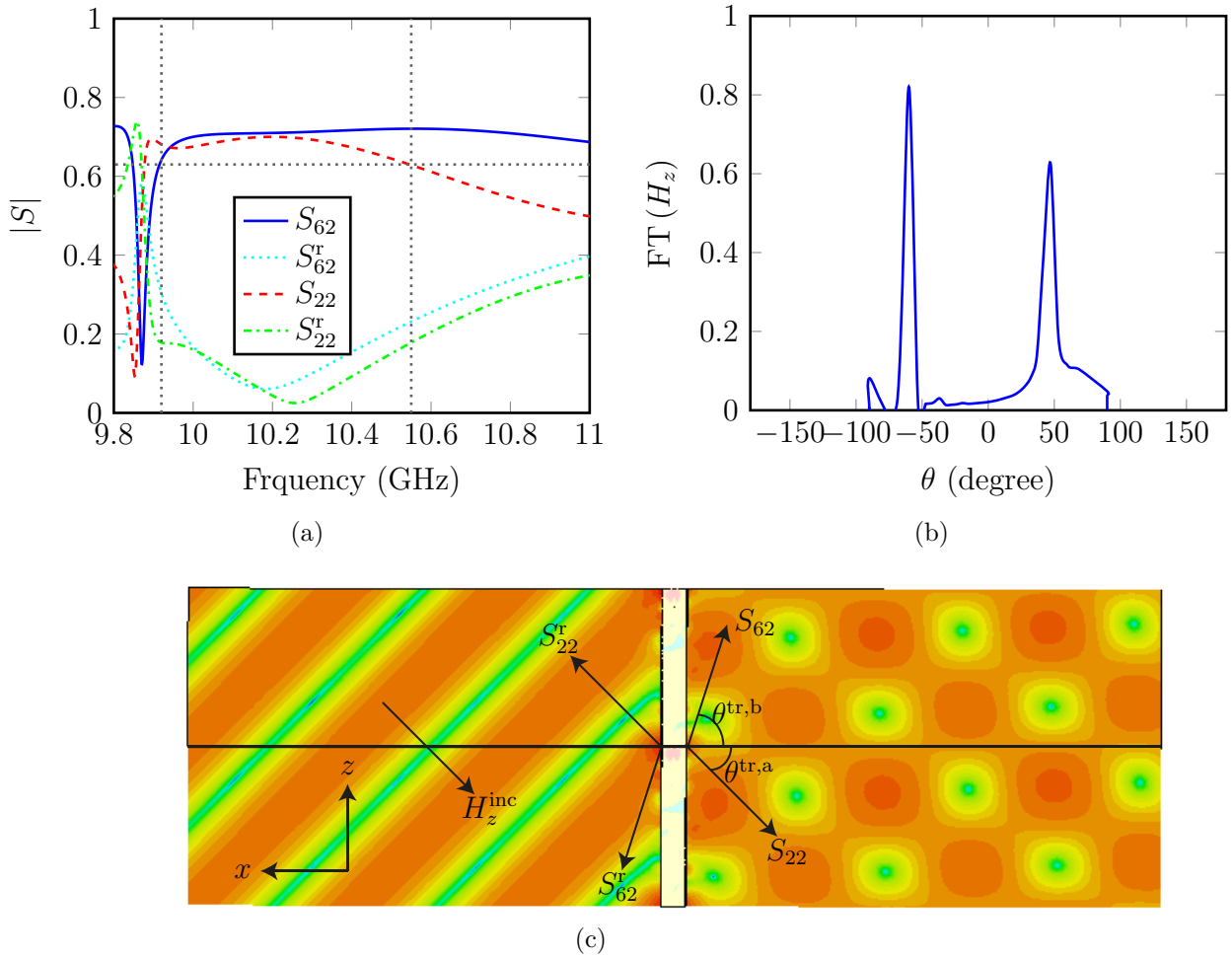

Figure 2.7 Beam-splitting metasurface CST simulation result. (a) S-parameters result, (b) Fourier transform of the transmitted field, and (c) transmitted and incident fields visualization.

2.5.2 Backward Propagation Method

In some applications, the transmitted field is not specified on the metasurface plane but at some distance from the metasurface as shown in Fig. 2.8. In this case, the specified far-field can be back-propagated to the plane of the metasurface to retrieve the corresponding transmitted field [7]. To show this concept, assume the metasurface of Fig. 2.8 and the specified field at distance d_0 from the the metasurface plane. Back-propagation is a spatial Fourier domain operation. Thus, first, we compute Fourier transform of field profile $\psi(x', y'; d_0)$, i.e.

$$\tilde{\psi}(k_x, k_y; d_0) = \frac{1}{4\pi^2} \iint_{x',y'} \psi(x', y'; d_0)\, e^{-[jk_x x' + jk_y y']}\, dx'\, dy'. \tag{2.37}$$

[7] This transformation is not unique as the metasurface field may contain evanescent fields.

Next, we use the propagator [112], $\tilde{H}\left(k_x, k_y; \pm z\right) = e^{\pm j k_z z}$ [8] with $k_z = \sqrt{k^2 - k_x^2 - k_y^2}$ to back-propagate (2.37) to the plane of the metasurface, and thereby obtain $\tilde{\psi}\left(k_x, k_y; 0^+\right) = \tilde{H}\left(k_x, k_y; z\right)\tilde{\psi}\left(k_x, k_y; d_0\right)$. Finally, we take the inverse-Fourier transform to obtain the appropriate transmitted field, i.e.

$$\psi\left(x, y; 0^+\right) = \iint_{k_x, k_y} \tilde{\psi}\left(k_x, k_y; d_0\right) e^{[j k_x x + j k_y y]}\, dk_x\, dk_y. \tag{2.38}$$

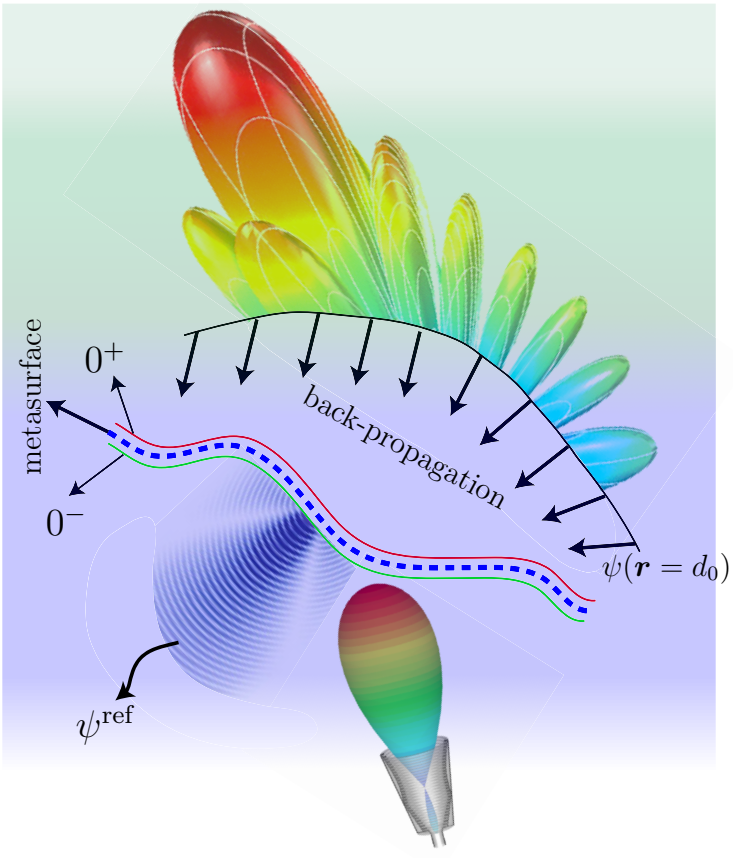

Figure 2.8 A metasurface with specified far-field at $\boldsymbol{r} = d_0$ but unknown transmitted-field at $0^+ \leq \boldsymbol{r} < d$. The incident, coming from the horn antenna here, and the reflected fields are known at $\boldsymbol{r} = 0^-$.

We demonstrate an example to show the usefulness of this technique. We show the field moving metasurface shown in Fig. 2.9. The metasurface, located at d_{ms} from the source, is used either to push a field to a farther distance or to pull a field and bring to the plane of the metasurface. In the pulling case [top right in Fig. 2.9], the incident field to the metasurface is the field of an isolated source measured at $r = d_{\text{ms}}^-$; and the transmitted field is the field

[8] We have assumed $e^{+j\omega t}$ time harmonic dependence.

of the same source measured at far distance $d_0 \gg d_{\text{ms}}$ and enforced at $r = d_{\text{ms}}^+$. The pushing case is opposite of the pulling, where having the same incident field as before, the metasurface pushes the near-field of the source measured at $d_0 \approx d_{\text{ms}}$ to a further distance $d > d_0$. We consider the pushing metasurface here, where back-propagation is needed to calculate the transmitted field on the metasurface plane ($d = d_{\text{ms}}^+$).

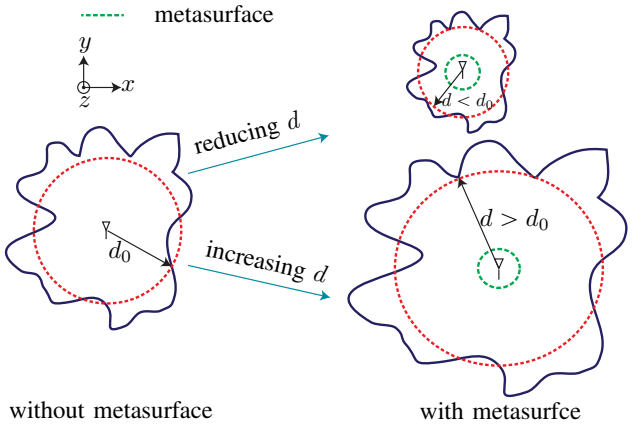

Figure 2.9 Field moving metasurface concept.

We consider an infinite line-source excitation with corresponding normalized Hankel Green function $H_0^2(k_0 r)$ radiating in free space, shown in Fig. 2.10a. We are pushing the field of the source at $d_0 = 0.3\lambda_0$ to $d = 3.3\lambda_0$ using an anisotropic metasurface at $d = 0.3\lambda_0$ on top of the source. Therefore, the specified field at $d = 3.3\lambda_0$ is back-propagated to the plane of the metasurface ($d_{\text{ms}} = d_0^+$), and using (2.27), the susceptibilities are calculated. The FDFD-GSTC, which will be explained in the next chapter, simulation result is shown in Fig. 2.10b. The discrepancy from the exact result is due to the metasurface's edge scattering and using limited Fourier terms during the back-propagation process. A similar procedure as the synthesis example in Sec. 2.5.1 can be followed for the unit-cell synthesis with just more complexity due to the fast variation of the S-parameters in this case.

However, this method is not useful in some cases, for example, in beam-forming, where a null at a direction is specified. Thence, electromagnetic inversion or inverse scattering method is used.

2.5.3 Electromagnetic Inversion Method

This technique is a generalization of the backward propagation method. In this method, the fields are unknown on the metasurface but they are specified in the far-field. Using inverse scattering method [113, 114], the electric and magnetic fields are found on the metasurface

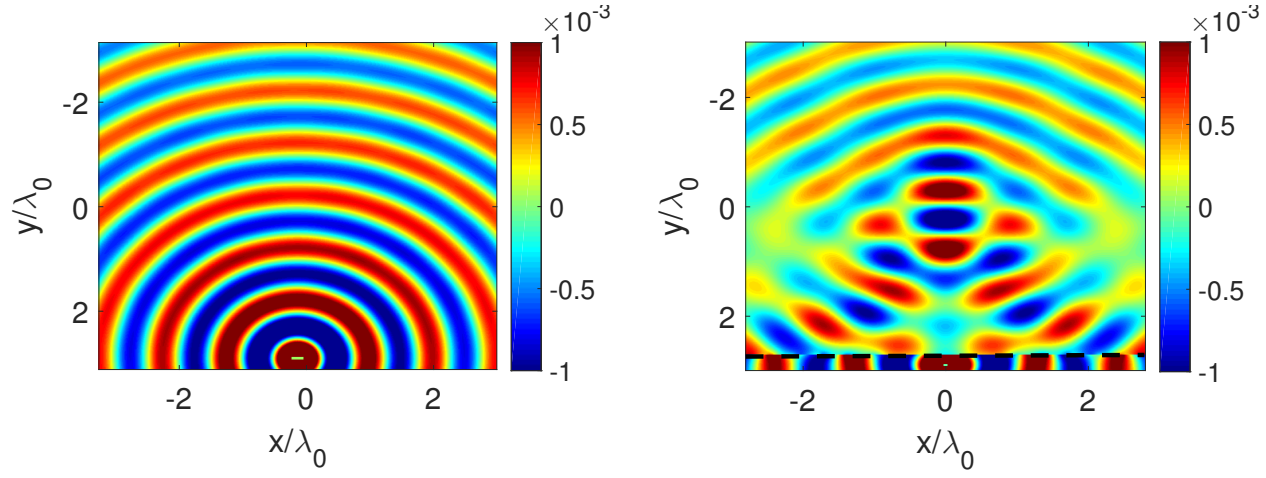

Figure 2.10 Field pushing metasurface. (a) Infinite line source radiating in free-space. (b) The metasurface, dashed black line, pushes the near field of the source to a far distance.

plane such that after their forward propagation, the specified far-fields will be retrieved. The fields are calculated using source reconstruction method (SRM) [115,116]. A brief description of this technique is given below.

Assume electric and magnetic currents in a volume V enclosed by surface S' as shown in Fig. 2.11a. The equivalent currents can be placed on the surface S' such that the original fields will be radiated outside the surface, Fig. 2.11b. Using Love's theorem [117], the fields inside the surface S' are set to zero, Fig. 2.11c. Thus, the equivalent currents on the enclosing surface will be

$$\tilde{\boldsymbol{E}}_{\mathrm{t}} = \hat{\boldsymbol{n}} \times \tilde{\boldsymbol{M}}_{\mathrm{eq}}, \qquad \tilde{\boldsymbol{H}}_{\mathrm{t}} = -\hat{\boldsymbol{n}} \times \tilde{\boldsymbol{J}}_{\mathrm{eq}}, \tag{2.39}$$

with $\boldsymbol{n}$ is the unit outward normal vector to the metasurface. The fields are calculated through

$$\tilde{\boldsymbol{E}} = \int_{S'} \left(\tilde{\boldsymbol{J}}_{\mathrm{eq}}(\boldsymbol{r}') \tilde{G}_{\mathrm{J}}(\boldsymbol{r}, \boldsymbol{r}') \right) dS' + \int_{S'} \left(\tilde{\boldsymbol{M}}_{\mathrm{eq}}(\boldsymbol{r}') \tilde{G}_{\mathrm{M}}(\boldsymbol{r}, \boldsymbol{r}') \right) dS', \tag{2.40}$$

where the first and second Integrals $\tilde{\boldsymbol{E}}_{\mathrm{J}}$ and $\tilde{\boldsymbol{E}}_{\mathrm{M}}$, respectively, are

$$\tilde{\boldsymbol{E}}_{\mathrm{J}} = -\frac{j\eta}{4\pi k} \int_{\mathrm{S}'} \left\{ k^2 \tilde{\boldsymbol{J}}_{\mathrm{eq}}(\boldsymbol{r}') \frac{e^{-jkR}}{R} + \nabla \left(\nabla . \left[\tilde{\boldsymbol{J}}_{\mathrm{eq}}(\boldsymbol{r}') \frac{e^{-jkR}}{R} \right] \right) \right\} dS' \tag{2.41}$$

$$\tilde{\boldsymbol{E}}_{\mathrm{M}} = -\frac{1}{4\pi} \nabla \times \int_{\mathrm{S}'} \tilde{\boldsymbol{M}}_{\mathrm{eq}}(\boldsymbol{r}') \frac{e^{-jkR}}{R} dS'. \tag{2.42}$$

$\tilde{G}_{\mathrm{M,J}}(\boldsymbol{r}, \boldsymbol{r}')$ is the green function of the medium; $R = |\boldsymbol{r} - \boldsymbol{r}\|$, $\boldsymbol{r}$ and $\boldsymbol{r}'$ are vectors defining position of the observation and the equivalent source point, respectively. There are numerical

techniques developed to solve them [115, 116].

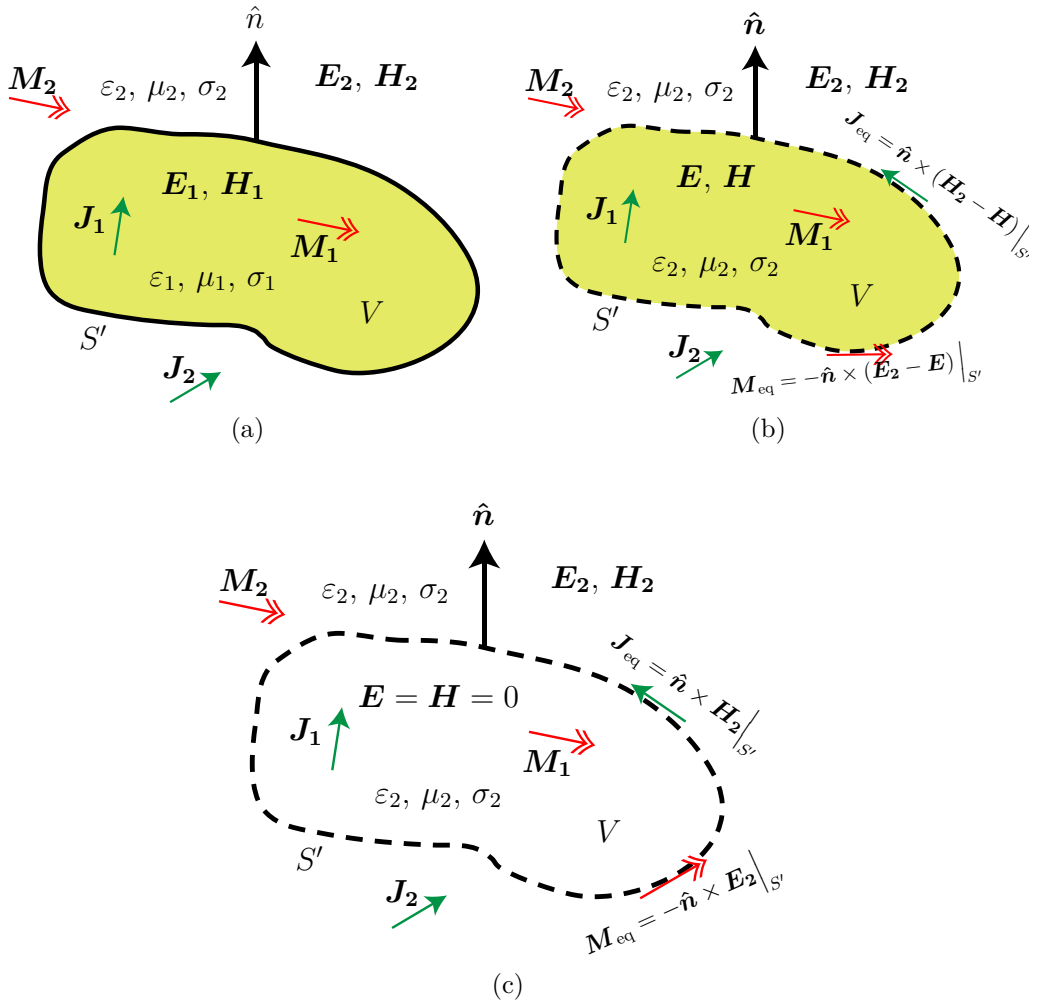

Figure 2.11 Illustration of electromagnetic equivalent theory. (a) Original Problem. (b) Equivalent problem. (c) Love's equivalent problem.

This technique, making a complementary tool beside the GSTC relations, is developed to the metasurface synthesis [118, 119]. For the set of specified incident and reflected fields, the transmitted field is calculated through (2.39). Knowing all the fields surrounding the metasurface, the susceptibilities are calculated using (2.13). It is very important to note that the reflected fields may be set to zero when applying the GSTC and, as far as the transmitted field calculated by (2.40) is used in the metasurface synthesis, the specified far-field generation is guaranteed.

Next, we show a beam-forming example [119]. The desired far-field specifications are given in Tab. 2.2. We assume plane-wave illumination of the metasurface, which is located at

$x = 0$. The far-field is enforced on a semi-circle of radius $R = 500\lambda_0$. Enforcing the Love's condition on the line $x = -\lambda/10$, the transmitted field is calculated on the reconstruction plane at $x = 0^+$ (right after the metasurface). Amplitude of the s-polarized incident plane-wave ($H_x = H_y = E_z = 0$) is modulated by a Gaussian profile to avoid edge diffraction from the metasurface. The design is performed at the frequency $f = 10$ GHz.

Table 2.2 Far-field specifications for the inverse-scattering metasurface synthesis method.

Specifications	Beam 1	Beam 2
Direction (φ)	$-30°$	$20°$
Half-power beam-width (HPBW)	$20°$	$36°$
Null direction	$20°$	$30°$

A monoisotropic metasurface, immersed in free-space, with χ_{ee}^{yy} and χ_{mm}^{zz} as the only nonzero susceptibilities are synthesized using (2.13) and shown in Fig. 2.12a. Then, using FDFD-GSTC method, the metasurface is simulated and the near-field results of Fig. 2.12b and Fig. 2.12c are obtained. To reduce the simulation time, near-field to far-field transformation is applied to the transmitted field at $x = 12\lambda_0$ line. The result of this transformation is plotted in Fig. 2.12d, which is in agreement with the specifications of Tab. 2.2.

2.5.4 Physical Realization of the Susceptibilities

Having the metasurface synthesis expression (2.13) and specified fields, the required susceptibilities can be obtained. However, this does not tell us about the shape of the inclusions required for the realization of the metasurface. Therefore, corresponding S-parameters are calculated [44] and discretized. Then, a proper unit-cell should be found that generates the required phase and amplitude of the discretized S-parameter. Note that same discretization procedure is followed when using polarzability or impedance model for the metasurface.

Depending on the metasurface synthesis and its functionality, some characteristics of the unit-cells' inclusions can be predicted as discussed in Sec. 2.3. However, finding a proper unit-cell is not straight-forward and different techniques are employed. In [54, 120] the unit-cell of Fig. 2.13a is used for the implementation of Huygens metasurfaces. Dog-bone shaped inclusions of Fig. 2.13b, can be used to implement the more general metasurfaces of non-zero reflection and transmission [121–123]. Equivalent circuit model of Fig. 2.13c with different values for Z_{e} and Z_{m} is applicable for both of these unit-cells and a look-up table for some S-parameters versus the inclusion's dimension is available in the literature. As a final step, after calculation of the proper unit-cell dimensions and juxtaposing the cells, a final optimization may be required to achieve the optimum functionality.

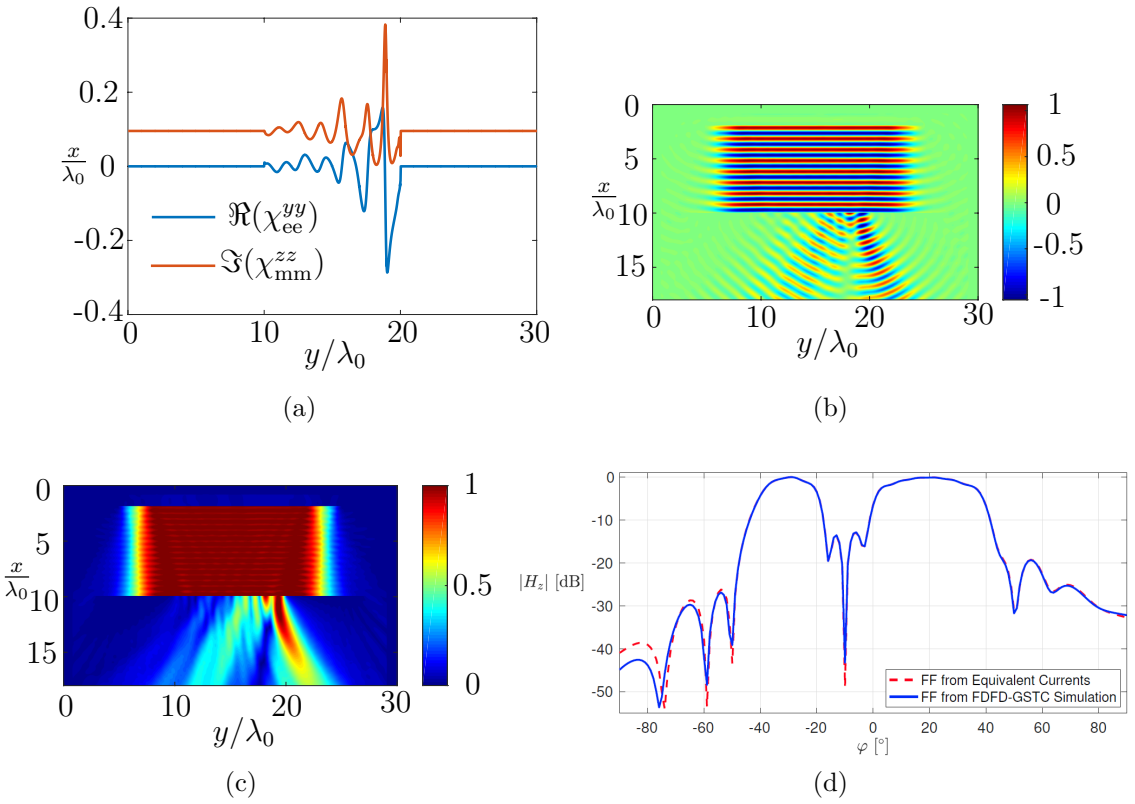

Figure 2.12 Simulation result of the metasurface synthesized using inverse-scattering method for the specifications in Tab. 2.2. (a) Real and imaginary part of the susceptibilities, where $\chi_{\mathrm{ee}}^{yy} = \chi_{\mathrm{mm}}^{zz}$ due to zero reflection. (b) 2D plot of the near-field result for $\Im(H_z)$. (c) 2D plot of the near-field result for $|H_z|$. (d) Far-field pattern.

However, there are limitation regarding the realization of the synthesized metasurface. The first limitation is the impedance or S-parameters discretization, thus, the unit-cell size. To obtain a full phase coverage and entire range of the impedances and admittances in a design, a unit-cell should retain sufficient area. Consequently, this limits the unit-cell size in the plane of interaction with the incident wave to about $\frac{\lambda}{5}$.

As an example, consider the simple case of reflectionless negative refraction metasurface with $\theta^{\mathrm{inc}} = -80°$ and $\theta^{\mathrm{tr}} = +80°$, where θ^{inc} and θ^{tr} are the incident and transmitted plane-waves directions, respectively. It is proved that a diffractionless refractive metasurface can be achieved by either a combination of gain and loss or bianisotropy [80]. The later is preferred since is does not require active elements. Based on this point, we select $\chi_{\mathrm{ee}}^{yy}, \chi_{\mathrm{mm}}^{zz}, \chi_{\mathrm{em}}^{yz}$ and χ_{me}^{zy} the none-zero susceptibility components. Inserting the plane-wave fields in (2.13) gives the unknown susceptibilities through which the S-parameters are calculated using (2.34) and plotted in Fig. 2.14. It can be seen from this figure that the variation in the phase and

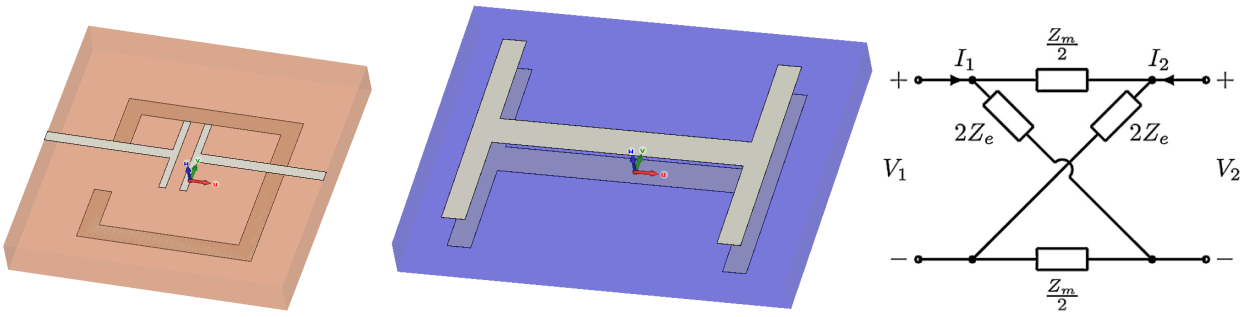

(a) (b) (c)

Figure 2.13 Generally used unit-cells for the metasurface realization. (a) Unit-cell for Huygen's metasurface. (b) Dog-bone shape unit-cell. (c) Equivalent circuit model for the mentioned unit-cells.

amplitude of the susceptibility is too fast per wavelength. For example, $\angle S_{11}^{yy}$ periodicity is 0.244λ and assuming $\frac{\lambda}{5}$ unit-cell size, which is a common choice, approximately one unit-cell is fittable.

A possible solution is to use multiple cascaded metasurfaces [9] and share the transformation burden between them, which is similar to the concept mentioned in the next paragraph.

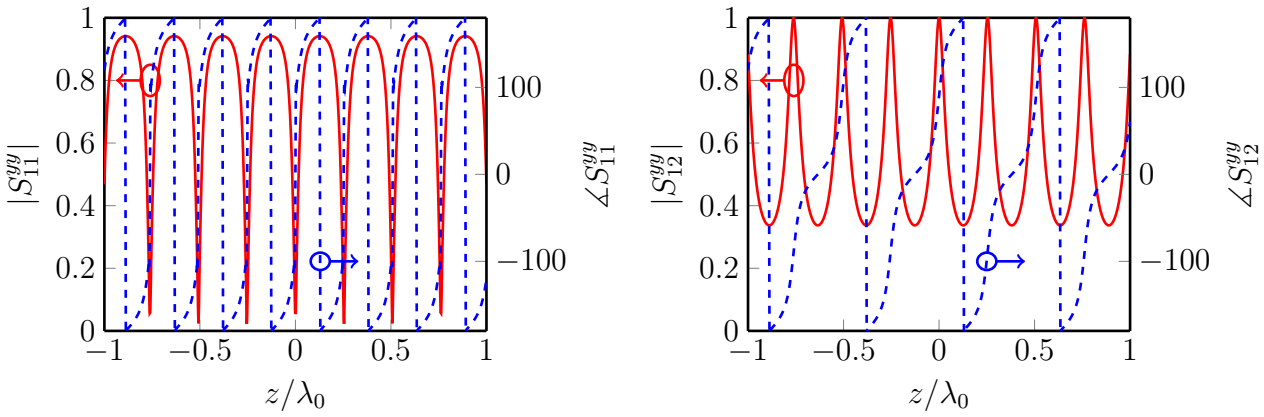

(a) (b)

Figure 2.14 S-parameters phase and amplitude variation for a metasurface transforming $\theta^{\text{inc}} = 80^\circ$ into $\theta^{\text{tr}} = -80^\circ$. (a) S_{11}^{yy}. (b) S_{12}^{yy}.

Moreover, bianisotropic metasurfaces have the local power conservation condition. This limits

[9]Note that this is different from the cascaded metasurface concept, where they cascaded multiple impedance sheets to build a single metasurface. However, we are proposing cascaded of many metasurfaces, each of which may be made of multiple cascaded sheets.

applicability of bianisotropy in the applications with different power distributions at the input and output of the metasurface; for example, a dipole field transformation into a plane wave [124]. This transformation is shown in Fig. 2.15a. In these cases, a single bianisotropic metasurface realization requires either a lossy metasurface or reflection to compensate the power shortage on the input side of the metasurface. In [124, 125] two metasurfaces are cascaded to tackle this problem as shown in 2.15b. The first metasurface redistribute the input power. To avoid coupling between the metasurface and distribute the input power more evenly in the space, the two metasurfaces are positioned at some distance from each other. Finally, the second metasurface generates the desired field, here a plane wave. As a result of this solution, looking at the input and the output planes, the total power is conserved instead of the local power. A drawback of this solution is significantly thick structure which eliminates the reduced thickness benefit of the metasurface.

2.6 Metasurface Analysis

There is great motivation among researchers working on metasurfaces to develop an efficient tool for the metasurface analysis. Initial methods were approximate and applicable to particular type of metasurfaces. Equivalent conductivity method (ECM) was developed [126, 127] to simulate periodic metasurfaces with graphene patch inclusions sandwiched between two media with dielectric constants ε_1 and ε_2 and excited at angle θ_i by a perpendicularly polarized incident wave with propagation constant k in the direction of the illumination as shown in Fig. 2.16. To attribute an equivalent conductivity to the metasurface, an equivalent graphene nano-disk model [128, 129] is employed. The reflection coefficient of such metasurface is [126]

$$r = \frac{\sqrt{\varepsilon_1}\cos\theta_i - \sqrt{\varepsilon_2}\cos\theta_t - \eta_0\sigma_\mathrm{e}}{\sqrt{\varepsilon_1}\cos\theta_i + \sqrt{\varepsilon_2}\cos\theta_t + \eta_0\sigma_\mathrm{e}}. \tag{2.43}$$

Then, solving this equation for σ_e yields

$$\sigma_\mathrm{e} = \frac{\sqrt{\varepsilon_1}\cos\theta_i - \sqrt{\varepsilon_2}\cos\theta_t - r\left(\sqrt{\varepsilon_1}\cos\theta_i + \sqrt{\varepsilon_2}\cos\theta_t\right)}{\eta_0\left(1+r\right)} \tag{2.44}$$

Finally, the calculated equivalent conductivity of the metasurface can be used in Maxwell equations to find the unknown fields.

This technique have numerous restrictions compared to the general metasurfaces represented by the GSTC equations. In [130] they are extending this technique to the metasurfaces with different arrays of unit-cells. However, still this technique does not cover a broad range of metasurfaces such as, for example, bianisotropic, time-varying, surface-wave metasurfaces.

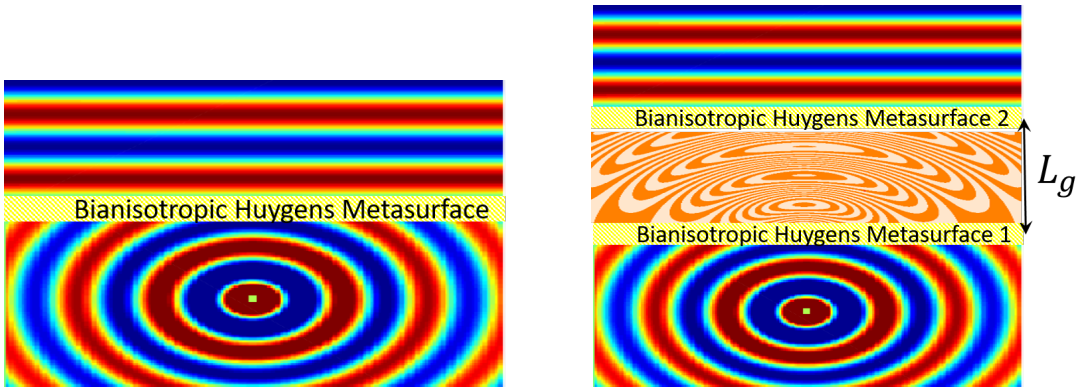

(a) (b)

Figure 2.15 Local power conservation for bianisotropic metasurface. (a) Dipole transformation into a plane wave using a single metasurface. (b) Proposed cascaded metasurface solution to alleviate the local power conservation.

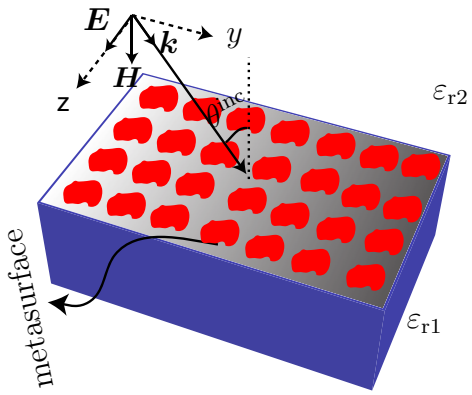

Figure 2.16 A periodic metasurface sandwiched between two media under perpendicular excitation.

An advanced, but still approximate, scheme was presented in [131–133] using MoM with IBC to model a metasurface. There is two major restrictions with this scheme. The first restriction is subwavelengthly thin slab approximation of the metasurface. Selection of proper basis function is crucial for the stability and accuracy of MoM, particularly, for a thin-layer problems. The drawbacks of that assumption will be discussed in the following paragraphs. The second restriction is that IBC is particular form of GSTCs as mentioned in Sec. 2.1. Thus, only under some conditions the MoM IBC scheme is applicable.

Other methods have been proposed in the literature, which are less efficient compared to the above-mentioned methods. Modal and multi-pole analysis technique of [134] and [135], respectively, is applicable for a periodic and mono-anisotropic metasurface under normal

excitation. It is very important to note that some authors have made a confusion between FSS structures and metasurfaces. A periodic, non-space varying, mono-anisotropic metasurface is a frequency selective surface. Therefore, it is misleading to generalize an analysis technique that is suitable only for the FSS problems to the metasurfaces.

One may consider a slab approximation of the metasurface as shown in Fig. 2.17, where the approximated susceptibility (χ_{app}) can be nonuniform in general. For the uniformly diluted susceptibility, Dirac delta function $\delta(x)$ can be approximated by a pulse function $\Pi\left(|\Delta x|\right)$ of very small width, Fig. 2.17. Therefore, the uniform approximated susceptibility is

$$\int_{-\infty}^{+\infty} \chi\delta(x)dx = \int_{-\infty}^{+\infty} \chi_{\text{app}}\Pi\left(\left|\frac{t}{2}\right|\right) dx, \tag{2.45}$$

with $\Pi(x)$ representing step function. Solving this integral, gives the χ_{app} as

$$\chi_{\text{app}} = \frac{\chi}{t}. \tag{2.46}$$

The presented approximation is valid for any scalar and tensor susceptibilities. Note that, the calculated bulk susceptibility (χ_{app}) is dimensionless as expected. Therefore, instead of a metasurface with susceptibility χ, one may simulate its corresponding diluted slab with the approximate susceptibility $\chi_{\text{app}} = \frac{\chi}{t}$.

However, the diluted slab approximation for a metasurface is not accurate [136–138]. First of all, the bulk material parameters or the susceptibility tensors are not unique and they will depend on the electrical thickness d of the bulky material. To achieve a better approximation, the thickness have to be reduced, which will result in localized field effect at the interface of the bulky metasurface and the surrounding media [137]. This approximation may even result in non-physical phenomena such as, violation of causality or an active bulky slab for a passive material.

As an example, we study the case of an absorber metasurface presented in [5] using COMSOL software. The anisotropic metasurface susceptibility with transmission coefficient T is $\chi = \chi_{\text{ee}}^{zz} = \chi_{\text{mm}}^{yy} = \frac{2j}{k}\frac{T-1}{T+1}$ [5]. Figure 2.18 shows the result of this study under normal plane wave illumination and the bulk thickness $d = \frac{\lambda}{100}$. We see that as the absorption coefficient increases, the discrepancy between the simulated and the expected result increases. One possible explanation for this phenomena is the following. Using the finest possible mesh in COMSOL, there will be one mesh element on the metasurface. The incident field, which decreases exponentially from $x = 0$ to $x = d$ inside the metasurface, should be totaly absorbed along a *single* mesh element. Therefore, very high value of lossy susceptibility is required, which should be higher than the calculated χ. However, increasing χ brings another issue

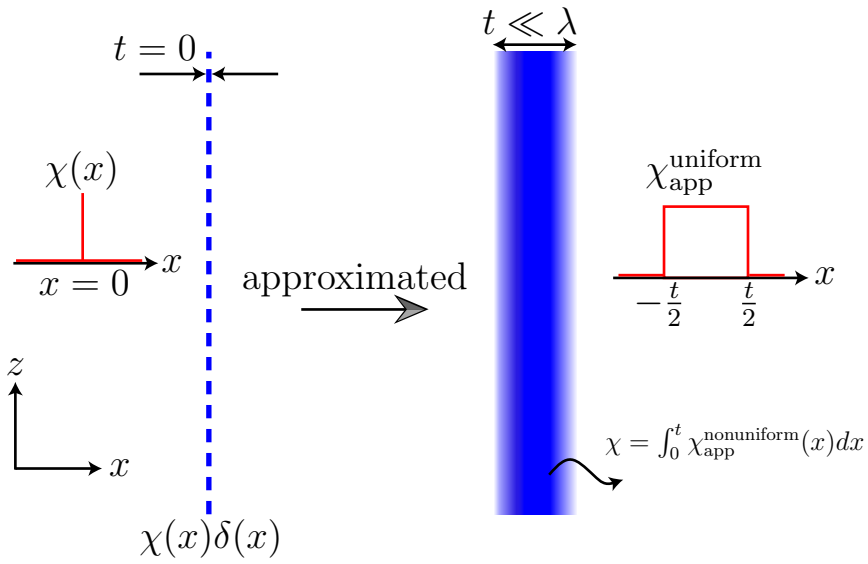

Figure 2.17 A zero thickness ($t = 0$) metasurface and its slab approximation with thickness $t \ll \lambda$.

which makes the result evermore inaccurate. The later is due to the fact that more mesh elements along the metasurface slab are needed for the simulation of higher value of χ with the same accuracy as for the previous χ. To clarify this point, we consider the simple example of two dielectrics of the same thickness, $d = \lambda$ for example, but with different permittivities, $\varepsilon_{r1} = 2$ and $\varepsilon_{r2} = 200$. It is clear that the higher dielectric material requires denser meshing and simulating $\varepsilon_{r2} = 200$ with the same mesh size of $\varepsilon_{r1} = 2$ will not yield accurate result. One may argue that by increasing χ the mesh size decreases as well. However, this takes us back to the same issue that the incident field cannot get absorbed completely inside the metasurface slab.

Therefore, computational techniques based on bulky metasurface models are not useful for their simulation and appropriate models have to be developed that treat a metasurface as a general discontinuity sheet. There are techniques developed for the analysis of simple discontinuity problems such as graphene [7] and electron gas [139]. The proposed method for the electron gas analysis is very simple and applied for a uniform 2D electron current and is not useful in our simulations. However, the method of [7], developed in FDTD scheme, is more advanced and interesting.

Since graphene is a poorly conducting single atom thickness that supports electric currents, the following BC on the conducting sheet is used

$$H_x^+ - H_x^- = \sigma_{\text{s}} E_y, \tag{2.47}$$

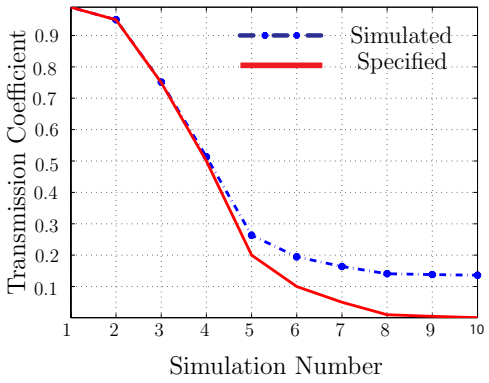

Figure 2.18 Error associated with the thickness approximation of an absorber metasurface for different transmission levels [5].

where σ_s is the graphene conductivity and H_x^+ and H_x^- are the magnetic fields on both sides of the graphene as shown in Fig. 2.19. Therefore, it introduces discontinuity on the magnetic fields. An interesting consequence of this property in FDTD analysis is that the sheet must be located only on the magnetic field nodes (H-nodes) as in Fig. 2.19. Its positioning on the electric field nodes will result in the forfeiture of the discontinuity, σ_s, since the electric field is continuous. Due to this reason, as proposed in [7], they have positioned the sheet on a magnetic field node and have defined H-nodes on its either sides to take into account the discontinuity effect of the graphene.

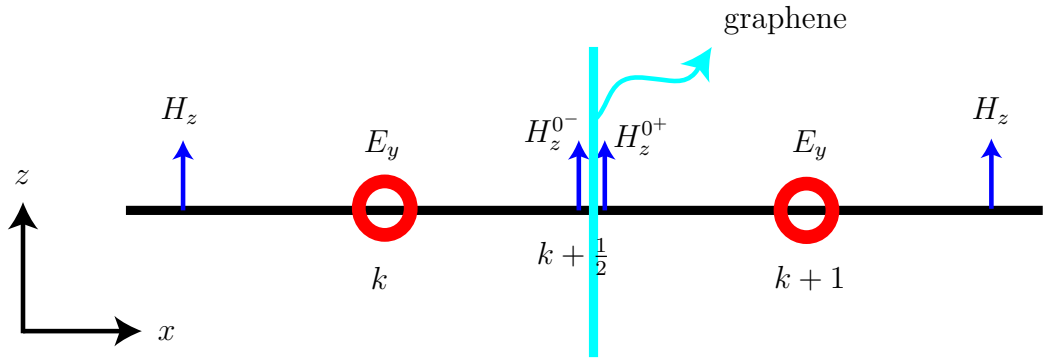

Figure 2.19 Positioning of graphene on magnetic field node in the 1D FDTD Yee grid. The sheet is illuminated from the left and the transmitted field region is the right side of the graphene.

However, this solution is not applicable to metasurface problems. To tackle the problem of general discontinuity aroused by GSTCs, we proposed a fully numeric scheme in FDFD scheme [74, 140]. This is the first scheme capable of simulating a bianisotropic and disper-

sive metasurface. Then, Finite element method (FEM) [141], boundary element method (BEM) [142] and spectral-domain method (SDM) [143] were developed by other research groups. However, their formulations are very complicated and they are not developed for the bianisotropic cases. All of these methods are frequency domain technique and they give only the steady state solution and are monochromatic. In many applications, the structure is excited by a broadband source and transient-time solutions are needed for more physical insight. Therefore, a time-domain technique must be developed.

In [144] a circuit model is developed for the design of uniform Huygens surfaces. Inspired from this, the authors of [145] and [6] developed a circuit model for the simulation of anisotropic metasurfaces, where the susceptibilities are expanded in terms of Lorentzians. An advantage of circuit-based models is that they support active elements on the surface. However, the main disadvantages of circuit models are 1- incompatibility for integration with numerical software as they are not fully numeric and require solving circuit model separately and 2- long simulation time due to big matrices and importing the results from the circuit model into FDTD 3- unapplicable to the simulation of metasurface surrounded by an scatterer. The semi-analytic method of [146] partially obviates the first two issues for a space-time modulated non-reflective and anisotropic metasurface in the steady-state.

In [147] an FDTD model for the space–time-modulated *anisotropic* metasurfaces is proposed. Albeit it is integrable with computational techniques, solving big matrices at each FDTD time-step makes it inefficient regarding both the simulation time and memory. The Floquet analysis of [148, 149] provides steady-state solution for a transparent space-time modulated metasurfaces with slowly-varying spatial anisotropic surface susceptibility [150]. Hitherto, the problem is not solved completely and a fully numeric time-domain tool capable of simulating a general metasurface, i.e. space-time varying, bianisotropic and dispersive, is needed.

Initially, this issue was tackled in [75] and later, in [101], its applicability for nonlinear metasurfaces was shown. In fact, the technique of [74, 140] was adapted into time-domain with increased complexity due to staggered-time nature of the Yee grid. Whilst this is an efficient technique regarding simulation time, memory; and have the same order of accuracy as FDTD, it is not capable of simulating frequency dispersion except the simple $\frac{1}{j\omega}$ dispersion form. Then, this issue was addressed in [151] by integrating GSTC in FDTD. This technique suffers the long simulation time, resource requirement and possible accumulated error due to a matrix inversion at each time-step.

A possible solution is integrating piece-wise linear recursive convolution technique (PLRC) or auxiliary differential equation (ADE) [152], that are used for the analysis of conventional bulk dispersive materials, with GSTC-FDTD. To better understand the problem, a brief

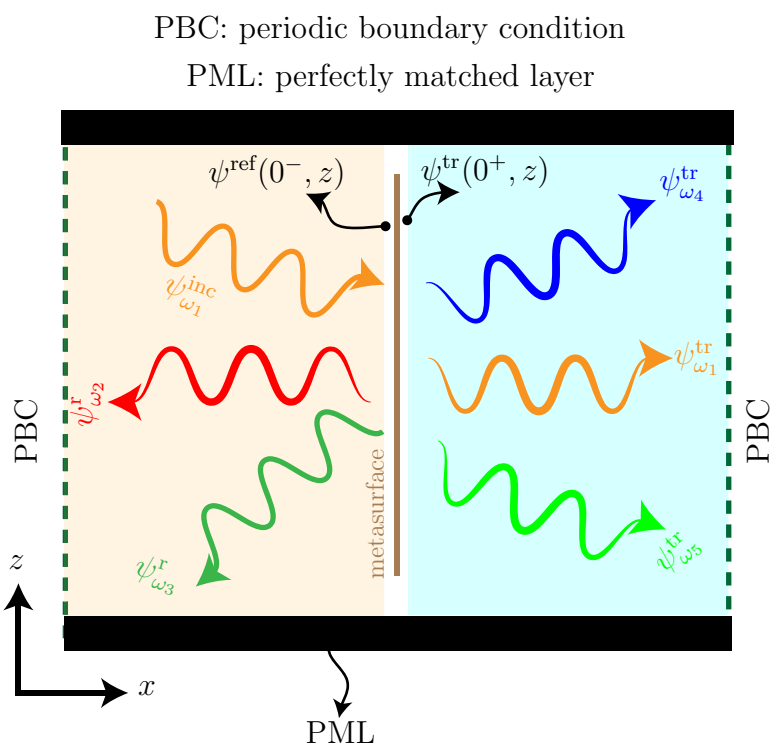

Figure 2.20 The simulation setup [6] where the $\psi^{\mathrm{ref}}(0^-,z)$ and $\psi^{\mathrm{tr}}(0^+,z)$ are calculated through an equivalent circuit and FDTD is used for the transmitted and reflected field regions.

description of PLRC and ADE is given below.

The permittivity of a Lorentz medium with L pole pairs is [152]

$$\varepsilon(\omega) = \varepsilon_{\infty,L} + \sum_{P=1}^{L} \frac{\Delta\varepsilon_p \omega_p^2}{\omega_p^2 + 2j\omega\delta_p - \omega^2}, \quad \Delta\varepsilon_p = \varepsilon_{\mathrm{s},p} - \varepsilon_{\infty,p}, \tag{2.48}$$

where $\varepsilon_{\infty,p}, \varepsilon_{\mathrm{s},p}, \omega_p$ and δ_p are the infinite frequency permittivity, static (zero-frequency) permittivity, undamped resonant frequency of the medium and damping coefficient, respectively. For the simplicity of the formulation and without loss of generality, we assume $L = 1$. In dispersive medium, the relation between the electric field and the displacement current at time t is

$$\boldsymbol{D}(t) = \varepsilon_0\varepsilon_\infty \boldsymbol{E}(t) + \varepsilon_0 \boldsymbol{E}(t) * \chi(t). \tag{2.49}$$

At time $t = n\Delta t$, where n is an integer and Δt is the time step, this relation simplifies into

$$\boldsymbol{D}^n = \varepsilon_0\varepsilon_\infty \boldsymbol{E}^n + \varepsilon_0 \int_{\tau=0}^{\tau=n\Delta t} \boldsymbol{E}(n\Delta t - \tau)\chi(\tau)d\tau. \tag{2.50}$$

Details of the discretization of (2.50) is given in [151][Sec. 9.3.1], which is

$$\boldsymbol{D}^n = \varepsilon_0\varepsilon_\infty \boldsymbol{E}^n + \varepsilon_0 \sum_{m=0}^{n-1} \left[\boldsymbol{E}^{n-m}\chi^m + \left(\boldsymbol{E}^{n-m-1} - \boldsymbol{E}^{n-m} \right) \zeta^m \right], \tag{2.51}$$

with

$$\chi^m = \int_{m\Delta t}^{(m+1)\Delta t} \chi(\tau) d\tau, \tag{2.52a}$$

$$\zeta^m = \frac{1}{\Delta t} \int_{m\Delta t}^{(m+1)\Delta t} (\tau - m\Delta t)\chi(\tau) d\tau. \tag{2.52b}$$

Substituting $\boldsymbol{D}^n$ from (2.51) into $\nabla \times \boldsymbol{H}^{n+\frac{1}{2}} = \frac{\boldsymbol{D}^{n+1} - \boldsymbol{D}^n}{\Delta t}$ yields

$$\begin{aligned} \boldsymbol{E}^{n+1} = &\left(\frac{\varepsilon_\infty - \zeta^0}{\varepsilon_\infty - \zeta^0 + \chi^0} \right) \boldsymbol{E}^n + \frac{\Delta t/\varepsilon_0}{\varepsilon_\infty - \zeta^0 + \chi^0} \nabla \times \boldsymbol{H}^{n+\frac{1}{2}} \\ &+ \frac{1}{\varepsilon_\infty - \zeta^0 + \chi^0} \sum_{m=0}^{n-1} \left[\boldsymbol{E}^{n-m} \Delta\chi^m + \left(\boldsymbol{E}^{n-m-1} - \boldsymbol{E}^{n-m} \right) \Delta\zeta^m \right], \end{aligned} \tag{2.53}$$

where $\Delta\chi^m = \chi^m - \chi^{m+1}$ and $\Delta\zeta^m = \zeta^m - \zeta^{m+1}$. The summation in (2.53) requires storing $\boldsymbol{E}, \zeta$ and χ for all times. Beside the formulation complexity, it has two major disadvantages: 1- error accumulation from all previous time steps due to integration in (2.50) and 2- huge resources requirement to store data of all time-steps. This issue will be more problematic when simulating resonant structures – which requires longer simulation time – and huge resource usage, particularly when L take larger values. Therefore, ADE scheme is used to address these issues.

In the efficient formulation of the ADE technique [153], one polarization current in frequency domain is associated with each term of (2.48) by

$$\tilde{\boldsymbol{P}}_p(\omega) = \varepsilon_0 \Delta\varepsilon_p \omega_p^2 \left(\frac{j\omega}{\omega_p^2 + 2j\omega\delta_p^2 - \omega^2} \right) \tilde{\boldsymbol{E}}(\omega). \tag{2.54}$$

Then, multiplying its both sides by the denominator of the right hand side and replacing $j\omega$ by $\frac{d}{dt}$, $-\omega^2$ by $\frac{d^2}{dt^2}$ and, finally, discretizing the resulted time-domain expression yields

$$\boldsymbol{P}_p^{n+1} = \frac{2 - \omega_p^2(\Delta t)^2}{1 + \delta_p \Delta t} \boldsymbol{P}_p^n + \frac{\delta_p \Delta t - 1}{\delta_p \Delta t + 1} \boldsymbol{P}_p^{n-1} + \frac{\varepsilon_0 \Delta\varepsilon_p \omega_p^2 (\Delta t)^2}{1 + \delta_p \Delta t} \frac{\boldsymbol{E}^{n+1} - \boldsymbol{E}^{n-1}}{2\Delta t} \tag{2.55}$$

Finally, its substation in the time domain Ampere's law gives the update equation for $\boldsymbol{E}$ as

$$\boldsymbol{E}^{n+1} \propto \boldsymbol{E}^{n-1} + \boldsymbol{E}^n + \nabla \times \boldsymbol{H}^{n+\frac{1}{2}} + \boldsymbol{P}_p^n + \boldsymbol{P}_p^{n-1} \tag{2.56}$$

The coefficients of the terms at the right side of (2.56) are given in [152][Eq. 9.79], which are removed here for the brevity and the sign $\propto$ indicates that a linear combination of the terms at the right side should be used for the exact solution. Equation (2.56) does not involve summation over all the past time steps. This is due to discretization of the corresponding differential equation of (2.54) instead of using convolution in (2.50). Therefore, ADE eliminates the PLRC problems as it requires less arithmetic operation with reduced floating point operations and smaller number of unknowns to be stored with the same second-order of accuracy as the PLRC [151].

Initially, the PLRC scheme was developed for the metasurfaces analysis in [154] and, thus, a complete analysis tool was made available. As mentioned earlier, ADE would be the most efficient analysis solution but the authors of [154] argued that ADE is not applicable for the metasurface problem. Considering the auxiliary functions defined in [152], their conclusion is completely true as with those functions the GSTC-FDTD update equations will not be discretizable in the staggered Yee grid and approximate discretization schemes will result in an inaccurate and unstable formulation.

However, in [155], we showed that by the suitable choice of auxiliary functions, the field update equations can be discretized without any approximation while being stable and accurate. Therefore, an efficient analysis tool for the general metasurface analysis was developed in [4].

2.7 Conclusion

In this chapter, we explained different classic boundary conditions and discussed their limitations and applicability conditions. It was proved that these BCs fail to represent a general metasurface discontinuity and a more advanced BC is required. We derived GSTCs using distribution theory and showed that it is the most general form of the BC; and depending on the choice of the susceptibilities, they are also capable of representing the classical BCs.

Then, we classified the metasurface GSTC synthesis techniques based on the transmitted fields location and illustrated each of them with an example. The direct synthesis method will be used during the thesis. Calculation of the unit-cell shapes was also discussed, and their essentially-required properties for a given transformation were presented. We also examined the restrictions on the metasurface unit-cell size and the local power conservation condition and their possible solutions.

Next, we discussed the metasurface analysis methods and the motivation for their development. Initially, these methods were based on conventional numerical techniques or approxi-

mate schemes and could support only limited metasurfaces while being less accurate.

Finally, we reviewed the literature on the accurate time and frequency domain methods developed for the general discontinuity. The FDFD-GSTC method is suitable for a frequency domain and dispersive metasurface simulation at a single frequency. However, it is not useful in a polychromatic simulation or for the space-time varying metasurface. We discussed the pros and cons of the developed FDTD-GSTC methods. In the following chapters, we will elaborate on the FDFD-GSTC and FDTD-GSTC methods.

CHAPTER 3 FINITE-DIFFERENCE FREQUENCY-DOMAIN GSTC ANALYSIS

In this chapter, we introduce a robust and simple technique in the finite difference frequency domain (FDFD) for the simulation of general metasurface discontinuity. We first discuss the basics of the FDFD technique. This makes the chapter standalone; therefore, readers do not need to search for the FDFD implementation in the literature. Secondly, it gives a better understanding of the developed formulations. The method of this chapter can handle general discontinuities represented in the frequency domain that are not time-varying. The results of the illustrative examples are compared with COMSOL or analytic solutions.

3.1 Introduction to FDFD Technique

Finite difference methods, due to their simplicity of implementation and formulation, are the most popular computational methods for solving Maxwell equations both in the time and frequency domain. Finite difference frequency domain (FDFD) [156, 157] is useful in the simulation of dispersive and resonant structures due to their fast convergence and calculation of the steady state solutions.

Without loss of generality, we restrict the formulation to the $\mathrm{TE_z}$ case with the non-zero E_x, E_y and H_z field components and propagation in both x and y directions as illustrated in Figs. 3.1 and 3.2 for the 1D and 2D cases, respectively. The corresponding standard Maxwell equations are [157]

$$\frac{\partial E_y}{\partial x} - \frac{\partial E_x}{\partial y} = -j\omega\mu_0\mu_{zz}(x,y)H_z \tag{3.1a}$$

$$-\frac{\partial H_z}{\partial x} = j\omega\varepsilon_0\varepsilon_{yy}(x,y)E_y \tag{3.1b}$$

$$\frac{\partial H_z}{\partial y} = j\omega\varepsilon_0\varepsilon_{xx}(x,y)E_x \tag{3.1c}$$

Using the central-difference scheme, the discretization of (3.1) yields [156]

$$\frac{E_y^{i+1,j+\frac{1}{2}} - E_y^{i,j+\frac{1}{2}}}{\Delta x} - \frac{E_x^{i+\frac{1}{2},j+1} - E_x^{i+\frac{1}{2},j}}{\Delta y} \tag{3.2a}$$
$$= -j\omega\mu_0 \mu_{zz}^{i+\frac{1}{2},j+\frac{1}{2}} H_z^{i+\frac{1}{2},j+\frac{1}{2}} \quad \text{or} \quad \boldsymbol{D}_e^x \boldsymbol{E}_y - \boldsymbol{D}_e^y \boldsymbol{E}_x = \boldsymbol{\mu}_{zz} \boldsymbol{H}_z,$$

$$-\frac{H_z^{i+\frac{1}{2},j+\frac{1}{2}} - H_z^{i-\frac{1}{2},j+\frac{1}{2}}}{\Delta x} = j\omega\varepsilon_0 \varepsilon_{yy}^{i,j+\frac{1}{2}} E_y^{i,j+\frac{1}{2}} \qquad \text{or} \quad -\boldsymbol{D}_h^x \boldsymbol{H}_z = \boldsymbol{\varepsilon}_{yy} \boldsymbol{E}_y, \tag{3.2b}$$

$$\frac{H_z^{i+\frac{1}{2},j+\frac{1}{2}} - H_z^{i+\frac{1}{2},j-\frac{1}{2}}}{\Delta y} = j\omega\varepsilon_0 \varepsilon_{xx}^{i+\frac{1}{2},j} E_x^{i+\frac{1}{2},j} \qquad \text{or} \quad \boldsymbol{D}_h^y \boldsymbol{H}_z = \boldsymbol{\varepsilon}_{xx} \boldsymbol{E}_x. \tag{3.2c}$$

Assuming n_x cells in the x direction and n_y cells in the y direction, $\boldsymbol{D}_{\mathrm{e}}^x, \boldsymbol{D}_{\mathrm{h}}^x, \boldsymbol{D}_{\mathrm{e}}^y, \boldsymbol{D}_{\mathrm{h}}^y, \boldsymbol{\varepsilon}_{xx}, \boldsymbol{\varepsilon}_{yy}$ and $\boldsymbol{\mu}_{zz}$ are square matrixes of dimension $N^2 = (n_x n_y)^2$. To avoid dealing with very large matrices and storing the zero elements, the material and field matrices are implemented in sparse form. The field quantities, $\boldsymbol{E}_y, \boldsymbol{E}_x$ and $\boldsymbol{H}_z$ are stored in column vectors of N rows. The matrix representation of $\boldsymbol{E}_y$ and $\boldsymbol{H}_z$, for example, are

$$\boldsymbol{E}_y = \begin{bmatrix} E_y^1 \\ E_y^2 \\ E_y^3 \\ \vdots \\ E_y^{N-1} \\ E_y^N \end{bmatrix}, \tag{3.3}$$

and

$$\boldsymbol{H}_z = \begin{bmatrix} H_z^1 \\ H_z^2 \\ H_z^3 \\ \vdots \\ H_z^{N-1} \\ H_z^N \end{bmatrix}, \tag{3.4}$$

repectively. The $\boldsymbol{D}_{\mathrm{h}}^{y}$, where by definition $\boldsymbol{D}_{\mathrm{h}}^{y}\boldsymbol{H}_z \equiv \frac{H_z^{i+\frac{1}{2},j+\frac{1}{2}} - H_z^{i+\frac{1}{2},j-\frac{1}{2}}}{\Delta y}$, reads

$$\boldsymbol{D}_{\mathrm{h}}^{y} = \frac{1}{\Delta y}\begin{bmatrix} -1 & 0 & \cdots & 1 & 0 & \cdots & 0 \\ 0 & -1 & 0 & \ddots & 1 & \ddots & 0 \\ 0 & 0 & \ddots & 0 & \ddots & \ddots & 0 \\ \vdots & \ddots & \ddots & -1 & \ddots & 0 & 1 \\ 0 & \ddots & \ddots & \ddots & \ddots & \vdots & \vdots \\ 0 & 0 & \cdots\cdots & 0 & -1 & 0 & \\ 0 & 0 & 0 & \cdots\cdots & 0 & -1 & \end{bmatrix}, \tag{3.5}$$

in which the -1 and 1 are the 0^{th} and n_x^{th} diagonals, respectively. Same procedure holds for the other terms in (3.2). In the 1D case, $n_x = 1$, the procedure will be the same.

In the following FDFD formulations, without loss of generality of the method, we will consider only a single transformation from the GSTC equation of (2.13) to avoid lengthy calculations and heavy notations. However, the same procedure allows a straightforward extension to the case of multiple transformations [44].

3.2 GSTC-Based Method

In this section, we do the FDFD formulation in the 1D and 2D Yee grid. We will not do the 3D extension, as it requires long and tedious equations while being straightforward without any new computational aspects. With the TE_z mode mentioned above, (2.13) simplifies into

$$-\Delta H_z = j\omega\varepsilon_0\chi_{\mathrm{ee}}^{yy}E_{y,\mathrm{av}} + jk_0\chi_{\mathrm{em}}^{yz}H_{z,\mathrm{av}}, \tag{3.6a}$$

$$-\Delta E_y = j\omega\mu_0\chi_{\mathrm{mm}}^{zz}H_{z,\mathrm{av}} + jk_0\chi_{\mathrm{me}}^{zy}E_{y,\mathrm{av}}. \tag{3.6b}$$

3.2.1 1D Computational Domain

We first consider the 1D problem (only H_z and E_y are non-zero), with propagation occurring in the x direction as shown in the Yee grid of Fig. 3.1. From (3.2), the corresponding FDFD equations are

$$\frac{E_y^{i+1} - E_y^{i}}{\Delta x} = -j\omega\mu_0\mu_{zz}^{i+\frac{1}{2}}H_z^{i+\frac{1}{2}} \quad \text{or} \quad \boldsymbol{D}_{\mathrm{e}}^{x}\boldsymbol{E}_y = \boldsymbol{\mu}_{zz}\boldsymbol{H}_z, \tag{3.7a}$$

$$-\frac{H_z^{i+\frac{1}{2}} - H_z^{i-\frac{1}{2}}}{\Delta x} = j\omega\varepsilon_0\varepsilon_{yy}^{i}E_y^{i} \quad \text{or} \quad -\boldsymbol{D}_{\mathrm{h}}^{x}\boldsymbol{H}_z = \boldsymbol{\varepsilon}_{yy}\boldsymbol{E}_y, \tag{3.7b}$$

For the mentioned 1D problem the coupling susceptibilities are zero, ($\overline{\overline{\chi}}_{\rm em} = \overline{\overline{\chi}}_{\rm me} = 0$), and (3.6) reduces to

$$-\Delta H_z = j\omega\varepsilon_0\chi_{\rm ee}^{yy}E_{y,\rm av}, \tag{3.8a}$$

$$-\Delta E_y = j\omega\mu_0\chi_{\rm mm}^{zz}H_{z,\rm av}. \tag{3.8b}$$

In the FDTD grid, a bulk material is located on the at least one E-field or H-field node, as shown in Fig. 3.1a for the H-field node. Hence, it is at least one computational grid cell thick, Δx. However, a different approach should be used for a sheet discontinuity. As mentioned in the previous chapter, the metasurface introduces a singularity on both the electric and magnetic fields. In case of a single discontinuity, one may position the structure on the H- or E-field nodes. For example, as mentioned in Sec. 2.6, for the case of graphene, introducing singularity on the magnetic field, it was positioned on the H-field node. Therefore, a metasurface can be placed neither on the H-field node nor on the E-field node. Our proposed solution is to put the metasurface between any two neighboring cells, i.e. E- and H-field nodes as shown in Fig. 3.1b where it is located between the $(d-1)^{\rm th}$ and $d^{\rm th}$ cells.

For the bulky materials simulation, ε and μ matrices take the corresponding value of the material at the position of the E- and H-field nodes, respectively. Thus, the material is introduced to the computation technique. However, treating the metasurface as a virtual structure between the nodes fails to take into account its presence in the FDFD grid since there is not any node on the metasurface and FDFD cannot realize its existence. Conventional FDFD update equations [(3.2)] are applicable everywhere in this problem except for the nodes surrounding the metasurface. This is because the conventional FDFD formulation does not take into account the presence of any material between the nodes. As an example consider the update equation (3.7a). Updating $H_z^{d+\frac{1}{2}}$ involves E_y^d and E_y^{d+1} and since there is not any structure in the space between these nodes, the FDFD equation (3.7a) is valid for updating $H_z^{d+\frac{1}{2}}$. This is in contrast to $H_z^{d-\frac{1}{2}}$ update equation, which involves E_y^{d-1} and E_y^d with a discontinuity in between. The same argument holds for E_y^{d-1} update equation in (3.7b). Consequently, a specific treatment is required to take into account the effect of the discontinuity. We propose to use the GSTC relation (3.8b) instead of the standard FDFD (3.7a). Discretizing (3.8b) leads to

$$-E_y^d + E_y^{d-1} = \frac{j\omega\mu_0\chi_{\rm mm}^{zz,(d-1/4)}}{2}\left(H_z^{d+\frac{1}{2}} + H_z^{d-\frac{1}{2}}\right). \tag{3.9}$$

This equation can be integrated with the matrix form of the FDFD only by modifying some of the coefficients of the material matrixes and the differential operators. To cast it into (3.7a),

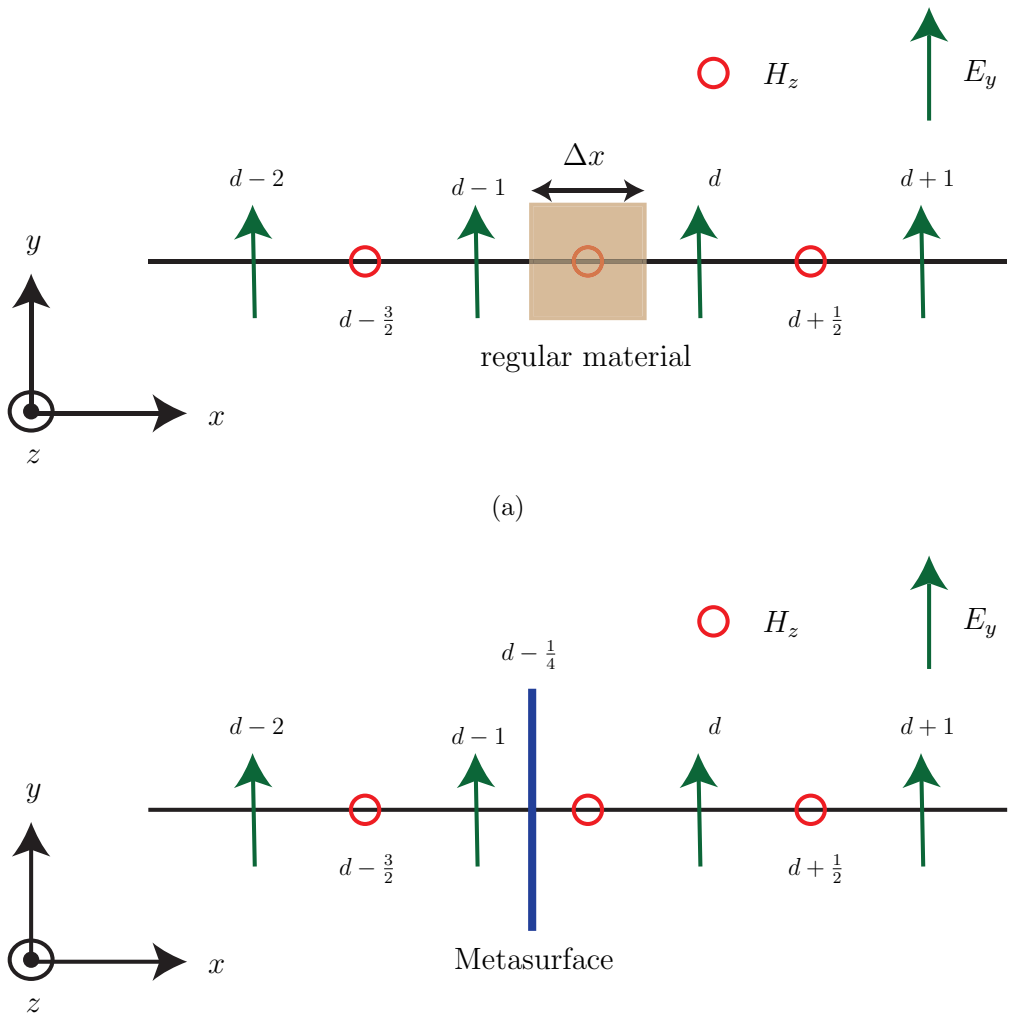

Figure 3.1 Material position in the 1D Yee grid. The E_y and H_z nodes are located at integer and half integer points, respectively. The incident wave impinges on the material from the left side and the transmitted wave exists at the right side. (a) Regular (bulk) material. (b) Metasurface sheet discontinuity.

we divide both side of (3.9) by $-1/\Delta x$ as follows

$$\frac{E_y^d - E_y^{d-1}}{\Delta x} = \frac{-j\omega\mu_0\chi_{\mathrm{mm}}^{zz,(d-1/4)}}{2\Delta x}\left(H_z^{d+\frac{1}{2}} + H_z^{d-\frac{1}{2}}\right). \tag{3.10}$$

Therefore, comparison of (3.10) and (3.7a) shows that only $\boldsymbol{\mu}_{zz}$ modification will be enough.

Therefore, we will have

$$\boldsymbol{\mu}_{zz} = \frac{-j\omega\mu_0\chi_{\mathrm{mm}}^{zz,(d-1/4)}}{2\Delta x}\begin{bmatrix} 1 & 0 & 0 & 0 & 0 & \cdots & 0 \\ 0 & 1 & 0 & 0 & 0 & \cdots & 0 \\ \vdots & \vdots & \vdots & \ddots & \ddots & \ddots & \vdots \\ 0 & 0 & 0 & 1 & 1 & \ddots & 0 \\ \vdots & \vdots & \vdots & \ddots & \ddots & \ddots & \vdots \\ 0 & 0 & 0 & \cdots & 0 & 1 & 0 \\ 0 & 0 & 0 & \cdots & 0 & 0 & 1 \end{bmatrix}, \tag{3.11}$$

where only $(d, d-1)^{\text{th}}$ element of the matrix have been altered, and all the other elements are kept unchanged.

Assuming $\mu_{zz} = \frac{\chi_{\mathrm{mm}}^{zz,(d-1/4)}}{2\Delta x}$ and revising (3.10) using this, reveals an interesting insight into the method.

$$\frac{E_y^d - E_y^{d-1}}{\Delta x} = -j\omega\mu_0\mu_{zz}H_z^{d+\frac{1}{2}} - j\omega\mu_0\mu_{zz}H_z^{d-\frac{1}{2}}. \tag{3.12}$$

The first term on the right side comes from diluting the metasurface sheet into a slab of thickness Δx with $\mu_r = \mu_{zz}$ and simulating it with conventional computational methods as performed in [5]. Then, $-j\omega\mu_0\mu_{zz}H_z^{d-\frac{1}{2}}$ is interpreted as the modification term that *compresses the diluted slab into zero-thickness.*

Now we apply the same logic to the other update equation, Eq. (3.7b), and calculate the required material matrix modification. Updating E_y^{d-1} involves $H_z^{d-\frac{1}{2}}$ and $H_z^{d-\frac{3}{2}}$ with a discontinuity in between. Thus, we replace Eq. (3.7b) by (3.8a), which gives

$$-H_z^{d-\frac{1}{2}} + H_z^{d-\frac{3}{2}} = \frac{j\omega\varepsilon_0\chi_{\mathrm{ee}}^{yy,(d-1/4)}}{2}\left(E_y^{d-1} + E_y^d\right), \tag{3.13}$$

properly accounting the effect of the discontinuity.

Similar to what we did for (3.9), we can cast this equation into (3.7b) form only by modifying the material matrix term. The resulted equation is

$$-\frac{H_z^{d-\frac{1}{2}} - H_z^{d-\frac{3}{2}}}{\Delta x} = \frac{j\omega\varepsilon_0\chi_{\mathrm{ee}}^{yy,(d-1/4)}}{2\Delta x}\left(E_y^{d-1} + E_y^d\right), \tag{3.14}$$

and its implementation requires only setting $(d-1,d)^{\text{th}}$ element to 1 as follows

$$\boldsymbol{\varepsilon}_{yy} = \frac{j\omega\varepsilon_0\chi_{\text{ee}}^{yy}}{2\Delta x}\begin{bmatrix} 1 & 0 & 0 & 0 & 0 & \cdots & 0 \\ 0 & 1 & 0 & 0 & 0 & \cdots & 0 \\ \vdots & \vdots & \vdots & \ddots & \ddots & \ddots & \vdots \\ 0 & 0 & 1 & 1 & & \ddots & 0 \\ \vdots & \vdots & \vdots & \ddots & \ddots & \ddots & \vdots \\ 0 & 0 & 0 & \cdots & 0 & 1 & 0 \\ 0 & 0 & 0 & \cdots & 0 & 0 & 1 \end{bmatrix}. \tag{3.15}$$

Similar to the previous interpretation for (3.10) applies to (3.14). The first term on the right side of (3.14) accounts for the diluted metasurface slab of thickness $2\Delta x$ and $\varepsilon_r = \frac{\chi_{\text{ee}}^{yy}}{2\Delta x}$. The second term *compresses the diluted slab into zero thickness* and corrects the scattered field.

3.2.2 2D Computational Domain

Now we extend the formulation of the previous section to the 2D Yee grid of Fig. 3.2. Therefore, in this case, the metasurface susceptibility will have space variation along y direction. For the sake of generality, we assume bianisotropic metasurface. Addition of the bianisotropy will affect the differential and material operators.

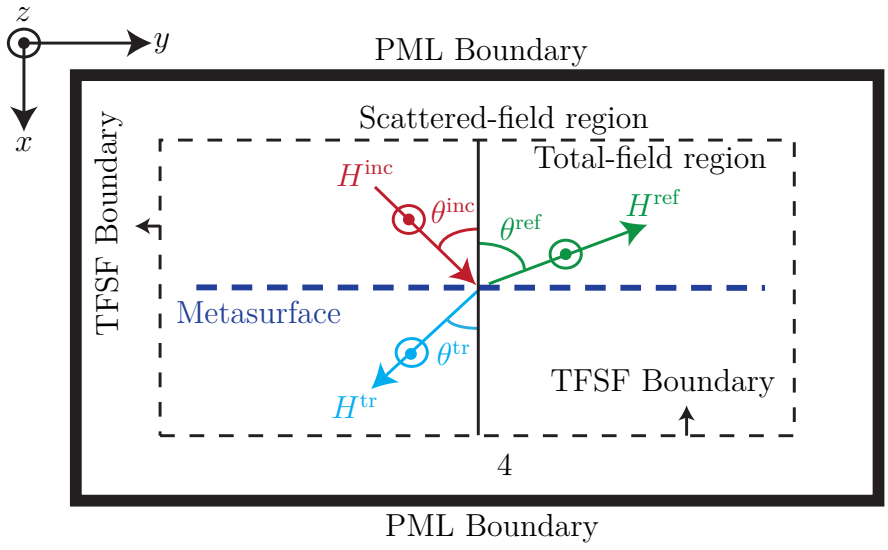

Figure 3.2 The metasurface, dashed thick blue line, immersed completely in the total-field region of the FDFD computational domain. Inside the dashed line is the total field region. The scattered field domain is the region between the dashed line and the PML (thick black line).

In the 2D FDFD Yee grid of Fig. 3.2, there are three different regions. The out layer is a PML, which absorbs all the scattered fields. The inner layer is the total-field region, where the metasurface is located. Between the PML and total-field region, there is a scattered field layer, which is separated by the total-field scattered-field (TFSF) boundary. To excite an incident field in the total field region and for some numerical facts, a minimum of one scattered-field cell is needed in the FDFD implementation [156, 157].

Similar to the 1D problem and following the arguments mentioned regarding the metasurface positioning in the solving region, we immerse it as a virtual structure between the two neighboring cells in the Yee grid, i.e. d^{th} and $(d+1)^{\text{th}}$ as shown in Fig. 3.3. Secondly, it should entirely lie in the total-field region; otherwise, undesired scattering fields will occur at the intersection of the TFSF boundary and the metasurface due to the lack of the excitation fields in the reflected region.

As in the previous section, the conventional FDFD equation, (3.2), is valid everywhere in the computational domain except for the nodes surrounding the metasurface. This is due to the presence of the metasurface discontinuity between the involved field nodes in the update equation of the E and H fields. Updating $E_y(d+1, n_b : n_l)$ involves $H_z(d+1, n_b : n_l)$ and obtaining its value requires passing over the discontinuity. To bring the effect of the discontinuity into the formulation, (3.2b) is replaced by (3.6a), which explicitly reads

$$\begin{aligned} -H_z^{\text{tr}} + H_z^{\text{inc}} + H_z^{\text{ref}} =& j\omega\varepsilon_0 \chi_{\text{ee}}^{yy} \frac{E_y^{\text{inc}} + E_y^{\text{tr}} + E_y^{\text{ref}}}{2} \\ &+ jk_0 \chi_{\text{em}}^{yz} \frac{H_z^{\text{inc}} + H_z^{\text{tr}} + H_z^{\text{ref}}}{2}. \end{aligned} \tag{3.16}$$

Discretizing this equation generates the 2D counterpart of (3.13)

$$\begin{aligned} & H_z^{d+\frac{1}{2}, j+\frac{1}{2}} \left(1 - \alpha_1(j)\right) - H_z^{d+\frac{3}{2}, j+\frac{1}{2}} \left(1 + \alpha_1(j)\right) \\ &= \frac{j\omega\varepsilon_0 \chi_{\text{ee}}^{yy,\left(d+\frac{1}{4}, j+\frac{1}{2}\right)}}{2} \left(E_y^{d, j+\frac{1}{2}} + E_y^{d+1, j+\frac{1}{2}}\right), \end{aligned} \tag{3.17a}$$

with

$$\alpha_1(j) = \frac{jk_0 \chi_{\text{em}}^{yz,\left(d+\frac{3}{4}, j+\frac{1}{2}\right)}}{2}. \tag{3.17b}$$

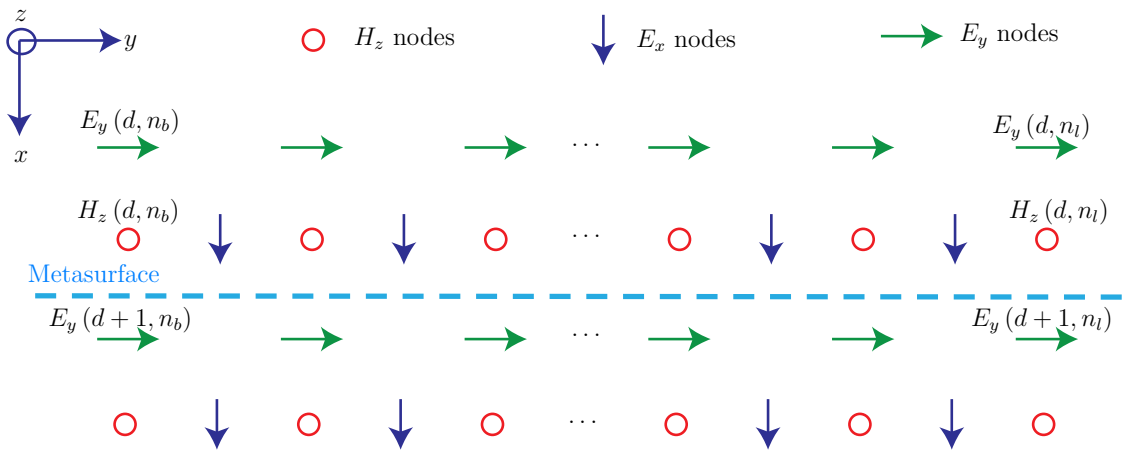

Figure 3.3 Position of the metasurface in the 2D Yee grid, between the H_z and E_y field nodes at $i = d$ from $j = n_b$ through $j = n_l$ in the y direction. As in Fig. 3.7 and Fig. 3.2, the x axis is normal to the metasurface. The numbers in parenthesis refer to the cell numbers. For instance, $E_y(d, n)$ represents the d^{th} and n^{th} cell in the x and y directions, respectively.

The same procedure is applicable for $H_z(d, n_b : n_l)$. We replace (3.2a) by (3.6b), which yields

$$\begin{aligned} -E_y^{\text{tr}} + E_y^{\text{inc}} + E_y^{\text{ref}} &= j\omega\mu_0\chi_{\text{mm}}^{zz}\frac{\left(H_z^{\text{inc}} + H_z^{\text{ref}} + H_z^{\text{tr}}\right)}{2} \\ &\quad + j\omega\sqrt{\varepsilon_0\mu_0}\chi_{\text{me}}^{zy}\frac{\left(E_y^{\text{inc}} + E_y^{\text{ref}} + E_y^{\text{tr}}\right)}{2}. \end{aligned} \tag{3.18}$$

Its discretization yields the 2D counterpart of (3.9) as

$$\begin{aligned} &E_y^{d,j+\frac{1}{2}}\left(1 - \alpha_2(j)\right) - E_y^{d+1,j+\frac{1}{2}}\left(1 + \alpha_2(j)\right) \\ &\quad = \frac{j\omega\mu_0\chi_{\text{mm}}^{zz,\left(d+\frac{3}{4},j+\frac{1}{2}\right)}}{2}\left(H_z^{d+\frac{1}{2},j+\frac{1}{2}} + H_z^{d+\frac{3}{2},j+\frac{1}{2}}\right), \end{aligned} \tag{3.19a}$$

with

$$\alpha_2(j) = \frac{jk_0\chi_{\text{me}}^{zy,\left(d+\frac{3}{4},j+\frac{1}{2}\right)}}{2}. \tag{3.19b}$$

As a general rule, conventional FDFD is valid everywhere in the solving region except at the closest E- and H-node to the metasurface where GSTCs are used. This modification of the FDFD update equations always result in the adjustment of the material matrix and, possibly, the differential operator depending on the metasurface type. In the bulk material simulation, the material matrices are diagonally sparse. While adding a metasurface behaves like a spatial dispersive material and make the material matrix non-diagonal and less sparse.

Consequently, this increases the computation time significantly.

3.3 Illustrative Examples

In this section, we prove the proposed method and formulation by 5 illustrative examples. In all of these examples, the metasurface is surrounded by free space as in Fig. 3.2 and the simulation frequency is $f = 10$ GHz and the scattered fields are absorbed by one wavelength thickness of a PML layer. The computation area dimension in the x and y directions are $20\lambda_0$ and $30\lambda_0$, respectively, with the discretization resolution of 30 cells per wavelength. The metasurface is illuminated by

$$H_z^{\text{inc}} = \exp(-jk_0x), \quad \text{and} \quad H_z^{\text{inc}} = \exp\left[-jk_0(x\cos(\theta^{inc}) + y\sin(\theta^{inc}))\right] \times \exp(-y^2), \tag{3.20}$$

in the 1D and 2D examples, respectively, where the plane-wave is modulated by the Gaussian profile in the 2D examples to eliminate the edge diffraction.

In the following examples with anisotropic metasurfaces, $\chi_{\text{me}}^{zy} = \chi_{\text{em}}^{yz} = 0$, the susceptibilities in terms of the specified incident, reflected and transmitted waves are calculated using (3.8) as

$$\chi_{\text{mm}}^{zz} = \frac{2}{j\omega\mu_0}\frac{-E_y^{\text{tr}} + E_y^{\text{ref}} + E_y^{\text{inc}}}{H_z^{\text{tr}} + H_z^{\text{inc}} + H_z^{\text{ref}}}, \tag{3.21a}$$

$$\chi_{\text{ee}}^{yy} = \frac{2}{j\omega\varepsilon_0}\frac{-H_z^{\text{tr}} + H_z^{\text{ref}} + H_z^{\text{inc}}}{E_y^{\text{tr}} + E_y^{\text{inc}} + E_y^{\text{ref}}}. \tag{3.21b}$$

3.3.1 1D Examples

The first example is a fully absorbing anisotropic metasurface, $R = T = 0$ under normal illumination. The corresponding metasurface susceptibilities, calculated using (3.21), are

$$\chi_{\text{ee}}^{yy} = \frac{2}{j\omega\varepsilon_0}\frac{H_z^{\text{inc}}}{E_y^{\text{inc}}}, \tag{3.22a}$$

$$\chi_{\text{mm}}^{zz} = \frac{2}{j\omega\mu_0}\frac{E_y^{\text{inc}}}{H_z^{\text{inc}}}. \tag{3.22b}$$

The FDFD-GSTC simulation results are presented in Fig. 3.4, where $H_z^{\text{ref}} = H_z^{\text{tr}} = 0$. Thus, the metasurface absorbs all the incident wave and shows the expected behavior. The relative error is in the order of 10^{-3}, 0.05% of the maximum amplitude of the incident wave in this example.

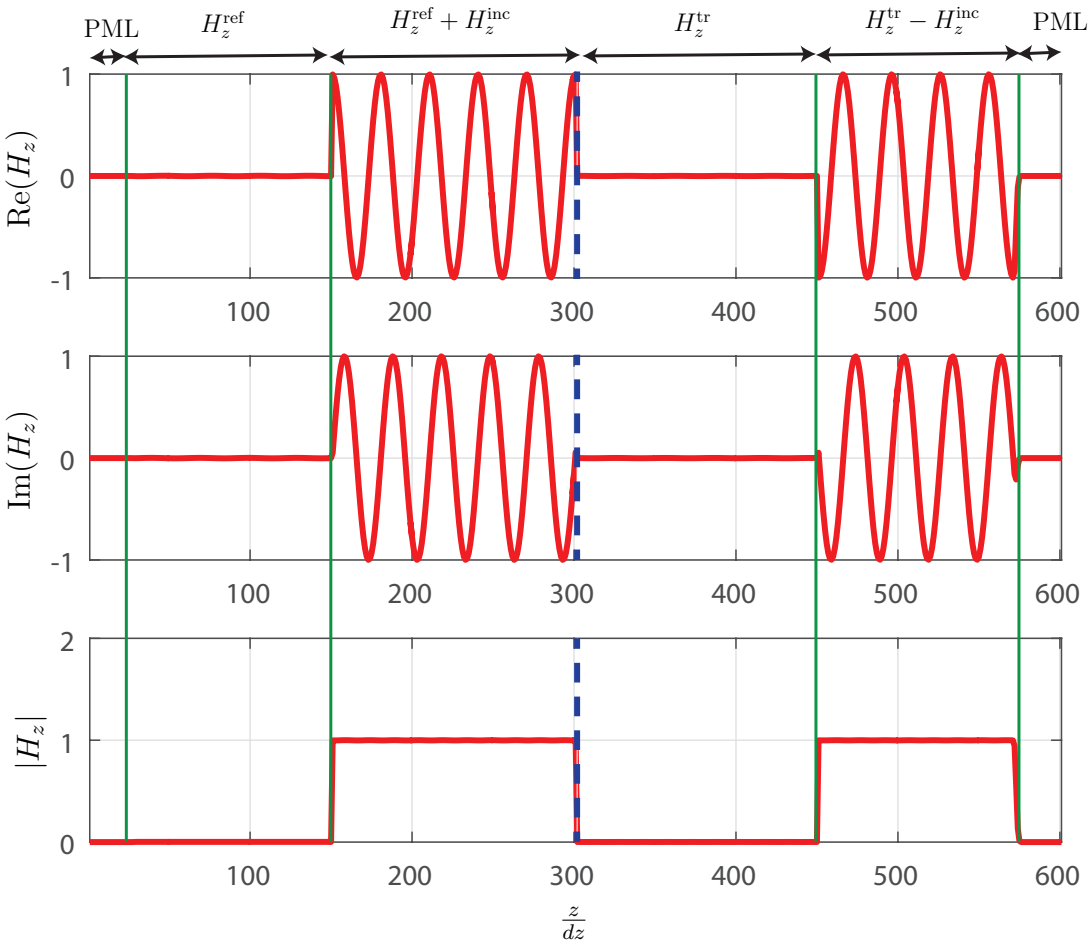

Figure 3.4 Example 1: FDFD-GSTC simulation results. Different quantities in the total field and scattered field regions are shown at the top of the figure. The metasurface, dashed blue line, is located at $\frac{z}{dz} = 300$.

The second 1D example is an anisotropic metasurface with $R = 0.3, T = 0.5$ and the rest of the power is absorbed. The metasurface susceptibilities can be from (3.8) or (3.21) as

$$\chi_{\text{ee}}^{yy} = -\frac{2}{j\omega\varepsilon_0}\frac{(-T+1+R)\,H_z^{\text{inc}}}{(1+T-R)\,E_y^{\text{inc}}}, \tag{3.23a}$$

$$\chi_{\text{mm}}^{zz} = -\frac{2}{j\omega\mu_0}\frac{(-T+1-R)\,E_y^{\text{inc}}}{(1+R+T)\,H_z^{\text{inc}}}. \tag{3.23b}$$

The simulation results are shown in Fig. 3.5. From this simulation, the reflected and transmitted wave's amplitude vary $0.300184 \leq |H_z^{\text{ref}}| \leq 0.300675$ and $0.497987 \leq |H_z^{\text{tr}}| \leq 0.502645$, respectively. The amount of error is negligible, and the results are in excellent agreement with the specifications.

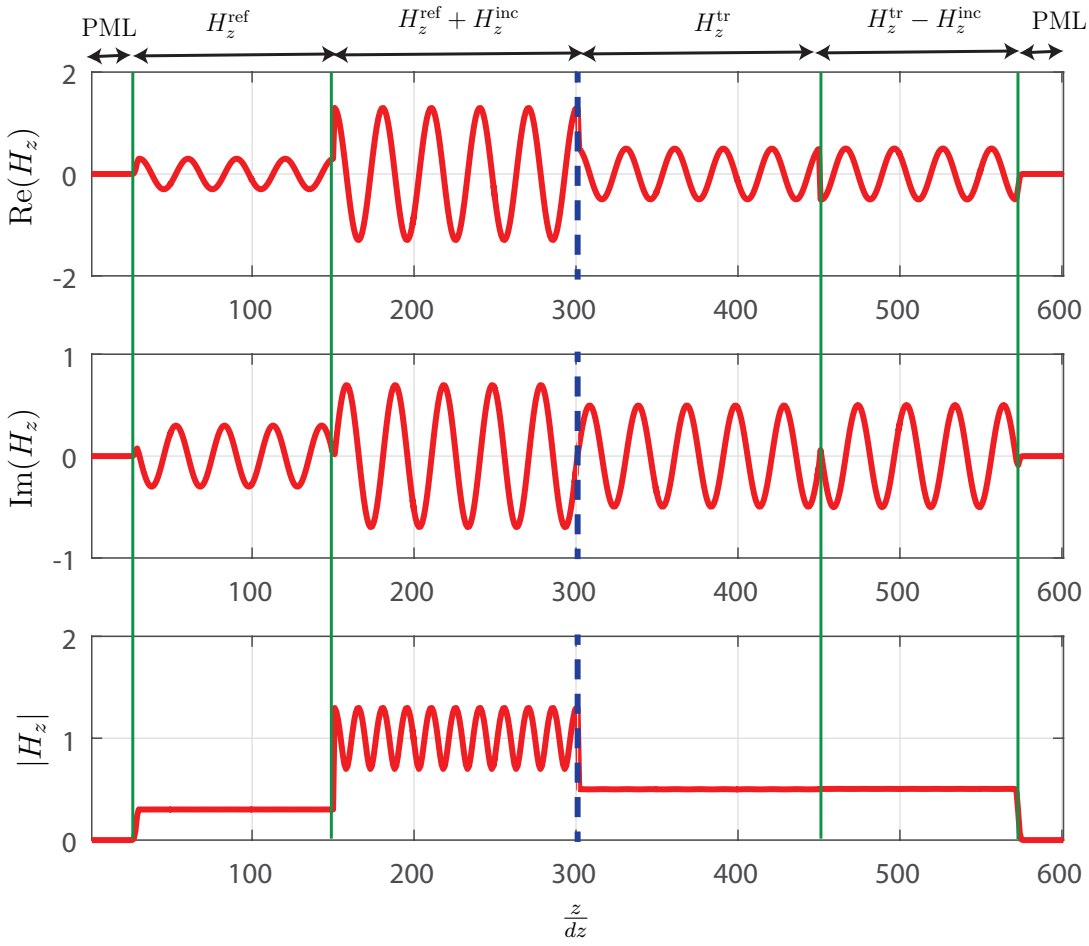

Figure 3.5 Example 2: FDFD-GSTC simulation results with normal incident wave.

3.3.2 2D Examples

The third example is a fully transparent metasurface ($R = 0$) that refracts a normally incident wave by 45°. The metasurface is synthesized using (3.21), and its simulation results are shown in Fig. 3.6. Figures 3.6a and 3.6b plots the FDFD-GSTC results, which perfectly simulate the synthesized metasurface and generates the specified fields and close to zero reflection.

To show the slab metasurface inaccuracy, we have simulated this metasurface using COMSOL [1] assuming a thickness of $d = \frac{\lambda}{100}$, and the results are plotted in Fig. 3.6d. Undesired scattered fields are clear from this simulation. They are diffraction orders that appear in any periodic structure simulation [158], which are generated in the simulated diluted metasurface of this problem and shown in Fig. 3.6c. Whereas, they should not appear in an exact simu-

[1] I have chosen COMSOL as it is the only software capable of simulating a space-varying structure, as far as I know.

lation because the synthesized metasurface makes exact matching between the incident wave and the transmitted field. Therefore, the COMSOL and other numerical software based on conventional computational technique fail to accurately simulate a sheet metasurface, while, FDFD-GSTC gives the optimal result.

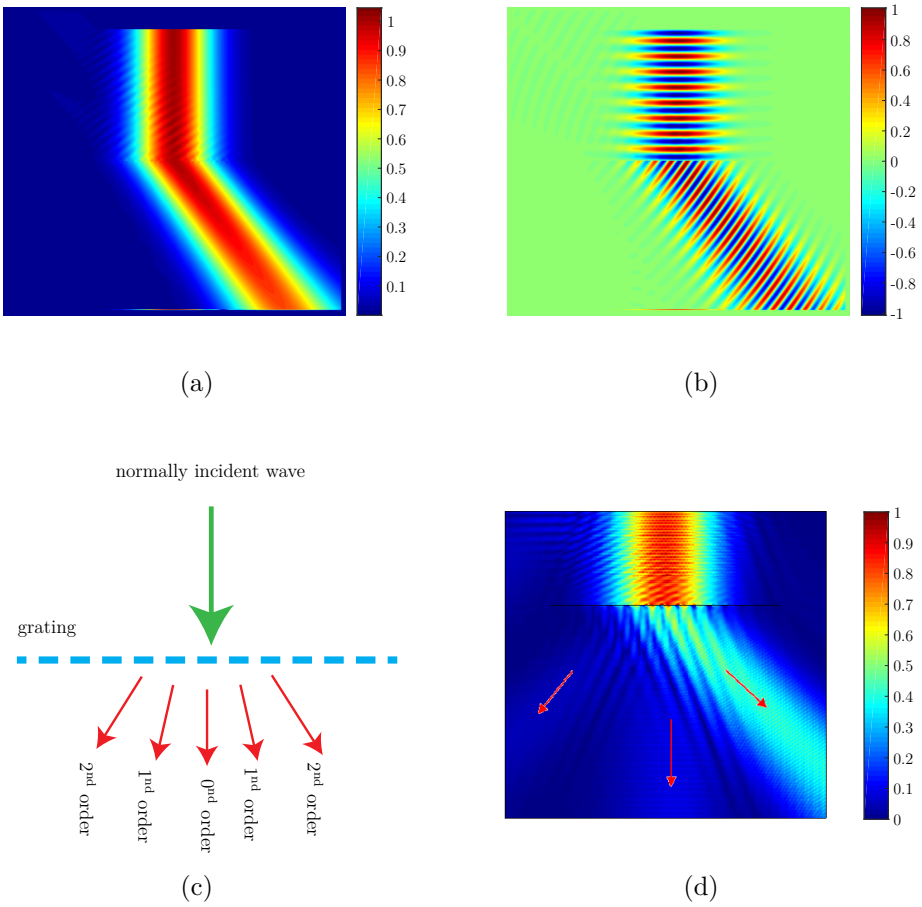

Figure 3.6 Example 3: Simulation results of the nonreflective refracting metasurface. (a) Absolute value of H_z computed by FDFD-GSTC. (b) Imaginary part. (c) Typical diffraction phenomenon in a periodic structure, such as a grating. (d) Slab approximation of the metasurface with $d = \frac{\lambda}{100}$ thickness and approximated 3D susceptibility $\frac{\bar{\bar{\chi}}}{d}$ by COMSOL.

The imaginary part of the susceptibilities of the synthesized metasurface for this example are shown in Fig. 3.7a. The figure shows that the metasurface is made of combination of loss and gain. This is essential for a diffraction-free refraction anisotropic metasurface. The reflection coefficient of Fig. 3.7b, calculated through (2.34), seems to be in contrast with the specifications and the presented 2D fields in Fig. 3.6. However, both are correct, and the non-zero S_{11} is due to the near-field of the metasurface, which does not propagate and contribute in the far-field.

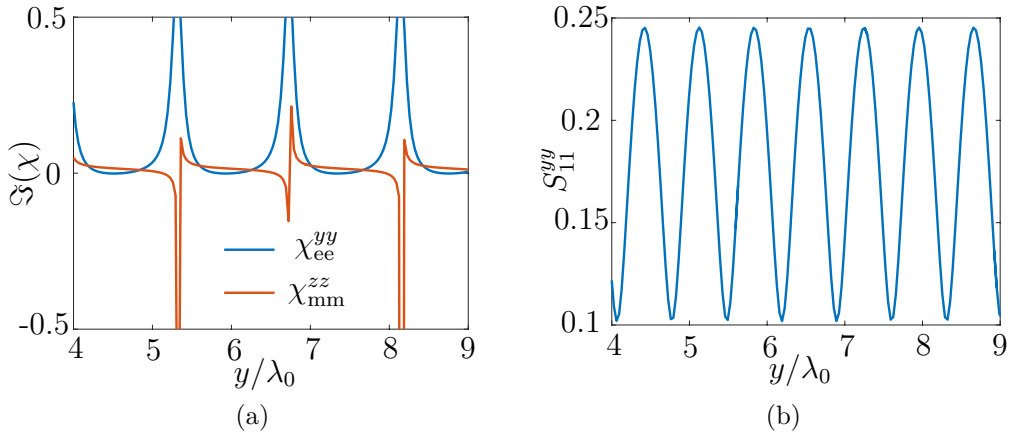

Figure 3.7 Example 1: Characteristics of the synthesized metasurface. (a) Susceptibilities. (b) Reflection coefficient (S_{11}).

The second 2D example of this section is a fully absorbing metasurface ($R = T = 0$), and its simulation results are plotted in Fig. 3.8. The FDFD-GSTC results are shown in Fig. 3.8b and 3.8a, in dB for better visualization. The scattered fields are zero, which reveals the metasurface has absorbed all the incident wave in the FDFD-GSTC simulations, shown in Figs. 3.8a and 3.8b. The same metasurface under slab approximation is simulated by COMSOL, and the result is plotted in Fig. 3.8d. It can be seen that the metasurface transmits a significant portion of the incident field and the slab approximation is invalid. In general, as shown in Fig. 3.8c and discussed in [5], the slab metasurface approach fails to simulate absorption of more than 50%. One reason for this phenomena is the impedance mismatch between the two interfaces of the metasurface slab and the surrounding free space, which generates multiple reflections within the slab and hence partly transmission of the incident wave [5] at each reflection.

As the last example, we study the surface wave routing concept using metasurfaces [159]. This concept is shown in Fig. 3.9a. It consists of a space wave coupling into a surface wave, its propagation between two points along the desired path and, finally, converting it back into a space wave, which can be different from the original space wave. The metasurface can be designed birefringent to achieve different functionality for different polarizations. For example, to refract an s-polarized (electric field parallel to the plane of the metasurface) wave and perform surface wave routing for a p-polarized wave (electric field normal to the plane of the metasurface) as in Fig 3.9a.

The details on the surface wave routing concept are given in [159]. We use this concept to design an electromagnetic periscope mentioned in that paper and shown in Fig. 3.9b. It is

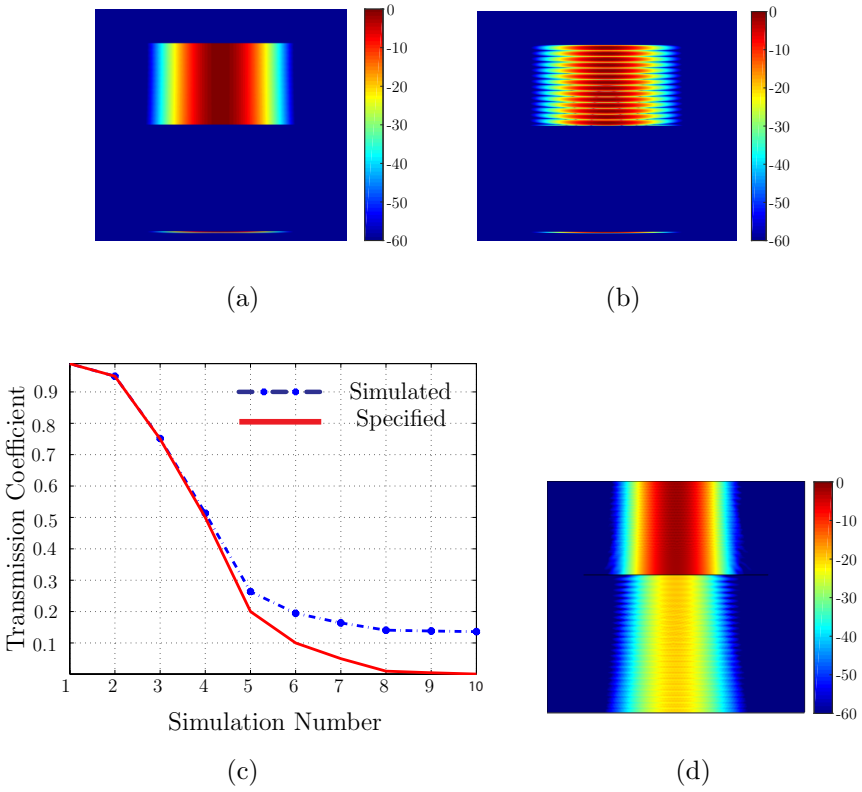

Figure 3.8 Example 4: simulation results of the fully absorptive metasurface (a) Absolute value of H_z computed by GSTC-FDFD. (b) Imaginary part. (c) Parametric study of COMSOL discrepancy versus transmission coefficient under the same conditions as in Fig. 3.6d. (d) Absolute value of H_z computed by COMSOL.

composed of three juxtaposed metasurfaces. The first metasurface is designed fully reflective ($T = 0, R = 1$) and illuminated at θ_1^{inc} angle. It couples the incident propagating wave into a surface wave and guides it on the same side as the incident field. The second metasurface routes the surface wave along its path until the desired point. This metasurface is synthesized for $\psi^{\text{inc}} = \psi^{\text{tr}} = 0$ fields and a surface wave propagating along its surface in the $z-$direction acting as the reflected wave. Finally, the last metasurface is non-reflective $\psi^{\text{ref}} = 0$ and performs the opposite function as the first metasurface, i.e. converts the surface wave into a transmitted wave with a given θ^{tr}.

We have synthesized an active electromagnetic periscope shown in Fig. 3.9b. The aim of doing this example is to verify that the FDFD-GSTC supports active susceptibility and surface-wave guiding. To avoid scattering at the connection point of the juxtaposed metasurfaces, we have specified small grazing angle, $\measuredangle\psi^{\text{inc}} = 30°$, for the incident plane wave. For the same reason, we have chosen $\measuredangle\psi^{\text{tr}} = -30°$. The synthesized anisotropic metasurface susceptibility

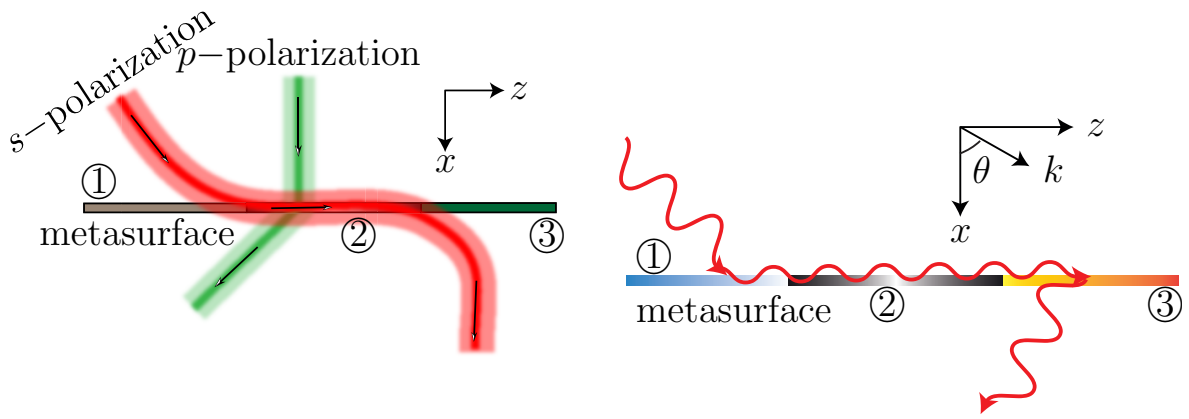

(a) (b)

Figure 3.9 Surface wave routing concept using three metasurfaces. (a) Three juxtaposed metasurfaces performing surface wave routing for $s-$polarization and refraction for $p-$polarization. (b) Electromagnetic periscope implemented by the surface wave routing concept.

is shown in Fig. 3.10 for χ_{ee}^{zz}, where $\Im(\chi_{\text{ee}}^{zz})$ is positive, thus, active. The simulation result of the periscope is depicted in Fig. 3.11. All of the metasurfaces shows the expected behavior in the simulation. There are spurious scatterings due to the coupling between the surface wave and the space wave at the connection point of the juxtaposed metasurfaces. More simulation examples on the surface wave routing using our FDFD-GSTC are presented in [159]. This example proves the robustness of the method; it treats the surface wave propagation and active susceptibility accurately.

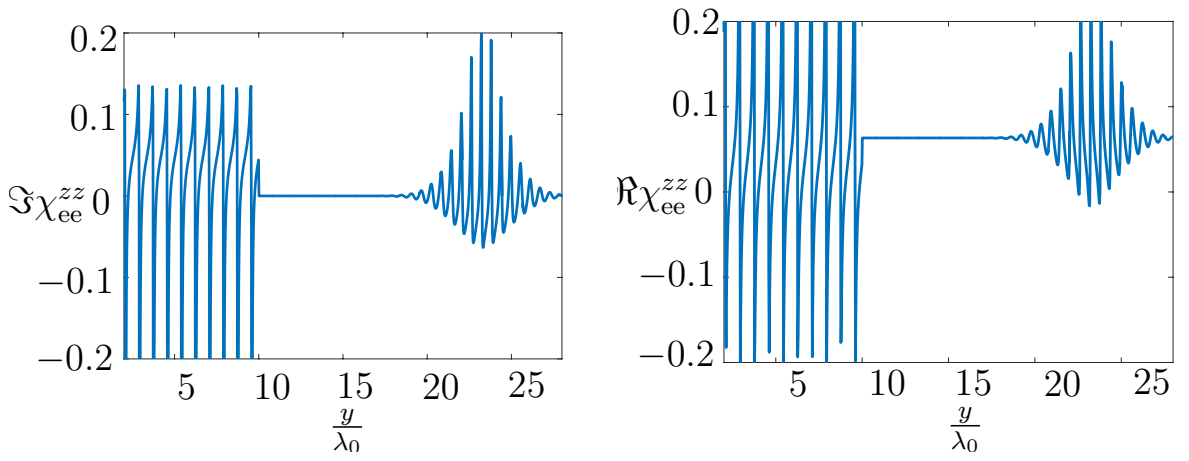

(a) (b)

Figure 3.10 Synthesized electromagnetic periscope χ_{ee}^{zz}. (a) $\Im(\chi_{\text{ee}}^{zz})$ and (b) $\Re(\chi_{\text{ee}}^{zz})$.

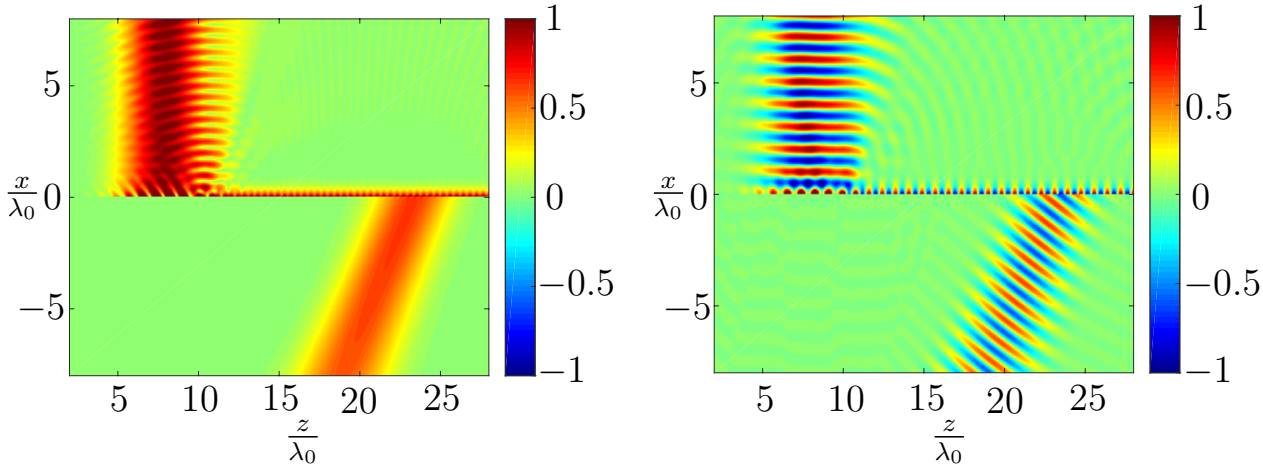

(a) (b)

Figure 3.11 Electromagnetic periscope simulation results with the metasurface located at $x = 0$. (a) $|E_z|$. (b) $\Re(E_z)$. The unexpected standing wave in these figures is due to the diffraction at the connecting point of the two metasurfaces, which partially reflects back the incident field.

3.4 Conclusion

In this chapter, we introduced a simple and robust technique for the simulation of metasurface discontinuity in the FDFD scheme. We positioned the metasurface between two neighboring cells. Conventional FDFD equations were replaced by the GSTCs to take into account the effect of the discontinuity. This adds a correction term in the FDFD-GSTC update equations that eliminate the undesired scatterings from the diluted metasurface slab approximation. The simulation were performed with 30 cells per wavelength. The simulation time with a metasurface in the computational domain increase significantly compared to the case when there is no metasurface. This is due to the non-sparse material matrices generated by adding the metasurface. However, using a home computer with 3.2GHz CPU clock and 16GB of RAM, the simulation of a single metasurface takes about 2minutes, which is acceptable. Although this technique is very accurate, however, it has limitations.

The main limitation of this technique is the frequency domain implementation. Therefore, it is not efficient in a broadband simulation. The conventional FDFD method requires the inversion of a large sparse matrix for each simulation frequency, which increases the computation time and resource requirement. FDFD-GSTC doubles this issue since the material matrix is, in general, less sparse than the conventional FDFD. Being a frequency domain method, it does not also apply to time-varying susceptibilities. Moreover, FDFD-GSTC of

this chapter is not useful for the simulation of nonlinear metasurfaces since they generate new frequency harmonics while it relates fields at the same frequency. Consequently, to address these issues, a time domain technique is required. This we will be treated in the following chapters.

CHAPTER 4 FDTD SIMULATION OF NON-DISPERSIVE METASURFACES

In this chapter, we extend the FDFD-GSTC method of the previous chapter into the time domain for the simulation of polychromatic, nonlinear and space-time varying metasurfaces. In the previous chapter, we introduced the metasurface simulation as a virtual structure. In this chapter, we present the virtual node concept. We will start with a brief discussion of the conventional FDTD technique and discretization of the Maxwell equations. Then, we discuss the simulation of metasurfaces in the staggered Yee grid of the FDTD and calculate the field update equations. Finally, we propose illustrative examples to prove the applicability of our method.

4.1 Conventional FDTD Method

For the discretization of the Maxwell equations, Yee used central-difference for the space and time partial derivatives [160]. This scheme has the second order accuracy. Assuming $(x, y, z) = (i\Delta x, j\Delta y, k\Delta z)$ at time $t = n\Delta t$, with Δt being the time step, the first partial space derivative of a function u in x-direction reads

$$\frac{\partial u}{\partial x}(i\Delta x, j\Delta y, k\Delta z; n\Delta t) = \frac{u^n_{i+\frac{1}{2},j,k} - u^n_{i-\frac{1}{2},j,k}}{\Delta x} + O[(\Delta x)^2], \tag{4.1}$$

where $u^n_{i+\frac{1}{2},j,k} = u(i\Delta x + \frac{\Delta x}{2}, j\Delta y, \Delta z; n\Delta t)$.

In the Yee algorithm, both $\overrightarrow{E}$ and $\overrightarrow{H}$ fields are calculated in the leap-frog arrangement as shown in Fig. 4.1. Consider Fig. 4.1a for the sake of simplicity. At the first integer time step ($t = 0\Delta t$), $\overrightarrow{E}$ fields are calculated in the computation region at full integer space-steps and stored in the memory. Then, we march-on-time half the time-step to $t = \frac{\Delta t}{2}$. Using the calculated $\overrightarrow{E}$ in the previous time step, $\overrightarrow{H}$ is calculated at the half-integer space-steps all over the computational domain and stored in the memory. This cycle is repeated until end of the calculation time. As can be seen form this scheme, $\overrightarrow{E}$ and $\overrightarrow{H}$ fields are interlinked and calculated at every half space- and time-step, thus, doubling the accuracy compared to the case where all the fields are measured at the same time and position. The same procedure holds for the 2D Yee grid of Fig. 4.1b and 3D case. For the sake of brevity, we are not repeating the FDTD discretization details here as they can be found in all computational electromagnetic books, for example, [47,152]. Using the mentioned leapfrog scheme and (4.1), the discretized 3D time-domain Maxwell equations are

$$E_x^{n+\frac{1}{2}}\left(i,j+\frac{1}{2},k+\frac{1}{2}\right)=E_x^{n-\frac{1}{2}}\left(i,j+\frac{1}{2},k+\frac{1}{2}\right) \tag{4.2a}$$
$$+\frac{\Delta t}{\varepsilon}\left[\frac{H_z^n(i,j+1,k+\frac{1}{2})-H_z^n(i,j,k+\frac{1}{2})}{\Delta y}-\frac{H_y^n(i,j+\frac{1}{2},k+1)-H_y^n(i,j+\frac{1}{2},k)}{\Delta z}\right],$$

$$E_y^{n+\frac{1}{2}}\left(i-\frac{1}{2},j+1,k+\frac{1}{2}\right)=E_y^{n-\frac{1}{2}}\left(i-\frac{1}{2},j+1,k+\frac{1}{2}\right) \tag{4.2b}$$
$$+\frac{\Delta t}{\varepsilon}\left[\frac{H_x^n(i-\frac{1}{2},j+1,k+1)-H_x^n(i-\frac{1}{2},j+1,k)}{\Delta z}-\frac{H_z^n(i,j+1,k+\frac{1}{2})-H_z^n(i-1,j+1,k+\frac{1}{2})}{\Delta x}\right],$$

$$E_z^{n+\frac{1}{2}}\left(i-\frac{1}{2},j+\frac{1}{2},k+1\right)=E_z^{n-\frac{1}{2}}\left(i-\frac{1}{2},j+\frac{1}{2},k+1\right) \tag{4.2c}$$
$$+\frac{\Delta t}{\varepsilon}\left[\frac{H_y^n(i,j+\frac{1}{2},k+1)-H_y^n(i-1,j+\frac{1}{2},k+1)}{\Delta x}-\frac{H_x^n(i-\frac{1}{2},j+1,k+1)-H_x^n(i-\frac{1}{2},j,k+1)}{\Delta x}\right],$$

$$H_x^{n+1}\left(i-\frac{1}{2},j+1,k+1\right)=H_x^n\left(i-\frac{1}{2},j+1,k+1\right) \tag{4.2d}$$
$$+\frac{\Delta t}{\mu}\left[\frac{E_y^{n+\frac{1}{2}}(i-\frac{1}{2},j+1,k+\frac{3}{2})-E_y^{n+\frac{1}{2}}(i-\frac{1}{2},j+1,k+\frac{1}{2})}{\Delta z}\right.$$
$$\left.-\frac{E_z^{n+\frac{1}{2}}(i-\frac{1}{2},j+\frac{3}{2},k+1)-E_z^{n+\frac{1}{2}}(i-\frac{1}{2},j+\frac{1}{2},k+1)}{\Delta y}\right],$$

$$H_y^{n+1}\left(i,j+\frac{1}{2},k+1\right)=H_y^n\left(i,j+\frac{1}{2},k+1\right) \tag{4.2e}$$
$$+\frac{\Delta t}{\mu}\left[\frac{E_z^{n+\frac{1}{2}}(i+\frac{1}{2},j+\frac{1}{2},k+1)-E_z^{n+\frac{1}{2}}(i-\frac{1}{2},j+\frac{1}{2},k+1)}{\Delta x}\right.$$
$$\left.-\frac{E_x^{n+\frac{1}{2}}(i,j+\frac{1}{2},k+\frac{3}{2})-E_x^{n+\frac{1}{2}}(i,j+\frac{1}{2},k+\frac{1}{2})}{\Delta z}\right],$$

$$H_z^{n+1}\left(i,j+1,k+\frac{1}{2}\right)=H_z^n\left(i,j+1,k+\frac{1}{2}\right) \tag{4.2f}$$
$$+\frac{\Delta t}{\mu}\left[\frac{E_x^{n+\frac{1}{2}}(i,j+\frac{3}{2},k+\frac{1}{2})-E_x^{n+\frac{1}{2}}(i,j+\frac{1}{2},k+\frac{1}{2})}{\Delta y}\right.$$
$$\left.-\frac{E_y^{n+\frac{1}{2}}(i+\frac{1}{2},j+1,k+\frac{1}{2})-E_y^{n+\frac{1}{2}}(i-\frac{1}{2},j+1,k+\frac{1}{2})}{\Delta x}\right],$$

where we have assumed the propagating occurs in a lossless homogenous medium. To reduce the calculation burden and avoid very long equations, without loss of generality, we will limit ourself to the 1D and 2D FDTD problems only.

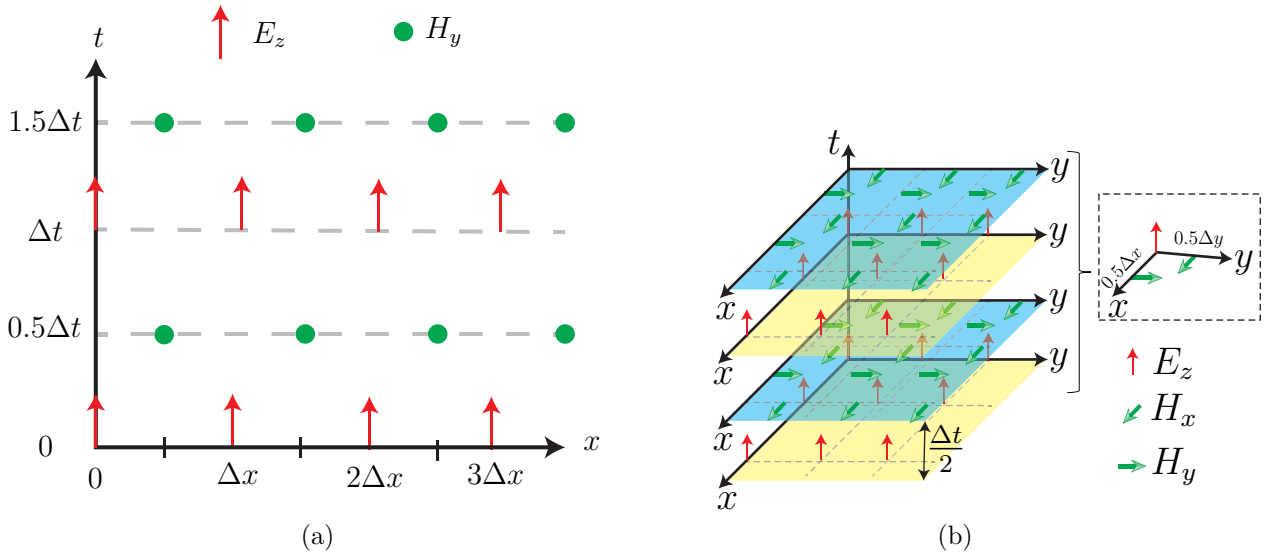

Figure 4.1 Space-time chart of the Yee's algorithm. (a) 1D space-time steps, (b) 2D space-time steps.

4.2 Space-Time Varying Metasurfce

Time domain representation of the GSTCs in (2.13) should be calculated using their inverse Fourier transform, which leads to convolution integrals. To avoid this cumbersome integrals, we assume non-dispersive metasurface, $\tilde{\chi}(\omega;t)=\chi(t)$. As a result of this simplification, using the Fourier transform property, we can replace $j\omega$ by $\frac{d}{dt}$ in (2.13) and obtain its time domain counterpart. For notational simplicity and without loss of generality, we consider here only the monoisotropic time-domain GSTCs:

$$\Delta H_y = \varepsilon_0 \frac{d\left[\chi_{\mathrm{ee}}^{zz} E_{z,\mathrm{av}}\right]}{dt}, \tag{4.3a}$$

$$\Delta E_z = \mu_0 \frac{d\left[\chi_{\mathrm{mm}}^{yy} H_{y,\mathrm{av}}\right]}{dt}. \tag{4.3b}$$

A time-varying susceptibility generally leads to the generation of new spatial an temporal frequency harmonics and possible amplification of the signal. To understand this phenomenon, we consider wave approximation from the geometrical optics

$$\tilde{\boldsymbol{E}} = \tilde{\boldsymbol{a}} e^{j\psi}, \tag{4.4}$$

where the wave amplitude, $\boldsymbol{a}$ is a slowly varying function of time and space and ψ is a space-time dependant phase. The wave vector and temporal frequency of the wave $\tilde{\boldsymbol{E}}$ is [161]

$$\boldsymbol{k} = \nabla\psi \quad \text{and} \quad \omega = -\frac{\partial\psi}{\partial t}, \tag{4.5}$$

respectively. We assume the metasurface introduces space-time varying phase shift of $\psi_{\text{ms,ref}}(x,t)$ and $\psi_{\text{ms,tr}}(x,t)$ on the reflected and transmitted fields, respectively. Phase of the scattered fields when illuminated by an incident plane wave with the phase ψ_{inc} will be

$$\psi_{\text{ref}} = \psi_{\text{inc}} + \psi_{\text{ms,ref}}(x,t) \tag{4.6}$$

$$\psi_{\text{tr}} = \psi_{\text{inc}} + \psi_{\text{ms,tr}}(x,t). \tag{4.7}$$

Using (4.5), the corresponding spatial and temporal frequencies are [162]

$$\omega_{\text{s}} = \omega_{\text{inc}} - \frac{\partial\psi_{\text{ms,s}}}{\partial t}, \tag{4.8}$$

$$k_{\text{s,x}} = k_{\text{inc,x}} + \frac{\partial\psi_{\text{ms,s}}}{\partial x}, \tag{4.9}$$

where s = r,t and inc indiactes the incident plane wave. The associated wave number of the scattered fields in $x-$direction is [162]

$$k_{\text{s,x}} = \frac{n_{\text{s}}\omega_{\text{s}}}{c} = \frac{n_{\text{s}}}{c}\left(\omega_{\text{inc}} - \frac{\partial\psi_{\text{ms,s}}}{\partial t}\right), \tag{4.10}$$

and n_{s} is the refractive index of the medium in which the wave is propagating. Equation (4.8) implies change of ω_{s} and generation of new frequencies (temporal dispersion) and (4.10) indicates change in the amplitude of the wave number $k_{\text{s,x}}$ and, consequently, spatial dispersion. General analytic calculation of the scattered fields and the related harmonics for a given space-time varying metasurface is not possible, and a numerical tool must be used. In the next section, we propose a numerical method to achieve this aim.

We assume the metasurface lies in the $y-z$ plane and is illuminated by an arbitrary wave in $-x$ direction. The susceptibility variation of a metasurface may be achieved through various tuning techniques. From example, by a carefully designed binary meta-atoms as shown in Fig. 4.2 and applying a biasing voltage enables tunning between ON and OFF states of varactor diodes [163].

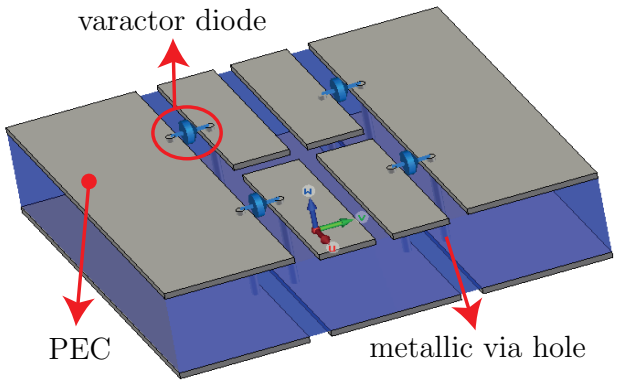

Figure 4.2 Binary patch meta-atom tuned using by varactor diodes.

4.3 1D FDTD Analysis

We first consider the 1D FDTD computational domain shown in Fig. 4.3 with propagation in $+x$ direction. The field update equations of (4.2) reduces to

$$H_y^{n+\frac{1}{2}}(i) = H_y^{n-\frac{1}{2}}(i) + \frac{\Delta t}{\mu_0 \Delta x}\left[E_z^n(i+1) - E_z^n(i)\right], \tag{4.11a}$$

$$E_z^n(i) = E_z^{n-1}(i) + \frac{\Delta t}{\varepsilon_0 \Delta x}\left[H_y^{n-\frac{1}{2}}(i) - H_y^{n-\frac{1}{2}}(i-1)\right]. \tag{4.11b}$$

This equation is valid everywhere except at the nodes around the discontinuity.

Considering the explanations in Sec. 3.2.1, to take into account the effect of the general discontinuity, the metasurface is positioned between the two neighboring cells i_d and i_d+1, where i_d is the cell number counting from the left. The region $x<0$ contain the incident and reflected waves and $x>0$ is the transmitted-wave region.

Similar to the FDFD method, the nodes around the discontinuity requires a special treatment. Consider the update equation for $E_z^n(i_d+1)$ in Fig. 4.3, which involves $H_y^{n-1/2}(i_d)$ and $H_y^{n-1/2}(i_d+1)$. Due to presence of the discontinuity, $H_y^{n-1/2}(i_d)$ cannot be used in (4.11b) because otherwise nothing will take into account the effect of the discontinuity. To solve this problem, we introduce a virtual magnetic node at $x=0^+$ and rewrite (4.11b) using this new node instead of $H_y^{n-1/2}(i_d)$ as

$$E_z^n(i_d+1) = E_z^{n-1}(i_d+1) + \frac{\Delta t}{\varepsilon_0 \Delta x}\left[H_y^{n-\frac{1}{2}}(i_d+1) - H_y^{n-\frac{1}{2}}\left(0^+\right)\right]. \tag{4.12}$$

Equation (4.3a) is used to find $H_y^{n-\frac{1}{2}}(0^+)$. Its time-domain discretization at time $t=$

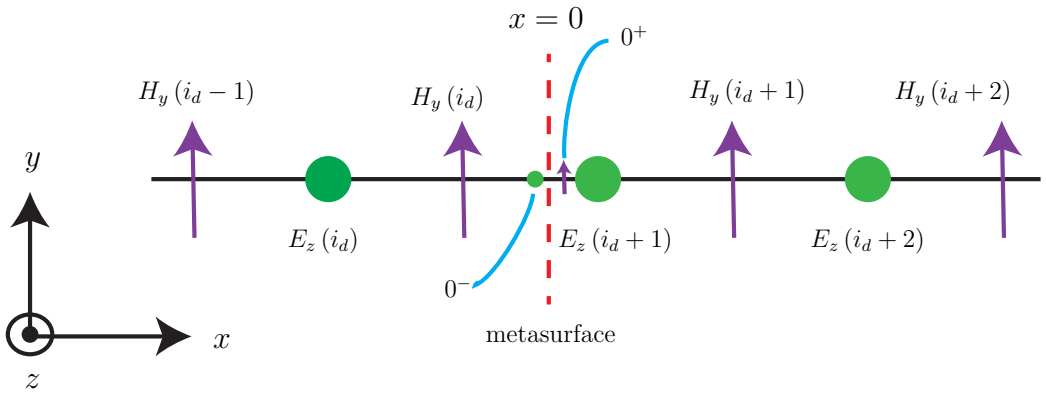

Figure 4.3 1D FDTD staggered Yee grid and position of the metasurface, solid red line, between the two neighboring E and H field nodes. The filled red and green circles represent electric and magnetic virtual nodes located just before ($x = 0^-$) and just after $x = 0^+$ the metasurface, respectively. The metasurface is illuminated from the left in the $+x$ direction.

$\left(n - \frac{1}{2}\right)\Delta t$ yields

$$H_y^{n-\frac{1}{2}}\left(0^+\right) = H_y^{n-\frac{1}{2}}\left(i_d\right) + \frac{\varepsilon_0}{\Delta t}[(\chi_{\mathrm{ee}}^{zz} E_{z,\mathrm{av}})^n - (\chi_{\mathrm{ee}}^{zz} E_{z,\mathrm{av}})^{n-1}]. \tag{4.13}$$

Then, we substitute (4.13) in (4.12) and group identical terms. The result of this calculation is

$$\begin{aligned}\left(1 + d_{\mathrm{ee}}^n\right) E_z^n\left(i_d + 1\right) = E_z^{n-1}\left(i_d + 1\right)\left(1 + d_{\mathrm{ee}}^{n-1}\right) + \\ \frac{\Delta t}{\varepsilon_0 \Delta x}\left[H_y^{n-\frac{1}{2}}\left(i_d + 1\right) - H_y^{n-\frac{1}{2}}\left(i_d\right)\right] - d_{\mathrm{ee}}^n E_z^n\left(i_d\right) + d_{\mathrm{ee}}^{n-1} E_z^{n-1}\left(i_d\right),\end{aligned} \tag{4.14}$$

where $d_{\mathrm{ee}}^n = \frac{\chi_{\mathrm{ee}}^{zz,n}}{2\Delta x}$.

Now we consider the update equation for $H_y^{n+\frac{1}{2}}\left(i_d\right)$. From (4.11a), it depends on the $E_z^n\left(i_d + 1\right)$ and $E_z^n\left(i_d\right)$ with the later being located on the other side of the discontinuity. Following the same argument as for $E_z^n\left(i_d + 1\right)$, we introduce a virtual electric node at $x = 0^-$ and rewrite the update equation (4.11a) using this new node as

$$H_y^{n+\frac{1}{2}}\left(i_d\right) = H_y^{n-\frac{1}{2}}\left(i_d\right) + \frac{\Delta t}{\mu_0 \Delta x}\left[E_z^n\left(0^-\right) - E_z^n\left(i_d\right)\right]. \tag{4.15}$$

Then, $E_z^n\left(0^-\right)$ is calculated through (4.3b), whose time-domain discretization gives

$$E_z^n\left(0^-\right) = E_z^n\left(i_d + 1\right) - \frac{\mu_0}{\Delta t}\left[(\chi_{\mathrm{mm}}^{yy} H_{y,\mathrm{av}})^{n+\frac{1}{2}} - (\chi_{\mathrm{mm}}^{yy} H_{y,\mathrm{av}})^{n-\frac{1}{2}}\right]. \tag{4.16}$$

Finally, we substitute (4.16) into (4.15) and obtain

$$\left(1+d_{\mathrm{mm}}^{n+\frac{1}{2}}\right)H_y^{n+\frac{1}{2}}(i_d)=H_y^{n-\frac{1}{2}}(i_d)\left(1+d_{\mathrm{mm}}^{n-\frac{1}{2}}\right)+ \frac{\Delta t}{\mu_0\Delta x}\left[E_z^n(i_d+1)-E_z^n(i_d)\right]-d_{\mathrm{mm}}^{n+\frac{1}{2}}H_y^{n+\frac{1}{2}}(i_d+1)+d_{\mathrm{mm}}^{n-\frac{1}{2}}H_y^{n-\frac{1}{2}}(i_d+1). \tag{4.17a}$$

with

$$d_{\mathrm{mm}}^n=\frac{\chi_{\mathrm{mm}}^{yy,n}}{2\Delta x}. \tag{4.17b}$$

Equations (4.14) and (4.17) are the E- and H-field update equations for the nodes around the metasurface. It is very important to note that the distance between the virtual nodes and its neighboring field node is $\Delta x/4$, while the distance between any two neighboring electric and magnetic field node is $\Delta x/2$. However, in calculating (4.14) and (4.17), we have approximated the first quantity by $\Delta x/2$. As we observed in our simulations, this does not have any consequence on the accuracy and stability of the resulted field update equations. Moreover, as we will see later, this approximation allows addition or removal of the metasurface without doing any change on the update equations.

Similar to the FDFD-GSTC method, the calculated update equations have interesting interpretations. Assume there is no metasurface, i.e. $\chi_{\mathrm{ee}}^{zz,n}=\chi_{\mathrm{mm}}^{yy,n}=0$. Equations (4.14) and (4.17) will reduce to the regular FDTD equations, as expected. The importance of the above approximation can be understood here. Without that approximation, when eliminating the metasurface from the computational domain, the field update equations should be modified to retrieve the conventional FDFD equations.

Another interesting case is the time-invariant susceptibilities, $\chi_{\mathrm{mm}}^{yy,n}=\chi_{\mathrm{mm}}^{yy}$ and $\chi_{\mathrm{ee}}^{zz,n}=\chi_{\mathrm{ee}}^{zz}$. Under this assumption, equations (4.14) and (4.17) reduces to

$$E_z^n(i_d+1)=E_z^{n-1}(i_d+1)+\frac{\Delta t}{\varepsilon_0\varepsilon_r\Delta x}\left[H_y^{n-\frac{1}{2}}(i_d+1)-H_y^{n-\frac{1}{2}}(i_d)\right]- \frac{\varepsilon_r-1}{\varepsilon_r}\left[E_z^n(i_d)+E_z^{n-1}(i_d)\right], \tag{4.18}$$

and

$$H_y^{n+\frac{1}{2}}(i_d)=H_y^{n-\frac{1}{2}}(i_d)+\frac{\Delta t}{\mu_0\mu_r\Delta x}\left[E_z^n(i_d+1)-E_z^n(i_d)\right]- \frac{\mu_r-1}{\mu_r}\left[H_y^{n+\frac{1}{2}}(i_d+1)+H_y^{n-\frac{1}{2}}(i_d+1)\right], \tag{4.19}$$

respectively, with $\varepsilon_r=1+\frac{\chi_{\mathrm{ee}}^{zz}}{2\Delta x}$ and $\mu_r=1+\frac{\chi_{\mathrm{mm}}^{yy}}{2\Delta x}$. In these equations, μ_r and ε_r correspond

to the volume dielectric constant of the diluted metasurface slab across a FDTD cell with thickness $2\Delta x$. Therefore, the last two terms of (4.18) and (4.19) are the modification terms that enables exact metasurface modeling. Note that the metasurface susceptibility has the unit of meter, unlike bulk material's susceptibility which is dimensionless. Division of $\chi_{\rm mm}$ and $\chi_{\rm ee}$ by $2\Delta x$ makes it dimensionless and consistent with the bulk material's unit. For a time-varying metasurface, we expect the corresponding volume dielectric constants vary in time too, which is the case if we define $\varepsilon_r^n = 1 + \frac{\chi_{\rm ee}^{zz,n}}{2\Delta x}$ and $\mu_r^n = 1 + \frac{\chi_{\rm mm}^{yy,n}}{2\Delta x}$.

Finally, for the sanity check, we can compare the calculated update equations with the conventional FDTD. In (4.2), the ε and μ of the bulk material are measured at the same location as its corresponding field node. The same holds for (4.14) and (4.17) both in time and space. For example, in (4.17a), $1 + d_{\rm mm}^{n+\frac{1}{2}}$ and $H_y^{n+\frac{1}{2}}$ both are measured at the same time, $n + \frac{1}{2}$, and tangential y and z directions.

4.3.1 2D FDTD Analysis

We now consider the 2D FDTD computational domain, shown in Fig. 4.4. To avoid lengthy and tedious formulations and without loss of the generality of the development, we solve here the TM_z problem, with E_z, H_x and H_y being the non-zero field components. The same procedure will apply to the TE_z case. Choosing $x-$axis normal to the plane of the metasurface, the field update equations in (4.2) reduce to

$$E_z^n(i,j) = E_z^{n-1}(i,j) + \frac{\Delta t}{\varepsilon_0 \Delta x}\left[H_y^{n-\frac{1}{2}}(i,j) - H_y^{n-\frac{1}{2}}(i-1,j)\right] + \frac{\Delta t}{\varepsilon_0 \Delta y}\left[H_x^{n-\frac{1}{2}}(i,j) - H_x^{n-\frac{1}{2}}(i-1,j)\right], \tag{4.20a}$$

$$H_y^{n+\frac{1}{2}}(i,j) = H_y^{n-\frac{1}{2}}(i,j) + \frac{\Delta t}{\mu_0 \Delta x}\left[E_z^n(i+1,j) - E_z^n(i,j)\right]. \tag{4.20b}$$

When taking into account the effect of the metasurface discontinuity, the main difference compared to the 1D FDTD will be the array of virtual magnetic and electric nodes as in Fig. 4.4. In (4.20a), we assume $i = i_d + 1$ and $j = j_d$, corresponding to the cell numbers after the discontinuity in Fig. 4.4. To update $E_z^n(i_d+1, j_d)$ at the node around the discontinuity, we replace $H_y^{n-\frac{1}{2}}(i_d, j_d)$ in (4.20a) with $H_y^{n-\frac{1}{2}}(0^+, j_d)$. To determine $H_y^{n-\frac{1}{2}}(0^+, j_d)$ the GSTC equation (4.3a) is discretized, which after arranging yields

$$H_y^{n-\frac{1}{2}}\left(0^+, j_d\right) = H_y^{n-\frac{1}{2}}(i_d, j_d) + \frac{\varepsilon_0}{\Delta t}\left[(\chi_{\rm ee}^{zz} E_{z,\rm av})^n - (\chi_{\rm ee}^{zz} E_{z,\rm av})^{n-1}\right], \tag{4.21}$$

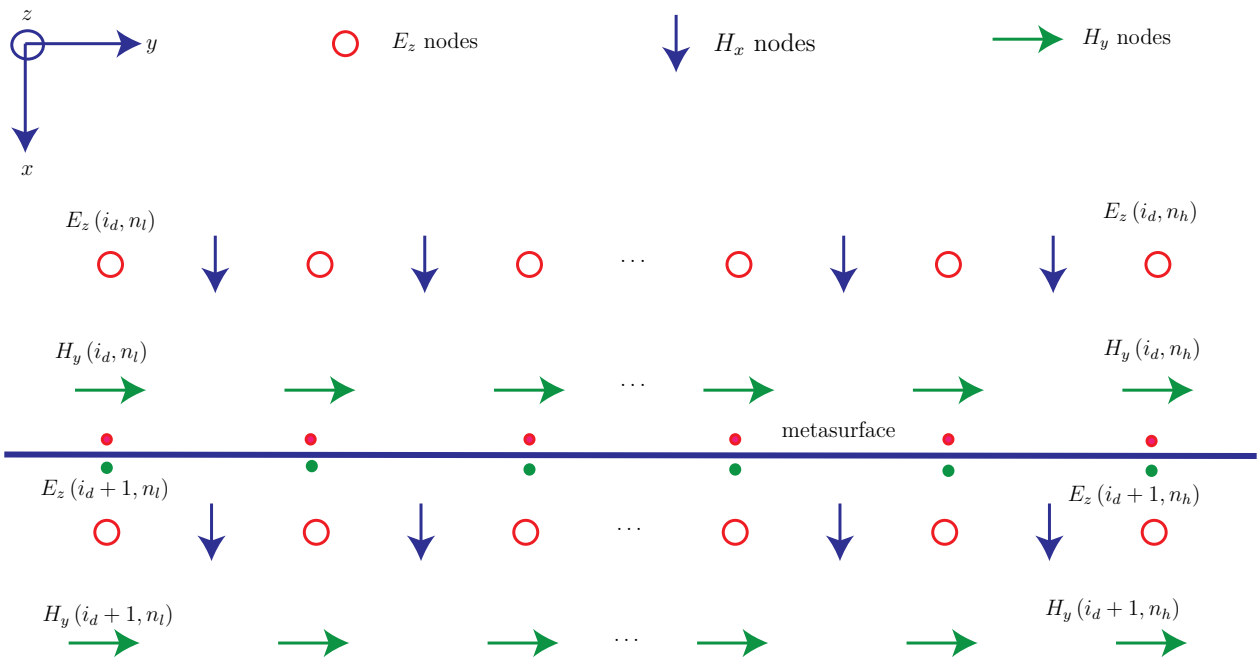

Figure 4.4 Computational domain for the 2D FDTD and the metasurface position in the grid, located between the E and H-field sampling nodes, at $x = 0$. The filled red and green circles are the electric and magnetic virtual nodes at $x = 0^-$ and $x = 0^+$, respectively. The incident wave propagates in the $xy-$plane.

the 2D counterpart of (4.13). Finally, substituting (4.21) into (4.20a) and regrouping yields the final 2D field update equation for $E_z^n\,(i_d+1, j_d)$ as

$$E_z^n\,(i_d+1, j_d)\,A_{\text{ee}}^{zz,n} = E_z^{n-1}\,(i_d+1, j_d)\,A_{\text{ee}}^{zz,n-1} + \frac{\Delta t}{\varepsilon_0 \Delta x}\left[H_y^{n-\frac{1}{2}}\,(i_d+1, j_d) - H_y^{n-\frac{1}{2}}\,(i_d, j_d)\right] + \frac{\Delta t}{\varepsilon_0 \Delta y}\left[H_x^{n-\frac{1}{2}}\,(i_d+1, j_d) - H_x^{n-\frac{1}{2}}\,(i_d+1, j_d)\right] - \frac{1}{2\Delta x}\left[\chi_{\text{ee}}^{zz,n} E_z^n\,(i_d, j_d) - \chi_{\text{ee}}^{zz,n-1} E_z^{n-1}\,(i_d, j_d)\right], \tag{4.22a}$$

with

$$d_{\text{ee}}^{zz,n} = 1 + \frac{\chi_{\text{ee}}^{zz,n}}{2\Delta x}. \tag{4.22b}$$

Similar to this, we use an array of electric virtual nodes at $x = 0^-$ and calculate $E_z^n\,(0^-, j_d)$ from (4.3b) as

$$E_z^n\left(0^-, j_d\right) = E_z^n\,(i_d+1, j_d) - \frac{\mu_0}{\Delta t}\left[(\chi_{\text{mm}}^{yy} H_{y,\text{av}})^{n+\frac{1}{2}} - (\chi_{\text{mm}}^{yy} H_{y,\text{av}})^{n-\frac{1}{2}}\right]; \tag{4.23}$$

and its substitution in (4.20b) instead of $E_z^n\left(i_d, j_d\right)$ yields,

$$H_y^{n+\frac{1}{2}}\left(i_d, j_d\right) A_m^{y,n+1} = H_y^{n-\frac{1}{2}}\left(i_d, j_d\right) A_m^{y,n-\frac{1}{2}} + \frac{\Delta t}{\mu_0 \Delta x}\left[E_z^n\left(i_d+1, j_d\right) - E_z^n\left(i_d, j_d\right)\right] - \frac{\chi_{\mathrm{mm}}^{yy,n+\frac{1}{2}}}{2\Delta x} H_y^{n+\frac{1}{2}}\left(i_d+1, j_d\right) + \frac{\chi_{\mathrm{mm}}^{yy,n-\frac{1}{2}}}{2\Delta x} H_y^{n-\frac{1}{2}}\left(i_d+1, j_d\right). \tag{4.24}$$

All the physical interpretations made for the 1D FDTD-GSTC case are valid here, too. The generalization of this technique to the 3D FDTD computational domain is straight-forward. Therefore, we are not showing the steps here for the sake of brevity.

4.4 Note on Dispersive Metasurfaces

In this case, without any loss of generality and for the sake of simplicity, we will use only $\tilde{\chi}_{ee}^{zz}$ component of the susceptibility tensor. The same conclusions hold for the cases involving other components of the susceptibility tensor.

In the time-domain formulations we presented by now, we assumed the non-dispersive metasurfaces. However, the majority of metasurfaces are dispersive due to the resonant nature of their unit-cells. Consequently, the time-domain susceptibility will also depend on the frequency, i.e. $\tilde{\chi} = \tilde{\chi}(\omega; t)$ in Sec. 4.2. In this case, the concept of the virtual node mentioned in this chapter is still valid for the dispersion simulation. However, special treatment is required as the equations are not discretizable assuming dispersion. To show this point clearly, consider the Lorentzian metasurface, $\tilde{\chi}_{ee}^{zz}(\omega) = \frac{1}{-\omega^2 + j\gamma\omega + \omega_0^2}$, for instance. Substituting this susceptibility into (2.13) yields

$$\Delta\tilde{H}_y = \frac{j\omega\varepsilon_0}{-\omega^2 + j\gamma\omega + \omega_0^2}\tilde{E}_{z,\mathrm{av}}. \tag{4.25}$$

Its discretization in time-domain at $t = \left(n - \frac{1}{2}\right)\Delta t$ is calculated by replacing $j\omega$ with $\frac{d}{dt}$, which results in

$$\frac{\Delta H_y^{n+\frac{1}{2}} - 2\Delta H_y^{n-\frac{1}{2}} + \Delta H_y^{n-\frac{3}{2}}}{2\Delta t} + \gamma\frac{\Delta H_y^n - \Delta H_y^{n-1}}{\Delta t} + \omega_0^2 \Delta H_y^{n-\frac{1}{2}} = \varepsilon_0 \frac{E_{z,\mathrm{av}}^n - E_{z,\mathrm{av}}^{n-1}}{2}. \tag{4.26}$$

Because of the staggered nature of the Yee grid, E- and H-fields are measured at full-integer and half-integer times, respectively, or vice versa [Fig. 4.1]. However, in (4.26) the H-field is needed both in half-integer and full-integer time steps. Therefore, it is not compatible

with the staggered Yee grid. There are two techniques to solve this issue, namely, ADE and PLRC [152], which is the topic of the next chapter.

We have noted that the proposed method of this chapter is still applicable when odd and even order time derivatives of the electric or magnetic field do not appear simultaneously in the time domain GSTC equation. In other words, in the frequency-domain susceptibilities $(j\omega)^{2n}$ and $(j\omega)^{2n+1}$, n is an integer, do not simultaneously appear in the denominator or nominator. We can see this point clearly in (4.26). The presence of $j\omega$ in the denominator of χ_{ee}^{zz} generates the first-order time derivation of the H-field in (4.26) and requires the magnetic field value at full-integer time steps, $\Delta H_y^n - \Delta H_y^{n-1}$, which is not available.

We now perform the formulation for the above-mentioned case in an example, where the metasurface absorbs part of the incident wave and the rest is transmitted. The susceptibility of such metasurface is calculated in (3.23), where $j\omega$ appears in the denominator. We consider susceptibilities of the form $\tilde{\chi}_{\mathrm{ee}}^{zz}(\omega) = \tilde{\chi}_{\mathrm{mm}}^{yy}(\omega) = \frac{\kappa}{j\omega}$, where κ is a constant deciding the degree of absorption. Substituting these susceptibilities into (3.8) yields

$$\Delta\tilde{H}_y = \varepsilon_0\kappa\tilde{E}_{z,\mathrm{av}}, \tag{4.27}$$

$$\Delta\tilde{E}_z = \mu_0\kappa\tilde{H}_{y,\mathrm{av}}, \tag{4.28}$$

where the frequency dependency has vanished and the discretization process is significantly simplified. The corresponding discretized time-domain equations are

$$\Delta H_y^{n-\frac{1}{2}} = \frac{\varepsilon_0\kappa}{2}\left(E_{z,\mathrm{av}}^{n} + E_{z,\mathrm{av}}^{n-1}\right), \tag{4.29a}$$

$$\Delta E_z^n = \frac{\mu_0\kappa}{2}\left(H_{y,\mathrm{av}}^{n+\frac{1}{2}} + H_{y,\mathrm{av}}^{n-\frac{1}{2}}\right). \tag{4.29b}$$

Hereafter, one can follow the mentioned steps in the previous section and obtain the final update equations. This procedure will require replacing (4.13) and (4.16) for the 1D case and (4.21) and (4.23) for the 2D case by (4.29a) and (4.29b), respectively.

4.5 Benchmark and Illustrative Examples

In this section, we present six application examples of the developed GSTC-FDTD scheme. The simulations are compared with the analytic result or by other computational techniques, whichever is possible.

4.5.1 Homogeneous Constant Metasurface

We start with the 1D computational problem with a uniform 2D metasurface. We consider a time-invariant reflection-less metasurface, therefore, equal and constant monoisotropic susceptibilities, $\chi_{\rm ee}^{zz} = \chi_{\rm mm}^{yy} = 5$. The reason for choosing this example is the availability of an analytical closed-form solution. The transmitted field for the (necessarily) normally incident and transverse electromagnetic (TEM) plane wave $H_y^{\rm inc} = \sin(\omega t - k_0 x)$ is found by solving (4.3), which gives

$$H_y^{\rm tr} = \frac{1 - \frac{k_0^2}{4}\chi_{\rm mm}^{yy}\chi_{\rm ee}^{zz}}{1 + \frac{k_0^2}{4}\chi_{\rm mm}^{yy}\chi_{\rm ee}^{zz}} \sin(\omega t - k_0 x) + \frac{1}{\eta_0} \frac{\epsilon_0 \omega \chi_{\rm ee}^{zz}}{1 + \frac{k_0^2}{4}\chi_{\rm ee}^{zz}\chi_{\rm mm}^{yy}} \cos(\omega t - k_0 x)\,. \tag{4.30}$$

The GSTC-FDTD result is plotted in Fig. 4.5 and compared with the analytic result of (4.30). The maximum discrepancy between the two solutions defined by $\left|H_y^{\rm FDTD} - H_y^{\rm analytic}\right|$ is on the order of 10^{-3} using 30 cells per wavelength. As in any computational methods, this error can be improved using finer discretization in time and space. Finally, we achieved negligible reflection from the metasurface, and all the incident power is transmitted, as was specified in the synthesis.

4.5.2 Anisotropic Sinusoidally Time-Varying Homogeneous Metasurface

We again consider the same 1D computational problem and reflection-less metasurface as in the previous example but the susceptibilities are time-varying, $\chi_{\rm ee}^{zz} = \chi_{\rm mm}^{yy} = \chi = 1 + \sin(\omega t)$, under a normal incident TEM wave $E_z = \sin(\omega t)$. Note that the reflection-less property of the metasurface is assured using the two equal susceptibilities as in the previous example. Since the susceptibilities are time-varying, we expect the generation of new frequency harmonics, and this can be inferred from the explanations of Sec 4.2 and by inspecting (4.3).

The FDTD-GSTC simulation results are shown in Fig. 4.6. Unfortunately, this example cannot be benchmarked since no commercial code can analyze such metasurface and this is the first method developed for this type of simulations. Despite of this, the results may be verified using the synthesis specifications. The reflection from the metasurface discontinuity is zero and new harmonics are generated in the transmitted wave, both of them are expected.

4.5.3 Graphene Analysis

In this example, we show that our proposed model is capable of simulating other discontinuity structures such as graphene [7]. GSTC-FDTD applies for the case of general discontinuity, where both E- and H-fields are discontinuous, and the structure is bianisotropic. Therefore,

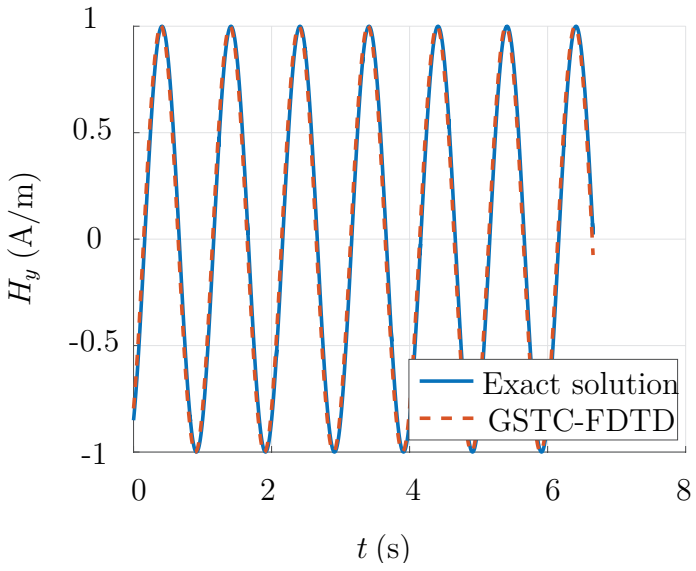

Figure 4.5 Example 1: Comparison of the GSTC-FDTD and exact analytical [Eq. (4.30)] transmitted waveforms. The solid blue and dashed red line represent the exact and simulated results, respectively. The number of the nodes per wavelength is $N_{\text{res}} = 30$.

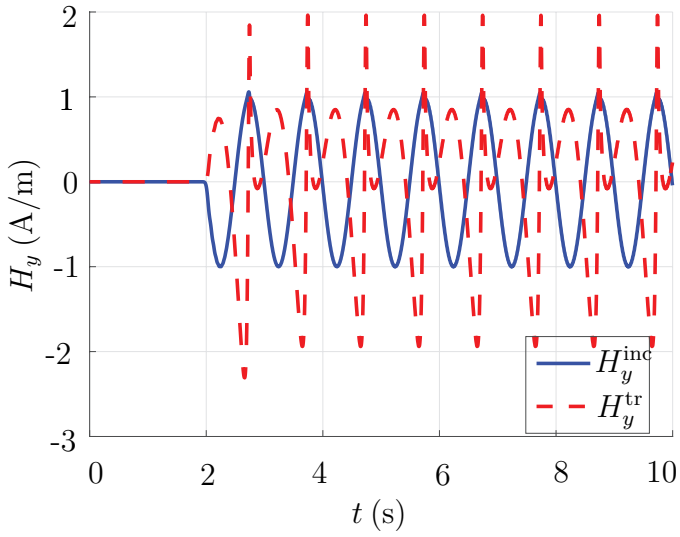

Figure 4.6 Example 2: GSTC-FDTD transmitted (dashed red line) and incident (blue line) waves for the metasurface with sinusoidal time-varying susceptibility, $\chi_{\text{ee}}^{zz} = \chi_{\text{mm}}^{yy} = \chi = 1 + \sin(\omega t)$.

it is expected to automatically be capable of treating the simple discontinuity cases such as graphene, where only the magnetic field is discontinuous. Graphene is positioned at the $E_z\left(i_d+1, j_d\right)$-nodes in the FDTD grid of Fig. 4.4, thus, keeping the continuity of the E-field. Simulation of the graphene sheet has been discussed in [7]. Using the boundary condition on the conducting sheet of the graphene, we obtain

$$H^{\mathrm{tr}}-H^{\mathrm{ir}}=\Delta H=\sigma_{\mathrm{s}} E_y, \tag{4.31}$$

where σ_{s} is the conductivity of the sheet and H^{tr} and H^{ir} are the transmitted and sum of the reflected and incident fields, respectively. Here we consider the second example of the paper, where the conductivity is assumed $\sigma=\frac{\sigma_0}{1+j\omega\tau}$ with σ_0 the dc conductivity and τ the electron relaxation time. Then, discretization of (4.31) in the time-domain yields [idem, Eq.(7)]

$$E_z^n=C^+\left(H_y^{0^+}-H_y^{0^-}\right)^{n+\frac{1}{2}}+C^-\left(H_y^{0^+}-H_y^{0^-}\right)^{n-\frac{1}{2}}, \tag{4.32}$$

with $C^+=\frac{\Delta t+2\tau}{2\Delta t\sigma_0}$ and $C^-=\frac{\Delta t-2\tau}{2\Delta t\sigma_0}$. Replacing $E_z^n\left(0^+, j_d\right)$ with (4.32) in (4.20b) for $i=i_d$, and grouping similar terms, gives

$$\begin{aligned} H_y^{n+\frac{1}{2}}\left(i_d+1, j_d\right) D^+ &= H_y^{n-\frac{1}{2}}\left(i_d+1, j_d\right) D^-+ \\ &\frac{\Delta t}{\mu_0 \Delta x}\left[E_z^n\left(i_d+2, j_d\right)+C^+ H_y^{n+\frac{1}{2}}\left(i_d, j_d\right)+C^- H_y^{n-\frac{1}{2}}\left(i_d, j_d\right)\right], \end{aligned} \tag{4.33}$$

in which $D^+=1+\frac{\Delta t}{\mu_0 \Delta x} C^+$ and $D^-=1-\frac{\Delta t}{\mu_0 \Delta x} C^-$. Next, doing the same procedure for $H_y^{n+\frac{1}{2}}\left(i_d, j_d\right)$ gives

$$\begin{aligned} H_y^{n+\frac{1}{2}}\left(i_d, j_d\right) D^+ &= H_y^{n-\frac{1}{2}}\left(i_d, j_d\right) D^-+ \\ &\frac{\Delta t}{\mu_0 \Delta x}\left[E_z^n\left(i_d, j_d\right)+C^- H_y^{n+\frac{1}{2}}\left(i_d+1, j_d\right)+C^+ H_y^{n-\frac{1}{2}}\left(i_d+1, j_d\right)\right]. \end{aligned} \tag{4.34}$$

As in [7], we choose gaussian-derivative current $I_z(t)=-\sqrt{2e}\beta\left(t-t_0\right)\exp\left(-\beta^2\left(t-t_0^2\right)^2\right)(\mu\mathrm{A})$, with $\beta=10/t_0$, $t_0=1\,\mathrm{ps}$ and e the electron charge, radiating in front of the graphene sheet. Finally, we show the source and measuring points position in Fig. 4.7.

The computational domain is bounded by a PML layer and $\Delta x=\Delta y=\sqrt{2}c_0$, $\Delta t=75\mu m, \sigma_0=29.4e^-3$ and $\tau=0.5\,\mathrm{ps}$, same as in [7]. The FDTD-GSTC simulation results are plotted in Fig. 4.8 and compared with [7]. Both of the methods yield same results in the steady state and transient time.

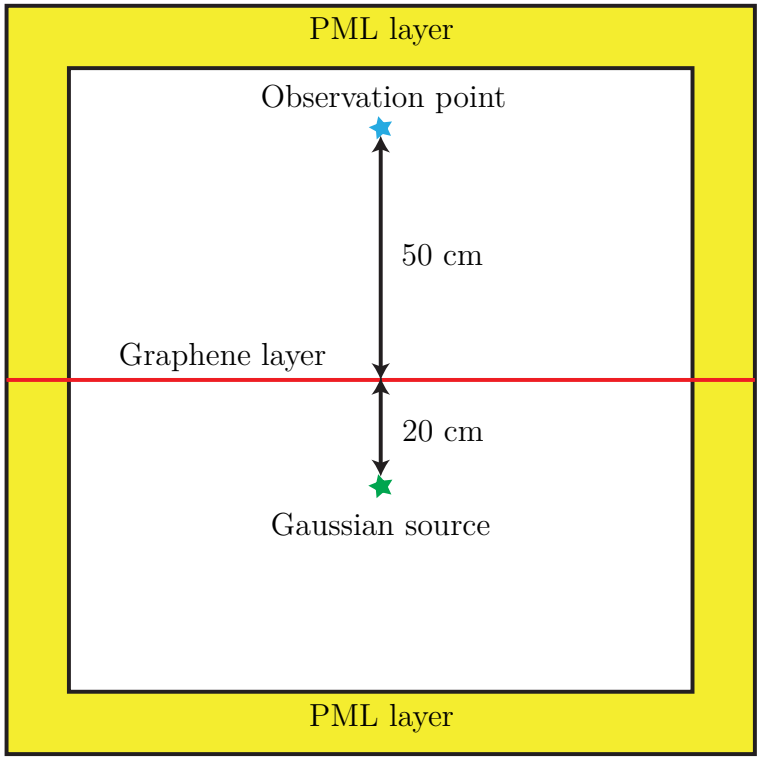

Figure 4.7 Example 3: Position of the source and observation point in the FDTD computation domain with respect to the graphene sheet.

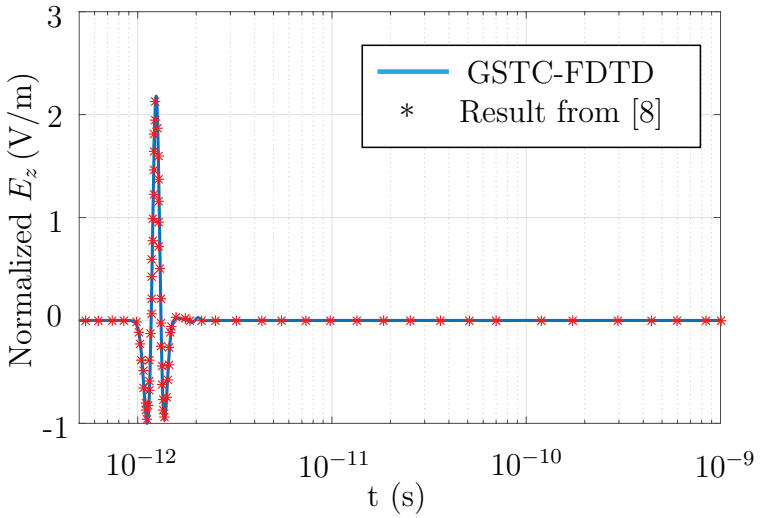

Figure 4.8 Example 3: The steady state and transient time simulation results calculated using GSTC-FDTD and its comparison with [7].

4.5.4 Dispersive Space-Time Varying

In this example, we consider a 2D computational domain and non-reflective metasurface with first order dispersion and varying both in space and time, shown in Fig. 4.9.

The metasurface linearly oscillates in space and time between fully absorbing to half transmitting as depicted in the figure. The susceptibilities for the absorbing and half transmitting metasurfaces can be calculated using GSTC synthesis equations (2.13) or (3.21) as $\tilde{\chi}_{mm}^{yy} = \tilde{\chi}_{ee}^{zz} = \frac{2c_0}{j\omega}$ and $\tilde{\chi}_{mm}^{yy} = \tilde{\chi}_{ee}^{zz} = \frac{2c_0}{3j\omega}$, respectively. We cast these susceptibilities into $\frac{2c_0}{j\omega\alpha(t)}$ form and choose a triangular period in time given by

$$\alpha(t) = \begin{cases} 1 + \frac{1}{50\Delta t}t, & \text{for } 0 \leq t \leq 100\Delta t, \\ 3 - \frac{1}{50\Delta t}(t - 100\Delta t), & \text{for } 100\Delta t \leq 200\Delta t, \end{cases}$$

with $\Delta t = 15.349$ ps. According to this relation, $\alpha(100n_1\Delta t) = \alpha(100n_2\Delta t)$, where n_1 and n_2 can be any integer number. For $\alpha = 1$ the metasurface will absorb all the incident power and for $\alpha = 3$ it will transmit half of the incident power and this behaviours will repeat periodically. Therefore, the corresponding time-varying GSTC in this case is

$$\Delta H_y = \frac{-2c_0\epsilon_0}{\alpha(t)} E_{z,\text{av}}, \tag{4.35a}$$

$$\Delta E_z = \frac{-2c_0\mu_0}{\alpha(t)} H_{y,\text{av}}. \tag{4.35b}$$

Following the procedure mentioed in Sec. 4.3.1 and Sec. 4.4, the update equation for $H_y^{n+\frac{1}{2}}(i_d, j_d)$ is

$$H_y^{n+\frac{1}{2}}(i_d, j_d) F^+ = H_y^{n-\frac{1}{2}}(i_d, j_d) F^- + \frac{\Delta t}{\mu_0 \Delta x}\left[E_z^n(i_d + 1, j_d) - E_z^n(i_d, j_d)\right] - \frac{\Delta t c_0}{2\Delta x \alpha(t)}\left[H_y^{n+\frac{1}{2}}(i_d + 1, j_d) + H_y^{n-\frac{1}{2}}(i_d + 1, j_d)\right], \tag{4.36}$$

with $F^+ = 1 + \frac{\Delta t c_0}{2\Delta x \alpha(t)}$ and $F^- = 1 - \frac{\Delta t c_0}{2\Delta x \alpha(t)}$, and for $E_y^n(i_d + 1, j_d)$ is

$$E_z^n(i_d + 1, j_d) R^+ = E_z^{n-1}(i_d + 1, j_d) R^- - \frac{\Delta t}{\epsilon_0 \Delta x}\left[H_y^{n-\frac{1}{2}}(i_d + 1, j_d) - H_y^{n-\frac{1}{2}}(i_d, j_d)\right] + \frac{\Delta t}{\epsilon_0 \Delta y}\left[H_x^{n-\frac{1}{2}}(i_d + 1, j_d) - H_x^{n-\frac{1}{2}}(i_d + 1, j_d - 1)\right] - \frac{\Delta t c_0}{6\Delta z \alpha(t)}\left[E_y^n(i_d, j_d) + E_y^{n+1}(i_d, j_d)\right], \tag{4.37}$$

with $R^{\pm} = 1 \pm \frac{c_0 \Delta t}{2\Delta x \alpha(t)}$.

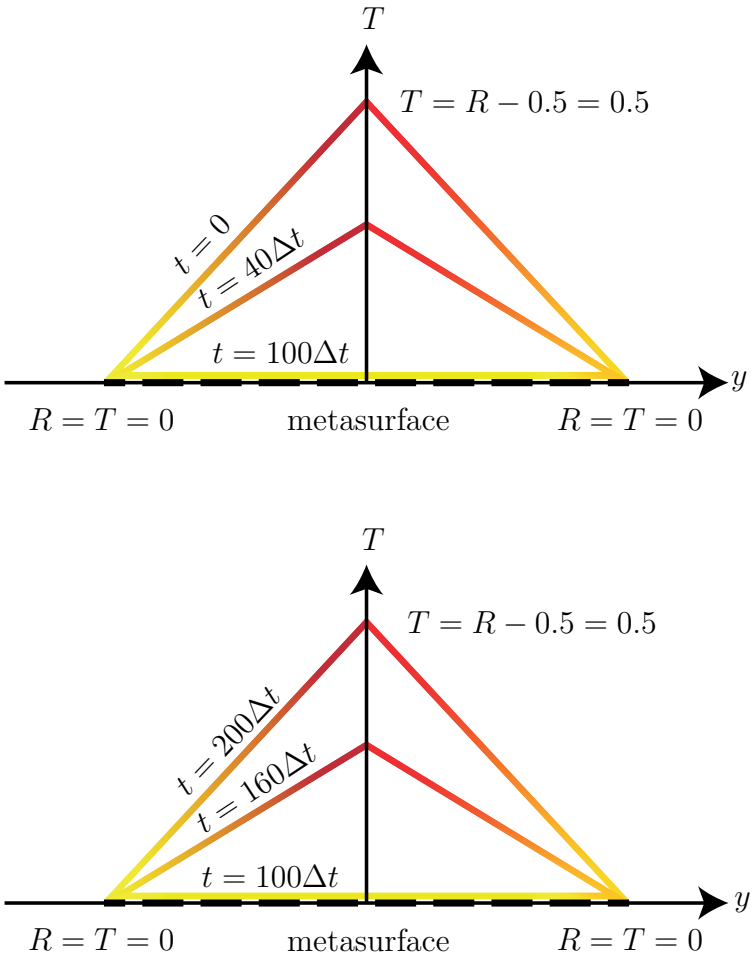

Figure 4.9 Example 4: Metasurface susceptibility linear variation in space and time. The metasurface is always full absorbing at the edges to avoid edge diffraction. Moving toward the center of the metasurface, its behaviour varies periodically and linearly between full absorbing and half transmitting as depicted.

The metasurface is illuminated by a normally incident plane wave and its amplitude is modulated by a Gaussian profile, $E_z(t, y) = \sin(2\pi f t)\exp(-y^2/0.02)$, at the frequency $f = 2\,\text{GHz}$. We have executed the simulation for $30,000$ time-steps, and the results are shown in Fig. 4.10 and 4.11. Figure. 4.10a plots the incident field and the transmitted fields right before and after the metasurface along the y-axis. Due to the Gaussian modulation of the excitation, the field's amplitude is decreasing gradually along the $y-$axis in this figure. This can be seen clearly in Fig. 4.10b, where we are plotting the total $(E_z^{\text{tr}} + E_z^{\text{inc}})$ and the transmitted (E_z^{tr}) fields at the time-step $n = 1823$ in the computation domain. In this figure, the metasurface is illuminated from the top, and the amplitude variation of the transmitted-field is related to the time-variation of the susceptibilities. These figures' results agree well with

the synthesis specifications. The temporal behavior of the incident and transmitted fields at $(x = 0^-, y = 0)$ and $(x = 0^+, y = 0)$, respectively, are plotted in Fig. 4.11. We observe the transmitted field have the same periodicity as the metasurface susceptibility $(200\Delta t)$, and it is a superposition of some harmonics. The generated harmonics are shown in Fig. 4.11b, which is the result of time variation, as expected from Sec. 4.2.

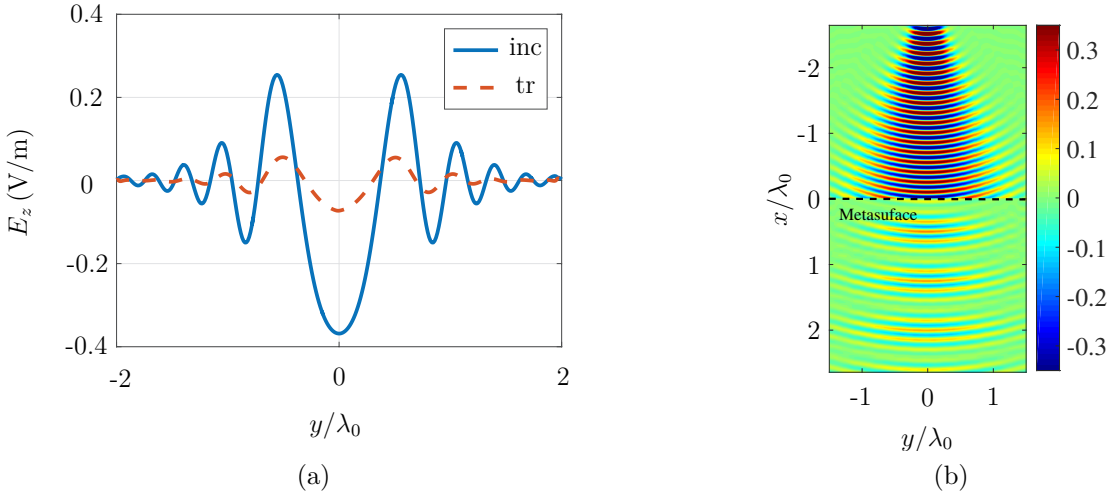

Figure 4.10 Example 4: GSTC-FDTD simulation results for the metasurface of Fig. 4.9. The resolution is set so high ($N_{\text{res}} = 200$) to account for very small space and time variations. (a) Incident (E_z^{inc}) and transmitted waves E_z^{tr} right before ($x = 0^-$) and after ($x = 0^+$) the metasurface, respectively, at time step $n = 1823$. (b) Wave pattern in the 2D computation domain with the metasurface positioned at $x = 0$ (dashed line).

4.5.5 Dispersive Anisotropic Metasurface

As we discussed, the presented technique is applicable for the particular family of dispersive metasurface. To show this, we investigate, reflection and transmission of a reflection-less half-absorbing and half-transmitting *dispersive* metasurface in a 1D FDTD computation domain. From the previous example, the susceptibilities of such metasurface are $\tilde{\chi}_{\text{mm}}^{yy} = \tilde{\chi}_{\text{ee}}^{zz} = j\frac{2c_0}{3\omega}$. We substitute them into (2.13) and obtain

$$\Delta H_y = \frac{-2c_0\epsilon_0}{3} E_{z,\text{av}}, \tag{4.38a}$$

$$\Delta E_z = \frac{-2c_0\mu_0}{3} H_{y,\text{av}}. \tag{4.38b}$$

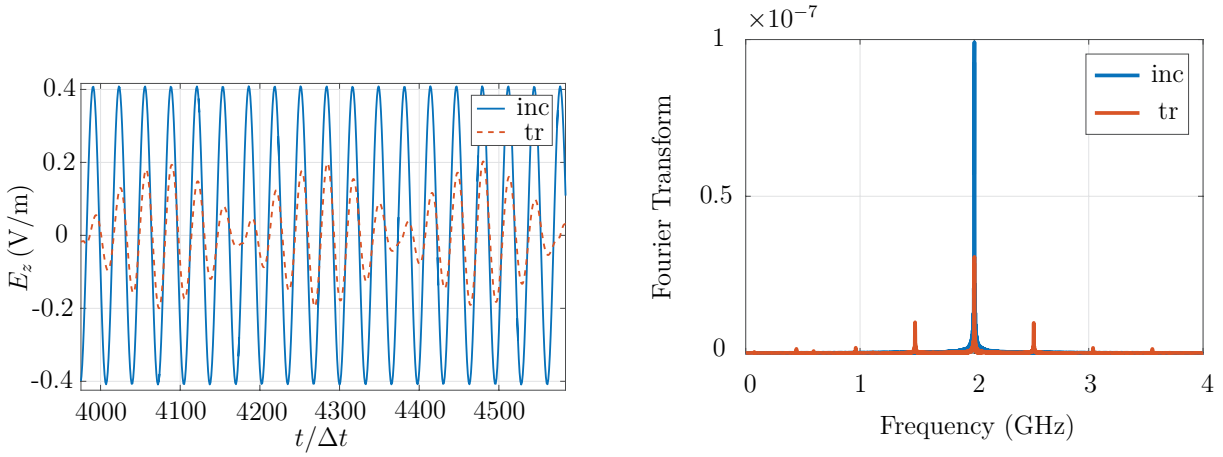

Figure 4.11 Example 4: GSTC-FDTD simulation result for the metasurface of Fig. 4.9. (a) Time variation of the E_z^{inc} and E_z^{tr} right before ($x = 0^-$) and after ($x = 0^+$) the metasurface at $y = 0$, respectively. (b) Fourier transform of the waveforms in (a).

Following again the procedure outlined in Sec. 4.3.1 and Sec. 4.4, the update equation for $H_y^{n+\frac{1}{2}}(i_d)$ is

$$H_y^{n+\frac{1}{2}}(i_d)\left(1+\frac{\Delta t c_0}{6\Delta x}\right) = H_y^{n-\frac{1}{2}}(i_d)\left(1-\frac{\Delta t c_0}{6\Delta x}\right) + \frac{\Delta t}{\mu_0 \Delta x}\left[E_z^n(i_d+1) - E_z^n(i_d)\right] - \frac{\Delta t c_0}{2\Delta x}\left[H_y^{n+\frac{1}{2}}(i_d+1) + H_y^{n-\frac{1}{2}}(i_d+1)\right], \tag{4.39}$$

and for $E_z^{n+1}(i_d+1)$ is

$$E_z^{n+1}(i_d+1)\left(1+\frac{\Delta t c_0}{6\Delta x}\right) = E_z^n(i_d+1)\left(1-\frac{\Delta t c_0}{6\Delta x}\right) + \frac{\Delta t}{\epsilon_0 \Delta x}\left[H_y^{n+\frac{1}{2}}(i_d+1) - H_y^{n+\frac{1}{2}}(i_d)\right] - \frac{\Delta t c_0}{6\Delta x}\left[E_z^n(i_d) + E_z^{n+1}(i_d)\right]. \tag{4.40}$$

FDTD-GSTC simulation results of this example are shown in Fig. 4.12 along with the measured quantity at each of the different region of the computational domain. The amplitude of the transmitted wave is halved and, since the reflected field is zero, the rest of the field is absorbed by the metasurface. That behavior is observed during all the simulation time as shown in 4.12b.

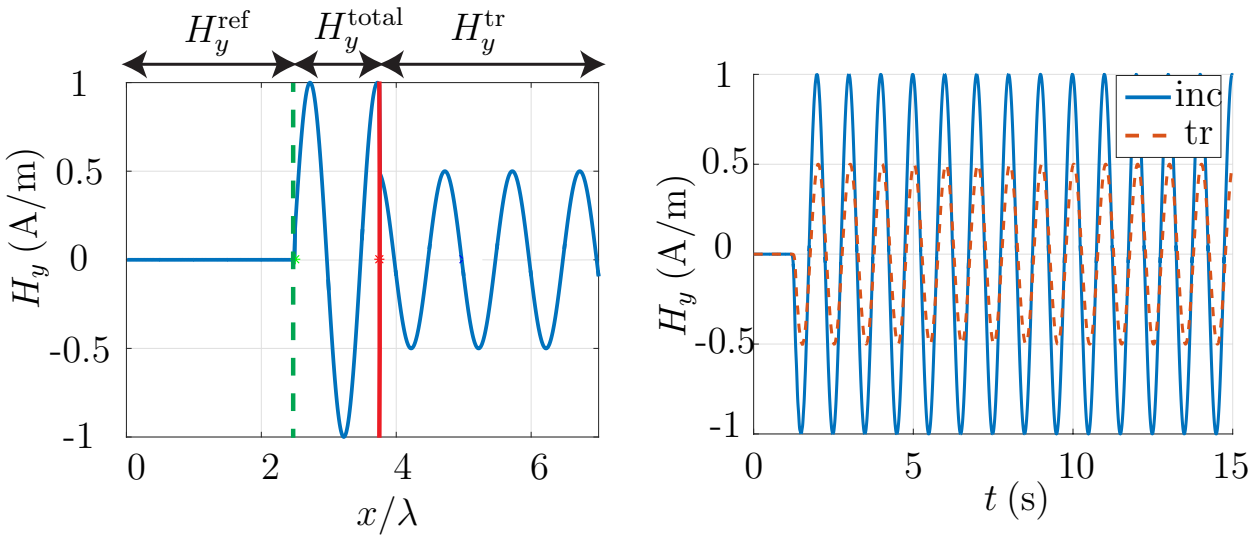

(a) (b)

Figure 4.12 Example 5: GSTC-FDTD simulation results for the none-reflective half-absorbing and half-transmitting dispersive metasurface. (a) Spatial profile of the magnetic field waveform at time $t = 3000\Delta t$ and $H_y^{\text{total}} = H_y^{\text{ref}} + H_y^{\text{inc}}$. (b) Temporal profile of the total field $(H_y^{\text{inc}} + H_y^{\text{ref}})$ right before $(x = 0^-)$ and transmitted wave (H_y^{tr}) right after $(x = 0^+)$ the metasurface. Number of cells per wavelength is $N_{\text{res}} = 30$.

4.6 Extension to the Nonlinear Metasurfaces

The GSTC-FDTD technique also applies to the nonlinear metasurfaces, where the susceptibility function depends on orders of the electric or magnetic fields larger than one and where the susceptibility tensors reach to the order of the associated nonlinearity. Here, we investigate the case of non-zero second-order nonlinear electric and magnetic susceptibilities. We will restrict our attention to the anisotropic susceptibilities, $\overline{\overline{\chi}}_{\text{em}} = \overline{\overline{\chi}}_{\text{me}} = 0$. The frequency domain electric and magnetic polarization densities are

$$\tilde{\boldsymbol{P}} = \epsilon_0 \overline{\overline{\tilde{\chi}}}_{\text{ee}}^{(1)} \cdot \tilde{\boldsymbol{E}}_{\text{av}} + \varepsilon_0 \overline{\overline{\tilde{\chi}}}_{\text{ee}}^{(2)} \cdot \tilde{\boldsymbol{E}}_{\text{av}}^2, \tag{4.41a}$$

$$\tilde{\boldsymbol{M}} = \overline{\overline{\tilde{\chi}}}_{\text{mm}}^{(1)} \cdot \tilde{\boldsymbol{H}}_{\text{av}} + \overline{\overline{\tilde{\chi}}}_{\text{mm}}^{(2)} \cdot \tilde{\boldsymbol{H}}_{\text{av}}^2, \tag{4.41b}$$

with $\overline{\overline{\tilde{\chi}}}^{(1)}$ and $\overline{\overline{\tilde{\chi}}}^{(2)}$ representing the first-order linear and second-order nonlinear susceptibilities, respectively.

From the practical considerations and proof of concept, we consider only the diagonal terms of the $\overline{\overline{\chi}}_{\text{mm}}$ and $\overline{\overline{\chi}}_{\text{ee}}$ susceptibility tensors. Without loss of the generality, we illuminate the metasurface by a $z-$polarized field; however, our discussion will be applicable to any field

polarization. Under these simplifications, upon substitution of (4.41) into (2.9), the nonlinear counterpart of (2.13) will be

$$-\Delta H_y = \varepsilon_0 j\omega \tilde{\chi}_{\mathrm{ee}}^{zz,(1)} E_{z,\mathrm{av}} + \varepsilon_0 j\omega \tilde{\chi}_{\mathrm{ee}}^{zz,(2)} E_{z,\mathrm{av}}^2, \tag{4.42a}$$

$$-\Delta E_z = \mu_0 j\omega \tilde{\chi}_{\mathrm{mm}}^{yy,(1)} H_{y,\mathrm{av}} + \mu_0 j\omega \tilde{\chi}_{\mathrm{mm}}^{yy,(2)} H_{y,\mathrm{av}}^2. \tag{4.42b}$$

In practice, a nonlinear metasurface is often designed to generate harmonics of the incident wave. This allows us to relax the dispersion condition on the susceptibilities and to obtain the associated time-domain relation for (4.42) as

$$-\Delta H_z = \varepsilon_0 \chi_{\mathrm{ee}}^{yy,(1)} \frac{\partial E_{y,\mathrm{av}}}{\partial t} + \varepsilon_0 j\omega \chi_{\mathrm{ee}}^{yy,(2)} \frac{\partial E_{y,\mathrm{av}}^2}{\partial t}, \tag{4.43a}$$

$$-\Delta E_y = \mu_0 j\omega \chi_{\mathrm{mm}}^{zz,(1)} \frac{\partial H_{z,\mathrm{av}}}{\partial t} + \mu_0 j\omega \chi_{\mathrm{mm}}^{zz,(2)} \frac{\partial H_{z,\mathrm{av}}^2}{\partial t}. \tag{4.43b}$$

This relation is used for the nonlinear metasurface synthesis. Since (4.42) consists of two sets of equations and four unknowns; thus, two sets of transformations are needed for the synthesis. Assuming $(\boldsymbol{H}, \boldsymbol{E})_1$ and $(\boldsymbol{H}, \boldsymbol{E})_2$ are the two specified set of fields, the susceptibilities are [101]

$$\chi_{\mathrm{ee}}^{zz,(1)} = -\frac{\Delta H_{y2} \frac{\partial E_{z,\mathrm{av1}}^2}{\partial t} - \Delta H_{y1} \frac{\partial E_{z,\mathrm{av2}}^2}{\partial t}}{\varepsilon_0 \left[\frac{\partial E_{z,\mathrm{av1}}^2}{\partial t} \frac{\partial E_{z,\mathrm{av2}}}{\partial t} - \frac{\partial E_{z,\mathrm{av1}}}{\partial t} \frac{\partial E_{z,\mathrm{av2}}^2}{\partial t} \right]}, \tag{4.44a}$$

$$\chi_{\mathrm{ee}}^{zz,(2)} = \frac{\Delta H_{y2} \frac{\partial E_{z,\mathrm{av1}}}{\partial t} - \Delta H_{y1} \frac{\partial E_{z,\mathrm{av2}}}{\partial t}}{\varepsilon_0 \left[\frac{\partial E_{z,\mathrm{av1}}^2}{\partial t} \frac{\partial E_{z,\mathrm{av2}}}{\partial t} - \frac{\partial E_{z,\mathrm{av1}}}{\partial t} \frac{\partial E_{z,\mathrm{av2}}^2}{\partial t} \right]}, \tag{4.44b}$$

$$\chi_{\mathrm{mm}}^{yy,(1)} = -\frac{\Delta E_{z2} \frac{\partial H_{y,\mathrm{av1}}^2}{\partial t} - \Delta E_{z1} \frac{\partial H_{y,\mathrm{av2}}^2}{\partial t}}{\mu_0 \left[\frac{\partial H_{y,\mathrm{av1}}^2}{\partial t} \frac{\partial H_{y,\mathrm{av2}}}{\partial t} - \frac{\partial H_{y,\mathrm{av1}}}{\partial t} \frac{\partial H_{y,\mathrm{av2}}^2}{\partial t} \right]}, \tag{4.44c}$$

$$\chi_{\mathrm{mm}}^{yy,(2)} = \frac{\Delta E_{z2} \frac{\partial H_{y,\mathrm{av1}}}{\partial t} - \Delta E_{z1} \frac{\partial H_{y,\mathrm{av2}}}{\partial t}}{\mu_0 \left[\frac{\partial H_{y,\mathrm{av1}}^2}{\partial t} \frac{\partial H_{y,\mathrm{av2}}}{\partial t} - \frac{\partial H_{y,\mathrm{av1}}}{\partial t} \frac{\partial H_{y,\mathrm{av2}}^2}{\partial t} \right]}. \tag{4.44d}$$

The condition of no reflection depends on the direction of the incident field [101]. Assuming Fig. 4.13a, where the incident field propagates in $+x-$direction, and solving (4.44) for $E^{\mathrm{ref}} =$

$H^{\text{ref}} = 0$ gives the condition

$$\chi_{\text{ee}}^{zz,1} = \chi_{\text{mm}}^{yy,1}, \tag{4.45}$$

$$\eta_0 \chi_{\text{ee}}^{zz,2} = \chi_{\text{mm}}^{yy,2}. \tag{4.46}$$

While the condition for Fig. 4.13b when the metasurface is excited from the opposite direction is

$$\chi_{\text{ee}}^{zz,1} = \chi_{\text{mm}}^{yy,1}, \tag{4.47}$$

$$-\eta_0 \chi_{\text{ee}}^{zz,2} = \chi_{\text{mm}}^{yy,2}. \tag{4.48}$$

Therefore, a nonlinear metasurface is nonreciprocal. This is due to different relation between E and H in the two cases ($E_z = \pm\eta_0 H_y$) and appearance of ψ_{av}^2 with $\psi = E$ or H for $\chi^{(1)}$ while ψ_{av} for $\chi^{(2)}$ in the denominator of (4.44).

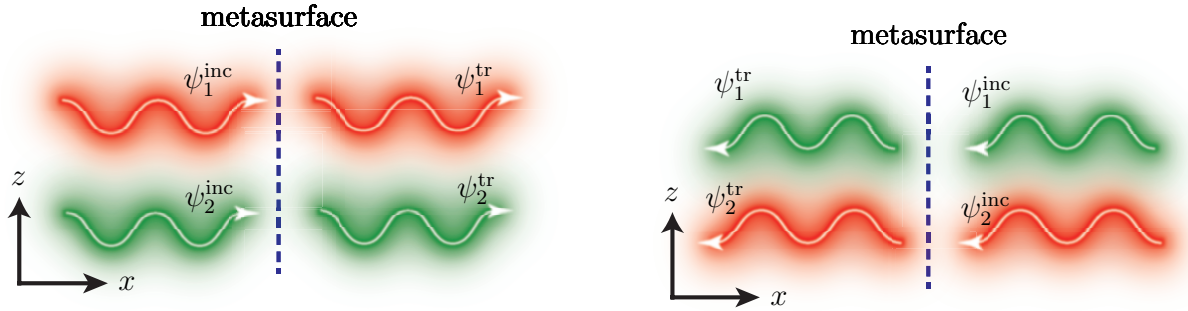

Figure 4.13 Nonlinear metasurface synthesis. (a) Direct transformation excited from the left. (b) Reciprocal transformation of (a) excited from the right.

We now consider a GSTC-FDTD analysis example where the metasurface is lossless, have small second-order non-linearity, as in all practical metasurfaces, and immersed in free space. The small second-order non-linearity enables perturbation analysis [101], too, which will be used for the GSTC-FDTD results validation. An incident plane-wave is assumed, $E^{\text{inc}} = E_0 \cos \omega t$, as in [101]. Discretization of (4.43) and following a similar procedure mentioned in the previous section gives the two solutions for the field update equations around the discontinuity. The acceptable physical solution is

$$H_y^{n+\frac{1}{2}}(i_d) = \frac{2\Delta x - \chi_{\text{ee}}^{zz,(1)} - H_y^{n+\frac{1}{2}}(i_d+1)\chi_{\text{ee}}^{zz,(2)} - \sqrt{\Delta_h}}{\chi_{\text{ee}}^{zz,(1)}}, \tag{4.49a}$$

$$E_z^n(i_d+1) = \frac{2\Delta x - \chi_{\mathrm{mm}}^{yy,(1)} - E_x^n(i_d)\chi_{\mathrm{mm}}^{yy,(2)} - \sqrt{\Delta_e}}{\chi_{\mathrm{mm}}^{yy,(1)}}, \tag{4.49b}$$

with

$$\begin{aligned}\frac{\Delta_h}{\sqrt{\mu_0}} &= 4\Delta t\chi_{\mathrm{ee}}^{zz,(2)}\left[E_z^n(i_d) - E_z^n(i_d+1)\right] \\ &+ 4\mu_0\Delta x^2 + \mu_0\left[\chi_{\mathrm{ee}}^{zz,(1)} + \left(H_y^{n-\frac{1}{2}}(i_d) + H_y^{n+\frac{1}{2}}(i_d+1)\right)\chi_{\mathrm{ee}}^{zz,(2)}\right]^2 \\ &- 4\mu_0\Delta x\left[\chi_{\mathrm{ee}}^{zz,(1)} + \left(H_y^{n-\frac{1}{2}}(i_d) + H_y^{n+\frac{1}{2}}(i_d+1)\right)\chi_{\mathrm{ee}}^{zz,(2)}\right],\end{aligned}$$

and

$$\begin{aligned}\frac{\Delta_e}{\sqrt{\varepsilon_0}} &= 4\Delta t\chi_{\mathrm{mm}}^{yy,(2)}\left[H_y^{n+\frac{1}{2}}(i_d) - H_y^{(}i_d+1)\right] \\ &+ 4\varepsilon_0\Delta x^2 + \varepsilon_0\left[\chi_{\mathrm{mm}}^{yy,(1)} + \left(E_z^{n-1}(i_d) + E_z^n(i_d+1)\right)\chi_{\mathrm{mm}}^{yy,(2)}\right]^2 \\ &- 4\varepsilon_0\Delta x\left[\chi_{\mathrm{mm}}^{yy,(1)} + \left(E_z^{n+1}(i_d) + E_x^n(i_d+1)\right)\chi_{\mathrm{mm}}^{yy,(2)}\right].\end{aligned}$$

Equation (4.49) implies $\Delta_e > 0$ and $\Delta_h > 0$. A consequence of this restriction is the limited choice of the susceptibilities and amplitude of the excitation signal to avoid nonphysical behaviors.

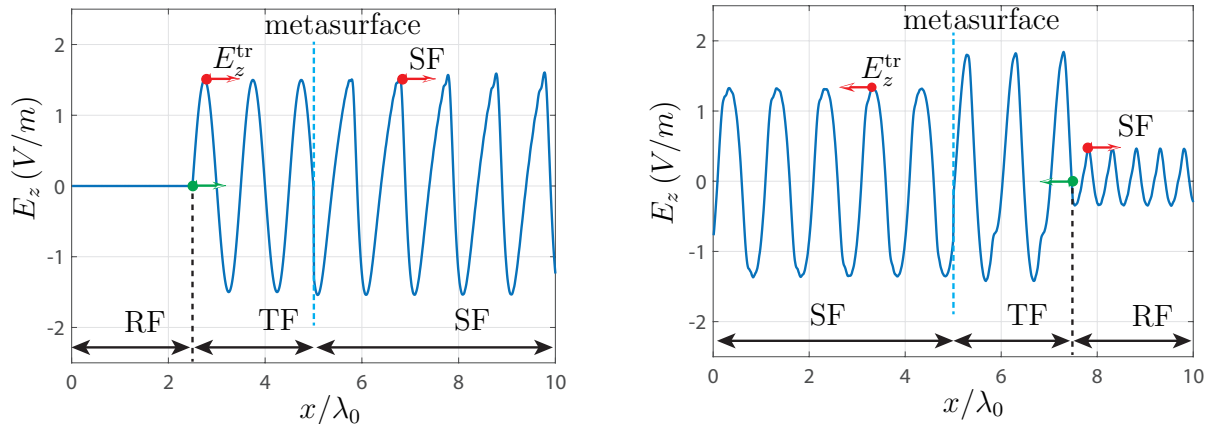

Figure 4.14 Nonlinear metasurface simulation. The RF, TF and SF indicates reflected, transmitted and scattered field region, respectively. (a) Excitation from the left and the transmitted field located at the right of the metasurface in the SF region. (b) Excitation from the right and the transmitted field located at the left of the metasurface in the SF region.

We consider the following arbitrary parameters: $E_0 = 1.5$ V/m, $\chi_{\rm ee}^{zz,(1)} = \chi_{\rm mm}^{yy,(1)} = 0.1$ m and $\chi_{\rm ee}^{zz,(2)} = \chi_{\rm mm}^{yy,(2)} = 0.04$ m$^2/V$. The simulation results are shown in Fig. 4.14, where the metasurface is excited on both sides by the source positioned at the TF-RF (total-field reflected-field) interface. Figures 4.14a and 4.14b show the illumination in $+x$ and $-x$ directions, respectively. In both of these cases, the distortion of the transmitted field indicates generation of the new harmonics. Whereas, different reflections are achieved in the two cases due to the nonreciprocal behavior, which is the consequence of nonlinearity. This agrees with the aforementioned reflection-less and non-reciprocity condition for the nonlinear metasurfaces.

For validation of the harmonics generation, we perform a parametric analysis for $E_0 = 1.5$ V/m, $\chi_{\rm ee}^{zz,(1)} = \chi_{\rm mm}^{yy,(1)} = 0.1$ m, as before, and $E_0 = 10$ V/m, $\chi_{\rm ee}^{zz,(1)} = \chi_{\rm mm}^{yy,(1)} = 0.3$ m; and $\chi_{\rm ee}^{zz,(2)} = \chi_{\rm mm}^{yy,(2)}$ is swiped. The generated harmonic corresponding to the example of Fig. 4.14 is marked by a star in Fig. 4.15a. These analysis confirm our GSTC-FDTD method.

4.7 Conclusion

In this chapter, we developed a simulation technique for the polychromatic, nonlinear and space-time varying metasurfaces by integrating GSTCs with the FDTD. This technique is based on the virtual node concept, where electric and magnetic field nodes are introduced in updating the fields around the discontinuity. Similar to the FDFD-GSTC technique, the metasurface was handled as a virtual structure in the Yee grid. The physical interpretation and their reduction to the conventional FDTD equations were discussed. The developed FDTD-GSTC technique is fully numeric, easy to develop and accurately simulates general sheet discontinuity. We proved the accuracy and applicability of the proposed method through many illustrative examples.

However, regarding temporal non-locality, it is useful solely for the $\frac{1}{(j\omega)^n}$ dispersion form and is unable to treat the general metasurface dispersion, which limits the applicability of the method. In the following chapter, we will tackle this problem through an efficient auxiliary differential equation.

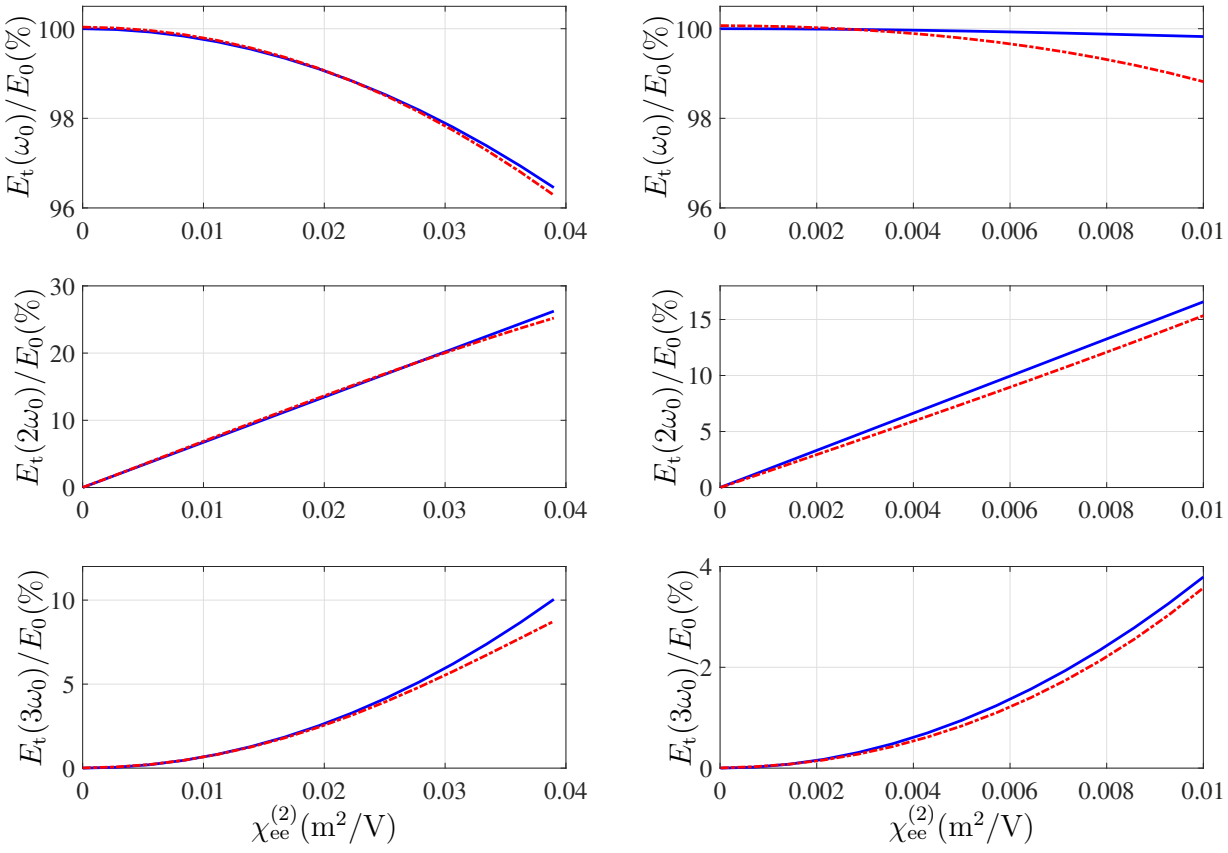

Figure 4.15 Parametric study of the non-linear metasurface using FDTD-GSTC. (a) $E_0 = 1.5$ V/m, $\chi_{ee}^{zz,(1)} = \chi_{mm}^{yy,(1)} = 0.1$ m, and (b) $E_0 = 10$ V/m, $\chi_{ee}^{zz,(1)} = \chi_{mm}^{yy,(1)} = 0.3$ m.

CHAPTER 5 DISPERSIVE BIANISOTROPIC METASURFACE SIMULATION

The presented FDTD-GSTC in the previous chapter simulates a general discontinuity but is unable to take into account the frequency dispersion. In this chapter, we are addressing this issue by replacing the conventional FDTD equations by enhanced update equations. This scheme consists of the virtual node and virtual structure concept mentioned in the previous chapter combined by judiciously selected auxiliary functions based on GSTCs that carries the effect of the discontinuity. Our technique is based on the efficient ADE that is 1- exact (no discretization approximation), 2- memory and speed vise efficient, 3- applicable to bianisotropic susceptibilities, $\overline{\overline{\chi}}(\omega;t)$. Unlike the conventional ADE applied for the bulk materials, it consists of tensorial electric and magnetic polarizations due to bianisotropy. It is therefore more general but involves a complicated system of equations. The developments will be verified by some examples, and the results will be compared with the specifications or an approximate technique.

We will describe the basic physics of material's dispersion and discuss their Lorentz, Drude and Debye dispersive models. Then, we will establish the ADE-dispersive FDTD metasurface analysis. Three illustrative examples validate this proposed formulation. Finally, we draw our conclusion.

5.1 Dispersive Medium Modeling

A medium can have spatial [161,164], $\boldsymbol{k}$, or temporal dispersion [165], ω, or a combination of them. Figure 5.1 shows a dispersive material's response to an excitation. Figure 5.1a depicts spatial dispersion or spatial non-locality. Unlike local materials, their dispersion relation represents propagation in various directions for a specified excitation frequency f_0. Temporal dispersion, Fig. 5.1b, is dual of the spatial dispersion, i.e., their dispersion relation represents propagation in multiple frequencies for a specified excitation direction $\boldsymbol{k}$. Dispersion, both the spatial and temporal as in Fig. 5.1c, is a consequence of causality, which states that any effect must be preceded by a cause [166], embodied in the Kramers-Kronig relations [165]. In our discussions during this chapter, we will consider only temporal dispersion (non-locality) and, for the brevity, we will directly call it dispersion unless otherwise specified. The primary mechanisms leading to dispersion are electronic, atomic, molecular or domain polarizations. They are formulated and expressed by the macroscopic electric and magnetic polarization density vectors [102].

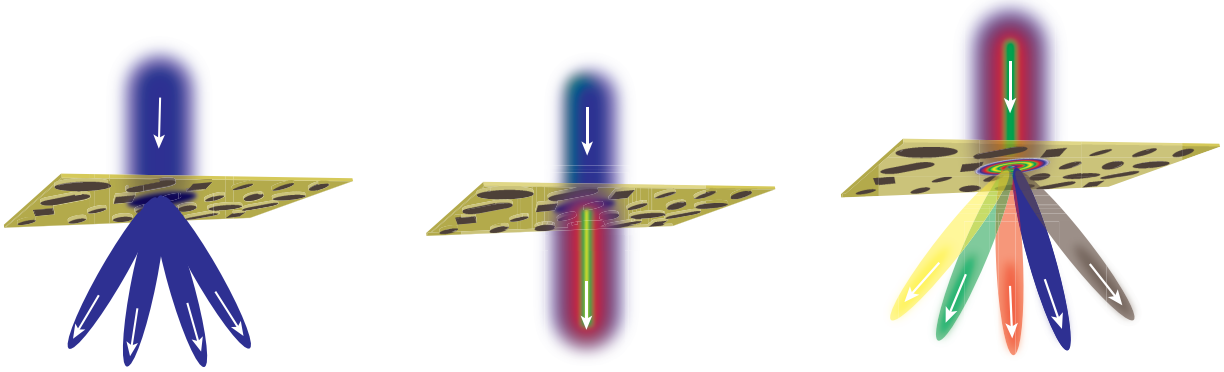

(a) (b) (c)

Figure 5.1 Schematic representation of the spatial and temporal dispersion (non-locality). The structure is illuminated from the top. (a) Spatial dispersion, where a monochromatic incident wave dispersed in the transmitted-field region. (b) Temporal dispersion, where a monochromatic incident wave transformed into a polychromatic signal in the transmitted-field region. and (c) Spatio-temporal dispersion, where polychromatic signal dispersed in different direction (spatial non-locality) at different frequencies (temporal non-locality).

Newton equation of motion treats the overall microscopic electronic, atomic and molecular effects by associating them with a damped harmonic oscillator in a homogenous medium [43, 102,165,167]. We show this concept for an electron with mass m bounded elastically to heavy nuclei. Newton equations of motion gives [102]

$$m\frac{d^2\boldsymbol{r}}{dt^2} = -m\omega_0^2\boldsymbol{r} - m\upsilon\frac{d\boldsymbol{r}}{dt} + \boldsymbol{F}, \tag{5.1}$$

where $\boldsymbol{r}$ is the displacement vector, υ is the collision frequency and the terms at the right side represent the elastic restoring force of the nuclei, damping force and Lorentz force acting on the electron, respectively. The Lorentz force $\boldsymbol{F}$ is given by

$$\boldsymbol{F} = e\left(\boldsymbol{E}^{\text{act}} + \boldsymbol{V}\times\boldsymbol{B}^{\text{act}}\right), \tag{5.2}$$

with e the electron charge and $\boldsymbol{V}$ the electron velocity. It is a valid assumption to consider $|\boldsymbol{V}| \ll c_0$. This leads to negligible magnetic force and $\boldsymbol{F} = e\boldsymbol{E}^{\text{act}}$. The acting electric $\boldsymbol{E}^{\text{act}}$ field in(5.2) is sum of the vacuum field, E, and polarization field, E_{P}. Ignoring the magnetic field, the electric field is

$$\boldsymbol{E}^{\text{act}} = \boldsymbol{E} + \frac{Ne\boldsymbol{r}}{3\varepsilon_0}, \tag{5.3}$$

where $\boldsymbol{E}_{\text{P}} = \frac{\boldsymbol{P}}{3\varepsilon_0} = \frac{Ne\boldsymbol{r}}{3\varepsilon_0}$ is calculated by Clausius–Mossotti formula [168]. Next, using (5.3) in

the approximate Lorentz force and transforming (5.1) into the frequency domain assuming $\exp j\omega t$ time-harmonic field yields

$$-m\omega^2\boldsymbol{r} = -m\omega_0^2\boldsymbol{r} - j\omega m\upsilon\boldsymbol{r} + e\left(\boldsymbol{E} + \frac{Ne\boldsymbol{r}}{3\varepsilon_0}\right). \tag{5.4}$$

Solving this relation for $\boldsymbol{E}$ and using $\boldsymbol{D} = \varepsilon_0\varepsilon_{\mathrm{L,r}}\boldsymbol{E} = \varepsilon_0\boldsymbol{E} + \boldsymbol{P}$ leads to the frequency domain macroscopic susceptibility model for dispersion represented by the Lorentz term as

$$\varepsilon_{\mathrm{L,r}} - 1 = \tilde{\chi}_{\mathrm{L}}(\omega) = \frac{\omega_{\mathrm{p}}^2}{\omega_0^2 + 2j\omega\gamma - \omega^2}, \tag{5.5}$$

where $\omega_{\mathrm{p}} = \frac{Ne^2}{m\varepsilon_0}$ and $\gamma = \upsilon/2$. Figure 5.2a plots the real and imaginary parts of $\tilde{\chi}_{\mathrm{L}}(\omega)$ versus frequency.

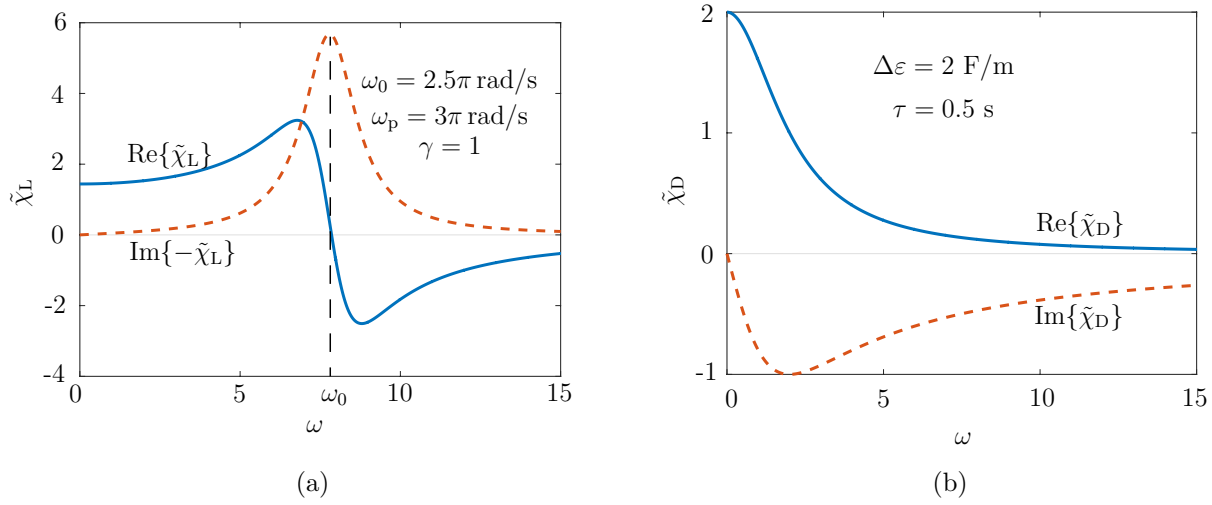

Figure 5.2 Susceptibility model of temporal dispersion. (a) Lorentz model. (b) Debye model.

The conducting electrons in the metals are not bounded by the nuclei force. Therefore, they do not support resonance (ω_0) and hence the Lorentz model of (5.5) reduces to the Drude dispersion model, $\tilde{\chi}_{\mathrm{L}}(\omega) = \omega_{\mathrm{p}}^2/(2j\omega\gamma - \omega^2)$. In some other materials, for example, biological tissues, the loss is significant at low frequencies such that $\omega^2 \ll \omega\gamma$. In this case (5.5) reduces to the Debye dispersion model

$$\tilde{\chi}_{\mathrm{D}}(\omega) = \frac{\Delta\chi}{1 + j\omega\tau} = \chi_\infty + \frac{\chi_{\mathrm{s}} - \chi_\infty}{1 + j\omega\tau} \tag{5.6}$$

where $\Delta\chi = (\omega_{\mathrm{p}}/\omega_0)^2$, χ_{s} and χ_∞ are the static and infinite frequency susceptibilities, respectively, and $\tau = 2\gamma/\omega_0$. Figure 5.2b plots the real and imaginary parts of $\tilde{\chi}_{\mathrm{D}}(\omega)$.

In general, a material is represented by many Lorentz terms. Thus, the relation between the polarization vector and the electric field is

$$\tilde{P}_i = \varepsilon_0 \sum_j \tilde{\chi}_{ij} \tilde{E}_j(\boldsymbol{r}, \omega) = \varepsilon_0 \sum_j \frac{\omega_{ij,\mathrm{p}}^2}{\omega_0^2 + 2j\omega\gamma_{ij} - \omega^2} \tilde{E}_j(\boldsymbol{r}, \omega), \tag{5.7}$$

with i and j representing any of (x, y, z) space components. A metasurface is composed of dielectrics, metals or combinations of them. This results in resonant behavior and exhibiting Lorentz or Debye dispersions similar to (5.7).

5.2 Dispersive Metasurface Analysis

Equation (2.13) is used for the metasurface synthesis. We assume that the susceptibilities follow the Lorentz or Debye dispersion models in the bandwidth of interest. Other susceptibility functions may be handled by their expansion in terms of Lorentzian and/or Debye dispersion functions [169, 170]. Since solutions of (2.13) are necessarily causal, the susceptibilities are necessarily dispersive.

Without loss of generality, we consider a 1D-FDTD computation domain and bianisotropic susceptibility tensor to avoid lengthy equations and tedious developments. The 1D-FDTD assumption naturally restricts the nonzero fields components to $(E_z, H_y) \neq 0$ and propagation in the $x-$direction, $\tilde{\mathbf{k}} = k_0 \hat{x}$. The extension to the 2D and 3D problems will not be shown here as it straightforwardly involves a similar procedure, with just more complexity and long equations. We assume the general Lorentz dispersion

$$\tilde{\chi}_{\mathrm{ab}}(\omega) = \frac{\omega_{\mathrm{p,ab}}^2}{\omega_{0,\mathrm{ab}}^2 + 2j\omega\gamma_{\mathrm{ab}} - \zeta\omega^2}, \tag{5.8}$$

where {a or b} = e, m. The dimensionless coefficient ζ is involved to switch between the Debye dispersion ($\zeta = 0$) and the Lorentz dispersion ($\zeta = 1$).

5.2.1 FDTD Virtual Node

The FDTD equations mentioned in Chapter (4), Equ. (4.11), are implemented in this chapter. We follow the virtual node concept and the metasurface positioning described in Sec. 4.3. Therefore, with reference to Fig. 4.3, the update equation around the discontinuity is calculated as

$$E_z^n\left(i_d+1\right)=E_z^{n-1}\left(i_d+1\right)+\frac{\Delta t}{\varepsilon_0\Delta x}\left[H_y^{n-\frac{1}{2}}\left(i_d+1\right)-H_y^{n-\frac{1}{2}}\left(0^+\right)\right], \tag{5.9}$$

and

$$H_y^{n+\frac{1}{2}}\left(i_d\right)=H_y^{n-\frac{1}{2}}\left(i_d\right)+\frac{\Delta t}{\mu_0\Delta x}\left[E_z^n\left(0^-\right)-E_z^n\left(i_d\right)\right]. \tag{5.10}$$

Next, $H_y(0^+)$ and $E_z(0^-)$ are computed using the GSTC (2.13), which reduces here to

$$\Delta\tilde{H}_y=j\omega\varepsilon_0\tilde{\chi}_{\rm ee}^{zz}\tilde{E}_{z,\rm av}+jk_0\tilde{\chi}_{\rm em}^{zy}\tilde{H}_{y,\rm av}, \tag{5.11a}$$

$$\Delta\tilde{E}_z=j\omega\mu_0\tilde{\chi}_{\rm mm}^{yy}\tilde{H}_{y,\rm av}+jk_0\tilde{\chi}_{\rm me}^{yz}\tilde{E}_{z,\rm av}, \tag{5.11b}$$

where the χ's are given in (5.8).

Equation. (5.11) must be transformed into time-domain to be compatible with the FDTD simulation as the overall FDTD is implemented in the time domain. This transformation generally requires convolution integrals similar to (2.50). However, substitution of the general Lorentz susceptibilities in (5.11) will involve only $(j\omega)^n$, where n is an integer. The usefulness of this property is to replace the $j\omega$ with $\frac{d}{dt}$ and calculate its corresponding time-domain counterpart.

5.2.2 Auxiliary Functions

following the discussions in Sec. 4.4, there is a mismatch between the space and time samplings in the discretized version of the time-domain equation (5.11). The classical efficient solution developed for the bulk and non-bianisotropic dispersive media is to introduce Auxiliary Differential Equations (ADEs) [152]. Here we are extending this technique to the bianisotropic metasurfaces. Choice of the auxiliary functions are not trivial. They have to satisfy two essential FDTD-ADE requirements: 1- numerical stable FDTD-GSTC update equations, and 2- discretizable equations both in space and time. For example, the following auxiliary functions used in the classical efficient ADE [152] is not stable and discretizable.

$$\begin{aligned}\tilde{P}_{\rm ee}^{zz}&=\varepsilon_0\tilde{\chi}_{\rm ee}^{zz}\tilde{E}_{z,\rm av},\\ \tilde{P}_{\rm em}^{zy}&=\frac{\tilde{\chi}_{\rm em}^{zy}}{c_0}\tilde{H}_{y,\rm av},\\ \tilde{M}_{\rm mm}^{yy}&=\mu_0\tilde{\chi}_{\rm mm}^{yy}\tilde{H}_{y,\rm av},\\ \tilde{M}_{\rm me}^{yz}&=\frac{\tilde{\chi}_{\rm me}^{yz}}{c_0}\tilde{E}_{z,\rm av}.\end{aligned}$$

Therefore, inspired from (5.12), we use the modified four set of auxiliary functions reading

as

$$\tilde{P}_{\text{ee}}^{zz} = j\omega\varepsilon_0\tilde{\chi}_{\text{ee}}^{zz}\tilde{E}_{z,\text{av}}, \tag{5.13a}$$

$$\tilde{P}_{\text{em}}^{zy} = jk_0\tilde{\chi}_{\text{em}}^{zy}\tilde{H}_{y,\text{av}}, \tag{5.13b}$$

$$\tilde{M}_{\text{mm}}^{yy} = j\omega\mu_0\tilde{\chi}_{\text{mm}}^{yy}\tilde{H}_{y,\text{av}}, \tag{5.13c}$$

$$\tilde{M}_{\text{me}}^{yz} = jk_0\tilde{\chi}_{\text{me}}^{yz}\tilde{E}_{z,\text{av}}. \tag{5.13d}$$

We now verify the validity of the auxiliary functions (5.13). their substitution into (5.11) interestingly gives the coefficient-free relations

$$\Delta\tilde{H}_y = \tilde{P}_{\text{ee}}^{zz} + \tilde{P}_{\text{em}}^{zy}, \tag{5.14a}$$

$$\Delta\tilde{E}_z = \tilde{M}_{\text{mm}}^{yy} + \tilde{M}_{\text{me}}^{yz}. \tag{5.14b}$$

We discretize the inverse Fourier transform of (5.14a) to get the time-domain quantities $H_y^{n-\frac{1}{2}}(0^+)$ and $E_z^n(0^+)$

$$H_y^{n-\frac{1}{2}}\left(0^+\right) = H_y^{n-\frac{1}{2}}(i_d) + \frac{P_{\text{ee}}^{zz,n} + P_{\text{ee}}^{zz,n-1}}{2} + \frac{P_{\text{em}}^{zy,n} + P_{\text{em}}^{zy,n-1}}{2}, \tag{5.15a}$$

$$E_z^n\left(0^-\right) = E_z^n\left(i_d+1\right) - \frac{M_{\text{mm}}^{yy,n+\frac{1}{2}} + M_{\text{mm}}^{yy,n-\frac{1}{2}}}{2} - \frac{M_{\text{me}}^{yz,n+\frac{1}{2}} + M_{\text{me}}^{yz,n-\frac{1}{2}}}{2}, \tag{5.15b}$$

Substitution of into (5.9) yields

$$\begin{aligned} E_z^n\left(i_d+1\right) = E_z^{n-1}\left(i_d+1\right) + \frac{\Delta t}{\varepsilon_0\Delta x}\left[H_y^{n-\frac{1}{2}}\left(i_d+1\right) - H_y^{n-\frac{1}{2}}\left(i_d\right)\right] \\ - \frac{\Delta t}{\varepsilon_0\Delta x}\frac{P_{\text{ee}}^{zz,n} + P_{\text{ee}}^{zz,n-1} + P_{\text{em}}^{zy,n} + P_{\text{em}}^{zy,n-1}}{2}. \end{aligned} \tag{5.16}$$

The first line of this expression is perceived as the conventional FDTD update equation (4.11b), while the second-line terms are the corresponding effect of the metasurface discontinuity.

The auxiliary functions $P_{\text{ee}}^{zz,n}$ and $P_{\text{em}}^{zy,n}$ are obtained through discretization of (5.13a) and (5.13b), respectively. Substituting (5.8) for $\tilde{\chi}_{\text{ee}}^{zz}$ and $\tilde{\chi}_{\text{em}}^{zy}$ into (5.13a) and (5.13b), respectively, and simplifying, yields

$$\left(\omega_{0,\text{ee}}^2 + 2j\omega\gamma_{\text{ee}} - \zeta\omega^2\right)\tilde{P}_{\text{ee}}^{zz} = \varepsilon_0\omega_{\text{p,ee}}^2 j\omega\tilde{E}_{z,\text{av}}, \tag{5.17}$$

$$\left(\omega_{0,\text{em}}^2 + 2j\omega\gamma_{\text{em}} - \zeta\omega^2\right)\tilde{P}_{\text{em}}^{zy} = \omega_{\text{p,em}}^2\frac{j\omega}{c_0}\tilde{H}_{y,\text{av}}. \tag{5.18}$$

The time-domain counterparts of these relations are found by replacing $j\omega$ and $-\omega^2$ by $\frac{d}{dt}$ and $\frac{d^2}{dt^2}$, respectively, which yields

$$\left(\omega_{0,\mathrm{ee}}^2 + 2\gamma_{\mathrm{ee}}\frac{d}{dt} + \zeta\frac{d^2}{dt^2}\right) P_{\mathrm{ee}}^{zz} = \varepsilon_0\omega_{\mathrm{p,ee}}^2\frac{dE_{z,\mathrm{av}}}{dt}, \tag{5.19}$$

$$\left(\omega_{0,\mathrm{em}}^2 + 2\gamma_{\mathrm{em}}\frac{d}{dt} + \zeta\frac{d^2}{dt^2}\right) P_{\mathrm{em}}^{zy} = \frac{\omega_{\mathrm{p,em}}^2}{c_0}\frac{dH_{y,\mathrm{av}}}{dt}. \tag{5.20}$$

Discretization of these equations gives

$$\begin{aligned}&\omega_{0,\mathrm{ee}}^2 P_{\mathrm{ee}}^{zz,n} + 2\gamma_{\mathrm{ee}}\frac{P_{\mathrm{ee}}^{zz,n+1} - P_{\mathrm{ee}}^{zz,n-1}}{2\Delta t} + \\ &\zeta\frac{P_{\mathrm{ee}}^{zz,n+1} - 2P_{\mathrm{ee}}^{yy,n} + P_{\mathrm{ee}}^{zz,n-1}}{\Delta t^2} = \varepsilon_0\omega_{\mathrm{p,ee}}^2\frac{E_{z,\mathrm{av}}^{n+1} - E_{z,\mathrm{av}}^{n-1}}{2\Delta t},\end{aligned} \tag{5.21}$$

$$\begin{aligned}&\omega_{0,\mathrm{em}}^2 P_{\mathrm{em}}^{zy,n} + 2\gamma_{\mathrm{em}}\frac{P_{\mathrm{em}}^{zy,n+1} - P_{\mathrm{em}}^{zy,n-1}}{2\Delta t} + \\ &\zeta\frac{P_{\mathrm{em}}^{zy,n+1} - 2P_{\mathrm{em}}^{yx,n} + P_{\mathrm{em}}^{zy,n-1}}{\Delta t^2} = \frac{\omega_{\mathrm{p,em}}^2}{c_0}\frac{H_{y,\mathrm{av}}^{n+\frac{1}{2}} - H_{y,\mathrm{av}}^{n-\frac{1}{2}}}{\Delta t},\end{aligned} \tag{5.22}$$

whose resolution for $P_{\mathrm{ee}}^{zz,n}$ and $P_{\mathrm{em}}^{zy,n}$ gives the update equations as

$$\begin{aligned}P_{\mathrm{ee}}^{zz,n} = &-\frac{\Delta t^2\omega_{0,\mathrm{ee}}^2 - 2\zeta}{\Delta t\gamma_{\mathrm{ee}} + \zeta}P_{\mathrm{ee}}^{zz,n-1} - \frac{\zeta - \Delta t\gamma_{\mathrm{ee}}}{\zeta + \Delta t\gamma_{\mathrm{ee}}}P_{\mathrm{ee}}^{zz,n-2} \\ &+ \frac{\varepsilon_0\Delta t\omega_{\mathrm{p,ee}}^2}{2(\gamma_{\mathrm{ee}}\Delta t + \zeta)}\left[E_{z,\mathrm{av}}^{n} - E_{z,\mathrm{av}}^{n-2}\right],\end{aligned} \tag{5.23a}$$

$$\begin{aligned}P_{\mathrm{em}}^{zy,n} = &-\frac{\Delta t^2\omega_{0,\mathrm{em}}^2 - 2\zeta}{\Delta t\gamma_{\mathrm{em}} + \zeta}P_{\mathrm{em}}^{zy,n-1} - \frac{\zeta - \Delta t\gamma_{\mathrm{em}}}{\zeta + \Delta t\gamma_{\mathrm{em}}}P_{\mathrm{em}}^{zy,n-2} \\ &+ \frac{\Delta t\omega_{\mathrm{p,em}}^2}{c_0(\gamma_{\mathrm{em}}\Delta t + \zeta)}\left[H_{y,\mathrm{av}}^{n-\frac{1}{2}} - H_{y,\mathrm{av}}^{n-\frac{3}{2}}\right].\end{aligned} \tag{5.23b}$$

From (5.16), updating $E_z^n(i_d+1)$ requires the knowledge of $P_{\mathrm{ee}}^{zz,n}$. Whereas, from (5.23a), $P_{\mathrm{ee}}^{zz,n}$ itself depends on $E_z^n(i_d+1)$ via $E_{z,\mathrm{av}}^n$ [1]. Substituting (5.23a) into (5.16), and solving

[1] $E_{z,\mathrm{av}}^n = \frac{E_z^n(i_d) + E_z^n(i_d+1)}{2}$

for $E_z^n(i_d+1)$ gives the update equation as

$$E_z^n(i_d+1)\left[1+\frac{\Delta t^2\omega_{\mathrm{p,ee}}^2}{8\Delta x(\gamma_{\mathrm{ee}}\Delta t+\zeta)}\right]=E_z^{n-1}(i_d+1)+\frac{\Delta t}{\varepsilon_0\Delta z}\left[H_y^{n-\frac{1}{2}}(i_d+1)-H_y^{n-\frac{1}{2}}(i_d)\right] \tag{5.24}$$
$$-\frac{\Delta t^2\omega_{\mathrm{p,ee}}^2}{4\Delta x(\gamma_{\mathrm{ee}}\Delta t+\zeta)}\left[\frac{E_z^n(k)}{2}+E_{z,\mathrm{av}}^{n-2}\right]+c_1P_{\mathrm{ee}}^{zz,n-1}+c_2P_{\mathrm{ee}}^{zz,n-2}-\frac{\Delta t}{\varepsilon_0\Delta x}\frac{P_{\mathrm{em}}^{zy,n}+P_{\mathrm{em}}^{zy,n-1}}{2},$$

where $c_1=\frac{\Delta t}{2\varepsilon_0\Delta x}\left[-1+\frac{\Delta t^2\omega_{\mathrm{p,ee}}^2-2\zeta}{\gamma_{\mathrm{ee}}\Delta t+\zeta}\right]$, $c_2=\frac{\Delta t}{2\varepsilon_0\Delta x}\frac{-\gamma_{\mathrm{ee}}\Delta t+\zeta}{\gamma_{\mathrm{ee}}\Delta t+\zeta}$, and $P_{\mathrm{ee}}^{zz,n-1}$ is found upon replacing n by $n-1$ in (5.23a).

In an analogous manner substitution of (5.15b) into (5.10) yields

$$H_y^{n+\frac{1}{2}}(i_d)=H_y^{n-\frac{1}{2}}(i_d)+\frac{\Delta t}{\mu_0\Delta x}\left[E_z^n(i_d+1)-E_z^n(i_d)\right]- \tag{5.25}$$
$$\frac{\Delta t}{\mu_0\Delta x}\frac{M_{\mathrm{mm}}^{yy,n+\frac{1}{2}}+M_{\mathrm{mm}}^{yy,n-\frac{1}{2}}+M_{\mathrm{me}}^{yz,n+\frac{1}{2}}+M_{\mathrm{me}}^{yz,n-\frac{1}{2}}}{2}.$$

The first line of this expression is perceived as the conventional FDTD update equation (4.11a), while the second-line terms are the corresponding effect of the metasurface discontinuity. Similar to (5.23), the auxiliary functions $M_{\mathrm{mm}}^{yy,n+\frac{1}{2}}$ and $M_{\mathrm{me}}^{yz,n+\frac{1}{2}}$ are found through discretization of (5.13c) and (5.13d), respectively, as

$$M_{\mathrm{mm}}^{yy,n+\frac{1}{2}}=-\frac{\Delta t^2\omega_{0,\mathrm{mm}}^2-2\zeta}{\Delta t\gamma_{\mathrm{mm}}+\zeta}M_{\mathrm{mm}}^{yy,n-\frac{1}{2}}- \tag{5.26a}$$
$$\frac{\zeta-\Delta t\gamma_{\mathrm{mm}}}{\zeta+\Delta t\gamma_{\mathrm{mm}}}M_{\mathrm{mm}}^{yy,n-\frac{3}{2}}+\frac{\mu_0\Delta t\omega_{\mathrm{p,mm}}^2}{2(\gamma_{\mathrm{mm}}\Delta t+\zeta)}\left[H_{y,\mathrm{av}}^{n+\frac{1}{2}}-H_{y,\mathrm{av}}^{n-\frac{3}{2}}\right],$$

$$M_{\mathrm{me}}^{yz,n+\frac{1}{2}}=-\frac{\Delta t^2\omega_{0,\mathrm{me}}^2-2\zeta}{\Delta t\gamma_{\mathrm{me}}+\zeta}M_{\mathrm{me}}^{yz,n-\frac{1}{2}} \tag{5.26b}$$
$$-\frac{-\Delta t\gamma_{\mathrm{me}}+\zeta}{\Delta t\gamma_{\mathrm{me}}+\zeta}M_{\mathrm{me}}^{yz,n-\frac{1}{2}}+\frac{\Delta t\omega_{\mathrm{p,me}}^2}{c_0(\gamma_{\mathrm{me}}\Delta t+\zeta)}\left[E_{z,\mathrm{av}}^n-E_{z,\mathrm{av}}^{n-1}\right].$$

To update $H_y^{n+\frac{1}{2}}(i_d)$ in (5.25) the knowledge of $M_{\mathrm{mm}}^{yy,n+\frac{1}{2}}$ is required. whereas, from (5.26a), $M_{\mathrm{mm}}^{yy,n+\frac{1}{2}}$ depends on $H_y^{n+\frac{1}{2}}(i_d)$. Therefore, we Substitute (5.26a) into (5.25) and solve for

$M_{\mathrm{mm}}^{yy,n+\frac{1}{2}}$. This yields

$$H_y^{n+\frac{1}{2}}(i_d)\left[1+\frac{\Delta t^2\omega_{\mathrm{p,mm}}^2}{8\Delta x(\gamma_{\mathrm{mm}}\Delta t+\zeta)}\right]=H_y^{n-\frac{1}{2}}(i_d)+\frac{\Delta t}{\mu_0\Delta x}\left[E_z^n(i_d+1)-E_z^n(i_d)\right] \tag{5.27}$$
$$+c_3M_{\mathrm{mm}}^{yy,n-\frac{1}{2}}+\frac{\Delta t^2\omega_{\mathrm{p,mm}}^2}{4\Delta x(\gamma_{\mathrm{mm}}\Delta t+\zeta)}\left[\frac{H_y^{n+\frac{1}{2}}(i_d+1)}{2}-H_{y,\mathrm{av}}^{n-\frac{3}{2}}\right]$$
$$+c_4M_{\mathrm{mm}}^{yy,n-\frac{3}{2}}+\frac{\Delta t}{\mu_0\Delta x}\frac{M_{\mathrm{me}}^{yz,n+\frac{1}{2}}+M_{\mathrm{me}}^{yz,n-\frac{1}{2}}}{2},$$

with $c_3=\frac{\Delta t}{2\varepsilon_0\Delta x}\left[-1+\frac{\Delta t^2\omega_{\mathrm{p,mm}}^2-2\zeta}{\gamma_{\mathrm{mm}}\Delta t+\zeta}\right]$, $c_4=\frac{\Delta t}{2\varepsilon_0\Delta x}\frac{-\gamma_{\mathrm{mm}}\Delta t+\zeta}{\gamma_{\mathrm{mm}}\Delta t+\zeta}$ and $M_{\mathrm{mm}}^{zz,n-\frac{1}{2}}$ is found upon replacing $n+\frac{1}{2}$ with $n-\frac{1}{2}$ in (5.26a).

Equations. (5.24) and (5.27) are the final electric and magnetic update equations, respectively, for the nodes surrounding the metasurface. In the absence of the metasurface, $\omega_{\mathrm{p,ee}}=\omega_{\mathrm{p,mm}}=0$, they will reduce to the conventional FDTD equations (4.11). In summary, the dispersive bianisotropic metasurface problem is solved in FDTD using the our proposed auxiliary functions set.

For the time-varying susceptibilities, (5.19) and (5.20) should be modified properly. For example, assume the plasma frequency in χ_{ee} varies in time, $\omega_{\mathrm{p,ee}}=\omega_{\mathrm{p,ee}}(t)$. In this case, (5.19) yields

$$\left(\omega_{0,\mathrm{ee}}^2+2\gamma_{\mathrm{ee}}\frac{d}{dt}+\zeta\frac{d^2}{dt^2}\right)P_{\mathrm{ee}}^{yy}=\varepsilon_0\frac{d\omega_{\mathrm{p,ee}}^2(t)*E_{z,\mathrm{av}}}{dt}, \tag{5.28}$$

where $*$ is the convolution product. For the discretization of this expression, the left hand side will remain unchanged as in (5.21). However, in the right hand side, $\omega_{\mathrm{p,ee}}^2$ should be calculated at the appropriate time steps using convolutions, which yields

$$\varepsilon_0\frac{d}{dt}\int_0^t\omega_{\mathrm{p,ee}}^2(t-\tau)E_{z,\mathrm{av}}(\tau)d\tau= \tag{5.29}$$
$$\varepsilon_0\frac{\int_0^{(n+1)\Delta t}f(n+1,\tau)d\tau-\int_0^{(n-1)\Delta t}f(n-1,\tau)d\tau}{2\Delta t}=\frac{\varepsilon_0 f(n+1,\frac{\Delta t}{2})}{2\Delta t}$$
$$\frac{\varepsilon_0}{2\Delta t}\sum_{i=1}^{n}f\left(n+1,(i+0.5)\,\Delta t\right)-f\left(n-1,(i-0.5)\,\Delta t\right),$$

with $f(n,\tau)=\omega_{\mathrm{p,ee}}^2(n\Delta t-\tau)E_{z,\mathrm{av}}(\tau)$. Note that, although the formulation of the time-varying metasurface seems straightforward, however, there are quite a few interesting phenomena in the time-varying metasurfaces, for example, down-chirp or up-chirp and generation of higher order harmonics.

The formulation for the 2D and 3D problems follows exactly same procedure as mentioned

above. However, since there is not any particular new point in doing the formulation, which are long and tedious, we are not writing them here. The proposed formulation can be extended to include the spatial dispersion, which adds more complexity to the equations and derivation steps; and can be a future extension of the topic. This extension will require spatial Fourier transformation of the susceptibilities, addition of their spatial derivatives using $k_x = \frac{\partial}{\partial x}$, for example, in the FDTD equations and introducing corresponding spatial auxiliary functions.

5.3 Illustrative Simulation Results

All the following simulations, we will use the normalization $\varepsilon_0 = \mu_0 = c_0 = 1$ at the frequency $f = 1$ Hz with the sinusoidally modulated Gaussian source $E_z^{\text{inc}} = e^{-(\frac{t-t_0}{\tau})^2} \sin(\omega t)$, plotted in Fig. 5.3, where $t_0 = 3.6, \tau = 1$ and $\omega = 2\pi f$, unless otherwise specified.

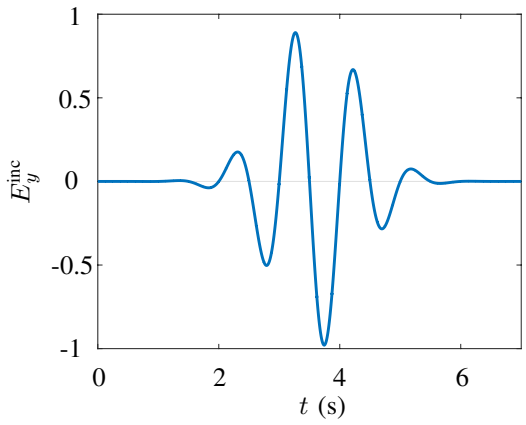

Figure 5.3 Waveform of the incident sinusoidally modulated Gaussian source.

Table 5.1 Summary of the three examples presented in this section along with the dimension of the computational area and the metasurface type.

Nb.	Dispersion	Scattering	dimension and type
1	Debye	$R, T \neq 0$	0, bianisotropic
2	Lorentz	$R = 0, T \neq 0$	0, bianisotropic
3	Lorentz	$R = 0, T = T(z)$	1, two anisot. metasur.

Table 5.1 summarizes the metasurface parameters and the expected scattering in the reflected and transmitted regions. In these examples, the results are compared with the analytic

solutions and computed, following the procedures described in [44], as

$$S_{11} = \frac{2jk_0\left(\chi_{\rm mm}^{yy} - \chi_{\rm ee}^{zz} + \chi_{\rm em}^{zy} - \chi_{\rm me}^{yz}\right)}{2jk_0\left(\chi_{\rm mm}^{yy} + \chi_{\rm ee}^{zz}\right) + k_0^2\chi_{\rm em}^{zy}\chi_{\rm me}^{yz} + 4 - k_0^2\chi_{\rm mm}^{yy}\chi_{\rm ee}^{zz}} \tag{5.30a}$$

$$S_{12} = \frac{k_0^2\chi_{\rm mm}^{yy}\chi_{\rm ee}^{zz} - \left(2j - k_0\chi_{\rm em}^{zy}\right)\left(2j - k_0\chi_{\rm me}^{yz}\right)}{2jk_0\left(\chi_{\rm mm}^{yy} + \chi_{\rm ee}^{zz}\right) + k_0^2\chi_{\rm em}^{zy}\chi_{\rm me}^{yz} + 4 - k_0^2\chi_{\rm mm}^{yy}\chi_{\rm ee}^{zz}} \tag{5.30b}$$

The susceptibilities for the first example (Tab. 5.1) are $\tilde{\chi}_{\rm me}^{yz} = \frac{2}{1+2j\omega}$ and $\tilde{\chi}_{\rm mm}^{yy} = \tilde{\chi}_{\rm ee}^{zz} = \tilde{\chi}_{\rm em}^{zy} = \frac{2}{1+0.7j\omega}$. Its simulation results are depicted in Figs. 5.4 and 5.5. In Fig. 5.4 the fields are plotted in different regions at the time $t = 5.8$ s. According to (5.30a), since the matching condition ($S_{11} = 0$) for a bianisotropic metasurface – $\chi_{\rm mm}^{yy} = \chi_{\rm ee}^{zz}$ and $\chi_{\rm em}^{zy} = \chi_{\rm me}^{yz}$ – is not satisfied in this example, therefore, the metasurface is not matched and the reflected field is non-zero ($E_z^{\rm r} \neq 0$). Figure. 5.5 illustrates the phase and amplitude of the Fourier transforms of the transmitted and reflected waves, which are in agreement with the analytic results calculated from (5.30).

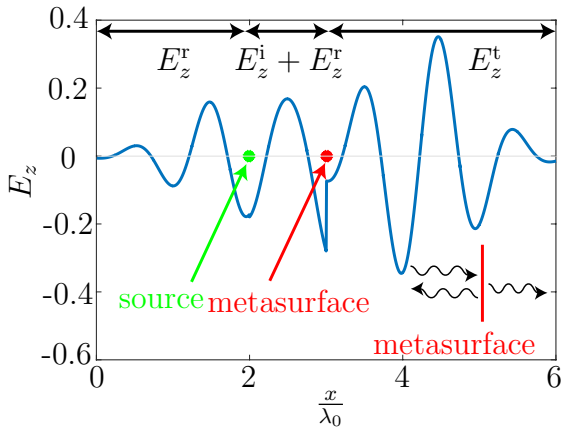

Figure 5.4 Example 1 (Tab. 5.1): Spatial variation of the simulated electric field at $t = 5.8$ s.

The susceptibilities for the second example (Tab. 5.1) are $\tilde{\chi}_{\rm ee}^{zz} = \tilde{\chi}_{\rm mm}^{yy} = \frac{2}{\omega_0^2+2j\omega\gamma-\omega^2}$ and $\tilde{\chi}_{\rm em}^{zy} = \tilde{\chi}_{\rm me}^{yz} = \frac{1}{\omega_0^2+2j\omega\gamma-\omega^2}$, where $\omega_0 = 2\pi 20$ and $\gamma = 8\omega_0$. In this case, the matching condition is satisfied and the reflection is expected to be zero. This condition is verified in Figs. 5.6 and 5.7. The simulated and analytical result for the phase and amplitude of the transmitted and reflected fields are in good agreement.

In the last example (Tab. 5.1), we consider two parallel space-varying anisotropic metasurfaces illuminated by a plane-wave ($\tilde{\chi}_{\rm em}^{zy} = \tilde{\chi}_{\rm me}^{yz} = 0$) having Lorentzian dispersion form. The metasurfaces are designed to be non-reflective and exhibit maximum transmission at their center and zero transmission at their edge, under a linear variation of the transmission, while

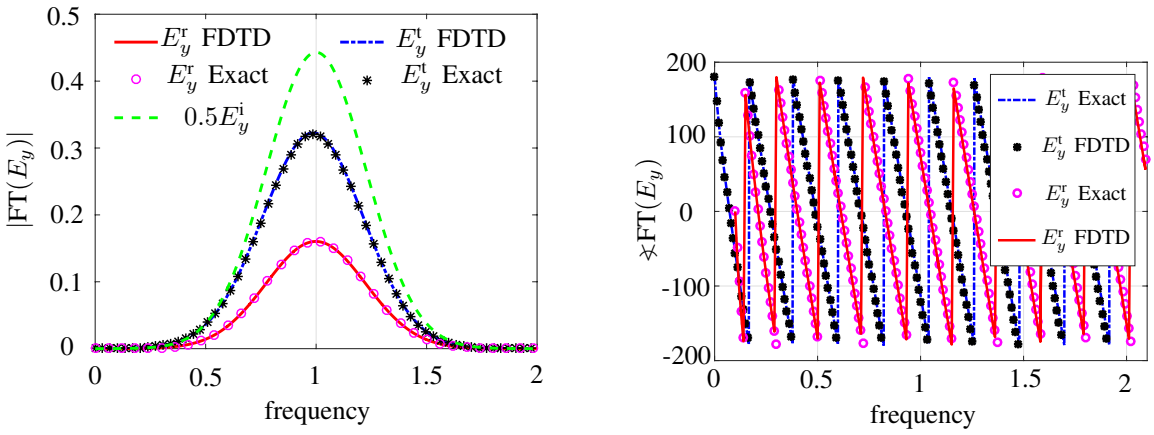

(a) (b)

Figure 5.5 Example 1 (Tab. 5.1): Fourier transform of the total (sum of the incident and reflected fields right before the metasurface) and transmitted (right after the metasurface) electric field in Fig. 5.4 and its comparison with the analytic result [Eq. (5.30)]. (a) Amplitudes. (b) Phases.

being matched with $\tilde{\chi}_{\mathrm{ee}}^{zz} = \tilde{\chi}_{\mathrm{mm}}^{yy} = \frac{\omega_{\mathrm{p}}^2}{\omega_0^2 + 2j\omega\gamma - \omega^2}$, where $\omega_{\mathrm{p}} = 2$ and $\omega_0 = 2\pi 20$. The linear variation of the metasurface absorption coefficient is controlled by γ as shown in Fig. 5.8.

We have numerically found that a single metasurface with Lorentz dispersion form cannot absorb the incident field completely. Therefore, we use the stack of two metasurfaces to achieve the total absorption. the distance between the metasurfaces are assumed 0.1λ, as shown in Fig. 5.9a. Figure 5.9a shows the 2D field distribution in the computational domain, where the metasurface exhibits the expected behaviour. This behavior is better illustrated in Fig. 5.9b, where the field distribution at $y = 0$ indicates a complete transmission of the incident field with a phase change, but zero transmition at $y = 3.75\lambda_0$.

5.4 Conclusion

We have presented a simple and efficient fully numeric Finite-Difference Time-Domain (FDTD) scheme for the simulation of dispersive – as well as nonlinear and time-varying, mentioned in the previous chapter – bianisotropic metasurfaces based on the Generalized Sheet Transition Conditions (GSTCs). Inspired by the conventional efficient ADE method, applied for the bulk materials simulation, we defined auxiliary polarization functions and brought the effect of the metasurface dispersion into our FDTD-GSTC computation. Being physically insightful, fully numeric, computationally efficient and easy to implement, this scheme is a fundamental contribution to FDTD. Therefore, these capabilities enable easy integration of

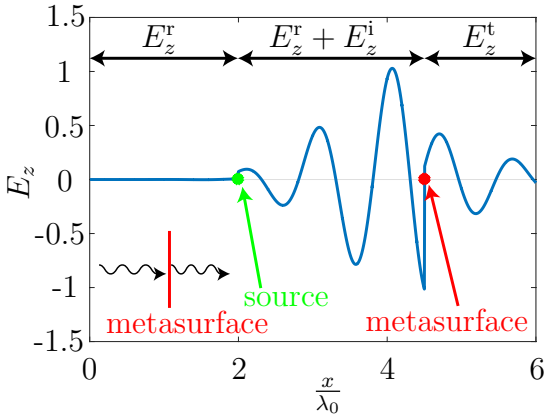

Figure 5.6 Example 2 (Tab. 5.1): Spatial variation of the simulated electric field at time $t = 3$ s.

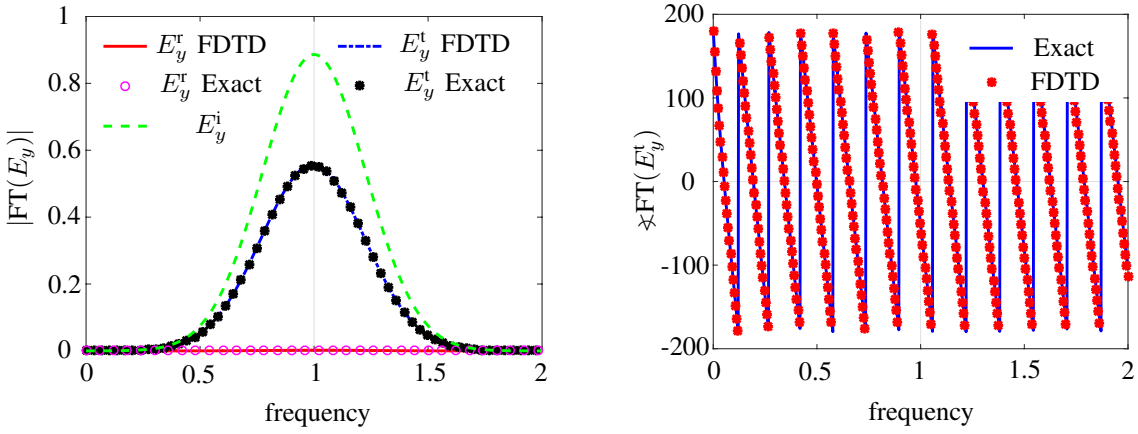

(a) (b)

Figure 5.7 Example 2 (Tab. 5.1): Fourier transform of the total (sum of the incident and reflected fields right before the metasurface) and transmitted (right after the metasurface) electric fields in Fig. 5.6 and its comparison with the analytic result, [Eq. (5.30)]. (a) Amplitudes. (b) Phases.

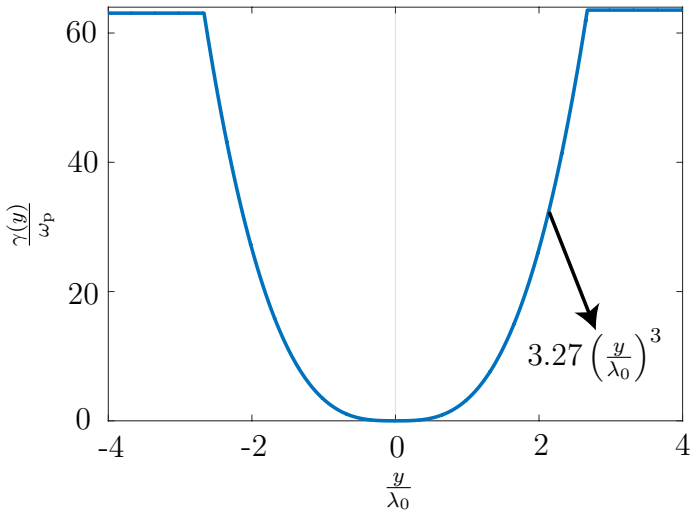

Figure 5.8 Example 3 (Tab. 5.1): Damping, $\gamma(y)$, profile for full absorption.

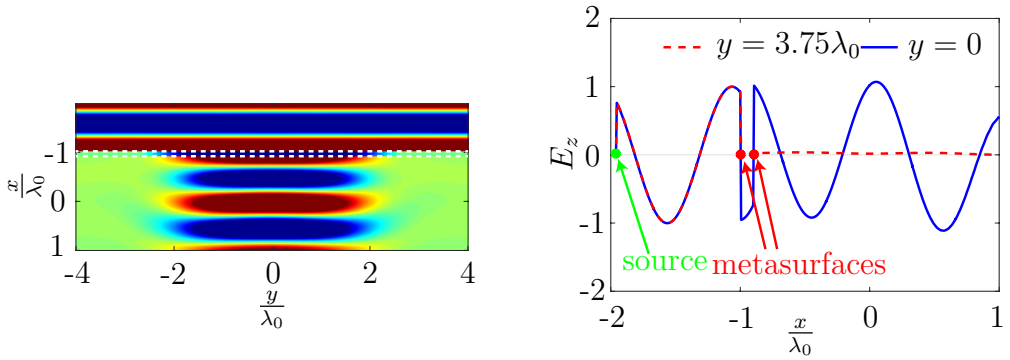

(a) (b)

Figure 5.9 Example 3 (Tab. 5.1): Two-metasurfaces configuration for the space-varying transmission with illumination in the $+x-$direction. (a) Spatial field distribution, with the metasurfaces located at $x = -\lambda_0$ and $x = -0.9\lambda_0$ shown by white dashed lines. (b) Field distribution in the $x-$direction for $y = 0$ and $y = 3.75\lambda_0$.

the GSTC equations with the commercial softwares only by modifying some coefficients in the FDTD equations, which currently cannot effectively simulate a metasurface.

CHAPTER 6 CONCLUSION

6.1 Summary of Works

In this thesis, we presented a complete metasurface analysis tool in the time and frequency domain. Compared to other methods proposed in the literature, our developments are: 1- Fully numeric, which allows easy integration with any commercial computation software, 2- General in the sense that it covers any form of metasurfaces including dispersive, bianisotropic and space-time varying, 3- Accurate, as there is no approximation in the discretization of the update equations and 4- Time and memory wise efficient compared to other developed techniques.

We introduced metasurfaces in Chapter 1. History of the conventional 3D metamaterials was presented, and the limitations that led to the appearance of metasurface were discussed. In the following chapter, we examined the conventional BCs and their weaknesses in the representation of general metasurface discontinuity. These restrictions led to the development of GSTCs. Then, metasurface GSTC synthesis techniques were discussed, where depending on the transmitted field's location, back-propagation or back-scattering may be required. We presented an example for each of the synthesis methods and discussed their limitations and usefulness. Then, the metasurface analysis techniques including approximate, and equivalent circuit methods are discussed. The conventional Non-GSTC techniques are approximate and applicable to the limited group of metasurfaces. Therefore, different approaches based on the integration of GSTCs with the FDTD, FDFD, FEM, and SD-IE were developed.

Initially, we integrated the GSTC with FDFD scheme. In this method, we introduced the metasurface as a virtual structure between the nodes. It successfully simulates temporal dispersive metasurfaces at a given frequency. Addition of the metasurface alters the differential and material matrix operators and makes them less-sparse. Therefore, the simulation time increases. However, the main concern on the GSTC-FDFD is monochromatic and its inapplicability to the time-varying metasurfaces.

This issue solved in Chapters 4 and 5. We first introduced GSTC in the FDTD for non-dispersive metasurfaces, where we applied the virtual node concept along with the virtual structure implementation of the metasurface, as in Chapter 1. This extension is not straightforward due to the staggered nature of the Yee and the related complexity in discretizing the field update equations. Then, the dispersion behavior was taken into account in Chapter 5 via ADE technique, which is the modified version of the traditional efficient ADE applied for

the simulation of conventional bulk dispersive materials.

Each of the developed methods was validated by many illustrative examples. We compared the COMSOL simulation results, where metasurface is approximated by a diluted subwavelength slab, with the GSTS-FDFD in Chapter 1 and showed the discrepancy between these two and accuracy of the GSTC-FDFD. In other examples, we compared the result of our technique with the analytic result or the synthesis specifications.

6.2 Limitations

In some applications, a metasurface may be spatially dispersive. However, in all of our developments, we ignored this non-locality. Similar to the GSTC-FDFD, which is limited to monochromatic metasurfaces, all of our developments are limited to single spatial dispersion. Since higher-order GSTCs involves spatial derivatives of the fields, therefore, they represent spatial dispersion. Consequently, their simulation will require spatial dispersion consideration.

Secondly, for the large-scale problems, our method is less efficient. For instance, consider a large planar array of antennas covered by metasurfaces. Performing mesh over full computation domain of this problem is impossible due to simultaneous presence of very small and very large structures in the solving region. Therefore, conventional FD methods are implemented on the GPU or CPU for their simulation. However, in all of our formulations and discussions, we were limited to the small-scale metasurfaces.

Moreover, a metasurface is not always planar, and it can have any shape and curvature as in Fig. 6.1. However, during this thesis, we discussed only the planar metasurfaces. Non-planar metasurfaces will require modification of the all components of the field in the update equations.

6.3 Future Research

As we mentioned earlier, a limitation of our method is its inefficiency for the large-scale problems. Therefore, it is crucial to enhance the developments and combine them with other numerical techniques such as geometrical optics and transmission line method, and adjust them for the GPU and CPU implementation. This will bring more applications of the metasurfaces and will boost its diversity. That also will be useful for the simulation of other discontinuity structure such as graphene and electron gas since GSTC is the generalized version of all those BCs.

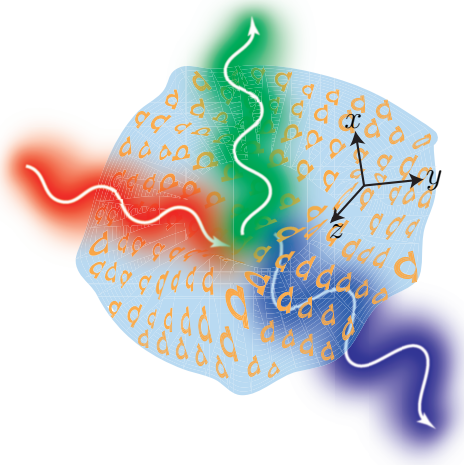

Figure 6.1 Schematic of a curved metasurface.

Since the majority of commercial softwares are based on FEM method (finite element method), GSTC-FEM will facilitate the metasurface simulation. Currently, GSTCs are developed under FEM scheme for anisotropic metasurfaces [141]. However, due to increasing applications of bianisotropic metasurfaces, it is crucial to add the required extensions to the GSTC-FEM. This extension is not straight-forward due to the presence of the spatial derivative of the fields for the bianisotropic metasurface.

BIBLIOGRAPHY

[1] D. Güney, T. Koschny, and C. M. Soukoulis, "Intra-connected three-dimensionally isotropic bulk negative index photonic metamaterial," *Opt. Express*, vol. 18, no. 12, pp. 12 348–12 353, 2010.

[2] B. Wang, J. Zhou, T. Koschny, M. Kafesaki, and C. M. Soukoulis, "Chiral metamaterials: simulations and experiments," *J. Opt. A: Pure Appl. Opt.*, vol. 11, no. 11, p. 114003, 2009.

[3] S. P. Burgos, R. D. Waele, A. Polman, and H. A. Atwater, "A single-layer wide-angle negative-index metamaterial at visible frequencies," *Nat. Mater*, vol. 9, no. 5, p. 407, 2010.

[4] Y. Vahabzadeh, N. Chamanara, K. Achouri, and C. Caloz, "Computational analysis of metasurfaces," *IEEE J. Multiscale and Multiphys. Comput. Techn.*, vol. 3, pp. 37–49, 2018.

[5] K. Achouri, M. Salem, and C. Caloz, "Improvement of metasurface continuity conditions." ISAP, 2015, pp. 123–125.

[6] T. J. Smy and S. Gupta, "Finite-difference modeling of broadband Huygens' metasurfaces based on generalized sheet transition conditions," *IEEE Trans. Antennas Propag.*, vol. 65, no. 5, pp. 2566–2577, 2017.

[7] V. Nayyeri, M. Soleimani, and O. Ramahi, "Modeling graphene in the finite-difference time-domain method using a surface boundary condition," *IEEE Trans. Antennas Propag.*, vol. 61, no. 8, pp. 4176–4182, Aug 2013.

[8] V. I. Karpman, "High frequency electromagnetic field in plasma with negative dielectric constant," *Plasma Phys. Control. Fusion*, vol. 13, no. 6, p. 477, 1971.

[9] D. L. Mills and E. Burstein, "Polaritons: the electromagnetic modes of media," *Rep. Prog. Phys.*, vol. 37, no. 7, p. 817, 1974.

[10] D. A. Kirzhnits, "Are the Kramers-Kronig relations for the dielectric permittivity of a material always valid?" *Phys.-Uspekhi*, vol. 19, no. 6, pp. 530–537, 1976.

[11] R. Kronig, "On the theory of dispersion of x-rays," *J. Opt. Soc. Am.*, vol. 12, no. 6, pp. 547–557, 1926.

[12] H. Lamb, *Hydrodynamics.* University Press, 1895.

[13] L. I. Mandel'shtam, "Group velocity in a crystal lattice," *Zh. Eksp. Teor. Fiz*, vol. 15, no. 9, pp. 475–478, 1945.

[14] V. E. Pafomov, "Transition radiation and cerenkov radiation," *Soviet. Phys. JETP*, vol. 9, p. 1321, 1959.

[15] H. C. Pocklington, "Growth of a wave-group when the group velocity is negative," *Nature*, vol. 71, no. 1852, pp. 607–608, 1905.

[16] V. G. Veselago, "The electrodynamics of substances with simultaneously negative values of ε and μ," *Phys.-Uspekhi*, vol. 10, no. 4, p. 509, 1968.

[17] R. A. Shelby, D. R. Smith, S. Nemat-Nasser, and S. Schultz, "Microwave transmission through a two-dimensional, isotropic, left-handed metamaterial," *Appl. Phys. Lett.*, vol. 78, no. 4, pp. 489–491, 2001.

[18] D. R. Smith, W. J. Padilla, D. C. Vier, S. C. Nemat-Nasser, and S. Schultz, "Composite medium with simultaneously negative permeability and permittivity," *Appl. Phys. Lett.*, vol. 84, no. 18, p. 4184, 2000.

[19] A. Sihvola, I. Semchenko, and S. Khakhomov, "View on the history of electromagnetics of metamaterials: Evolution of the congress series of complex media," *Photonics Nanostructures: Fundam. Appl.*, vol. 12, no. 4, pp. 279–283, 2014.

[20] R. M. Walser, "Electromagnetic metamaterials," in *Complex Mediums II: Beyond Linear Isotropic Dielectrics*, vol. 4467. International Society for Optics and Photonics, 2001, pp. 1–16.

[21] V. I. Slyusar, "Metamaterials on antenna solutions," 2009.

[22] T. Kodera, D. L. Sounas, and C. Caloz, "Magnetless nonreciprocal metamaterial (MNM) technology: application to microwave components," *IEEE Trans. Microw. Theory Tech.*, vol. 61, no. 3, pp. 1030–1042, 2013.

[23] D. Schurig, J. J. Mock, B. J. Justice, S. A. Cummer, J. B. Pendry, A. F. Starr, and D. R. Smith, "Metamaterial electromagnetic cloak at microwave frequencies," *Science*, vol. 314, no. 5801, pp. 977–980, 2006.

[24] W. Cai, U. K. Chettiar, A. V. Kildishev, and V. M. Shalaev, "Optical cloaking with metamaterials," *Nat. Photonics*, vol. 1, no. 4, p. 224, 2007.

[25] A. D. J. B. Pendry, "Taming spatial dispersion in wire metamaterial," *J. Phys. Condens. Matter*, vol. 20, no. 29, p. 295222, 2008.

[26] D. Ye, Z. Wang, K. Xu, H. Li, J. Huangfu, Z. Wang, and L. Ran, "Ultrawideband dispersion control of a metamaterial surface for perfectly-matched-layer-like absorption," *Phys. Rev. Lett.*, vol. 111, no. 18, p. 187402, 2013.

[27] Y. Guo, Y. Wang, M. Pu, Z. Zhao, X. Wu, X. Ma, C. Wang, L. Yan, and X. Luo, "Dispersion management of anisotropic metamirror for super-octave bandwidth polarization conversion," *Sci. Rep.*, vol. 5, p. 8434, 2015.

[28] R. W. Ziolkowski and A. Erentok, "Metamaterial-based efficient electrically small antennas," *IEEE Trans. Antennas Propag.*, vol. 54, no. 7, pp. 2113–2130, 2006.

[29] C. M. Soukoulis and M. Wegener, "Past achievements and future challenges in the development of three-dimensional photonic metamaterials," *Nat. Photonics*, vol. 5, no. 9, p. 523, 2011.

[30] Y. Zhou, X. Y. Chen, Y. H. Fu, G. Vienne, A. I. Kuznetsov, and B. Luk'Yanchuk, "Fabrication of large-area 3D optical fishnet metamaterial by laser interference lithography," *Appl. Phys. Lett.*, vol. 103, no. 12, p. 123116, 2013.

[31] G. Yoon, I. Kim, and J. Rho, "Challenges in fabrication towards realization of practical metamaterials," *Microelectron. Eng.*, vol. 163, pp. 7–20, 2016.

[32] J. B. Khurgin, "How to deal with the loss in plasmonics and metamaterials," *Nat. Nanotechnol.*, vol. 10, no. 1, p. 2, 2015.

[33] C. M. Soukoulis and M. Wegener, "Optical metamaterials—more bulky and less lossy," *Science*, vol. 330, no. 6011, pp. 1633–1634, 2010.

[34] H. Lamb, "On the reflection and transmission of electric waves by a metallic grating," *P. Lond. Math. Soc.*, vol. 1, no. 1, pp. 523–546, 1897.

[35] R. Landauer, "The electrical resistance of binary metallic mixtures," *J. Appl. Phys.*, vol. 23, no. 7, pp. 779–784, 1952.

[36] J. S. Yee, "Frequency selective surface (FSS)," May 4 1993, US Patent 5,208,603.

[37] R. Mittra, C. H. Chan, and T. Cwik, "Techniques for analyzing frequency selective surfaces-a review," *Proc. IEEE*, vol. 76, no. 12, pp. 1593–1615, 1988.

[38] P. Padilla, A. Muñoz-Acevedo, and M. Sierra-Castañer, "Passive planar transmit-array microstrip lens for microwave purpose," *Microw. Opt. Technol. Lett.*, vol. 52, no. 4, pp. 940–947, 2010.

[39] D. McGrath, "Planar three-dimensional constrained lenses," *IEEE Trans. Antennas Propag.*, vol. 34, no. 1, pp. 46–50, 1986.

[40] J. Vian and Z. Popovic, "Smart lens antenna arrays," in *Microwave Symposium Digest, 2001 IEEE MTT-S International*, vol. 1. IEEE, 2001, pp. 129–132.

[41] D. Pozar, S. Targonski, and R. Pokuls, "A shaped-beam microstrip patch reflectarray," *IEEE Trans. Antennas Propag.*, vol. 47, no. 7, pp. 1167–1173, 1999.

[42] R. Leberer and W. Menzel, "A dual planar reflectarray with synthesized phase and amplitude distribution," *IEEE Trans. Antennas Propag.*, vol. 53, no. 11, pp. 3534–3539, 2005.

[43] E. J. Rothwell and M. J. Cloud, *Electromagnetics, 2nd edition*. CRC Press, 2008.

[44] K. Achouri, M. A. Salem, and C. Caloz, "General metasurface synthesis based on susceptibility tensors," *IEEE Trans. Antennas Propag.*, vol. 63, no. 7, pp. 2977–2991, July 2015.

[45] E. F. Kuester, M. A. Mohamed, M. Piket-May, and C. L. Holloway, "Averaged transition conditions for electromagnetic fields at a metafilm," *IEEE Trans. Antennas Propag.*, vol. 51, no. 10, pp. 2641–2651, Oct 2003.

[46] M. M. Idemen, *Discontinuities in the Electromagnetic Field*. John Wiley & Sons, 2011.

[47] J. M. Jin, *Theory and Computation of Electromagnetic Fields*. Wiley, 2011.

[48] N. Yu, P. Genevet, M. A. Kats, F. Aieta, J. P. Tetienne, F. Capasso, and Z. Gaburro, "Light propagation with phase discontinuities: generalized laws of reflection and refraction," *Science*, vol. 334, no. 6054, pp. 333–337, 2011.

[49] F. Aieta, P. Genevet, N. Yu, M. A. Kats, Z. Gaburro, and F. Capasso, "Out-of-plane reflection and refraction of light by anisotropic optical antenna metasurfaces with phase discontinuities," *Nano Lett.*, vol. 12, no. 3, pp. 1702–1706, 2012.

[50] S. Larouche and D. R. Smith, "Reconciliation of generalized refraction with diffraction theory," *Opt. Lett.*, vol. 37, no. 12, pp. 2391–2393, 2012.

[51] A. Shaltout, V. Shalaev, and A. Kildishev, "Homogenization of bi-anisotropic metasurfaces," *Opt. Express*, vol. 21, no. 19, pp. 21 941–21 950, 2013.

[52] M. Yazdi, M. Albooyeh, R. Alaee, V. Asadchy, N. Komjani, C. Rockstuhl, C. R. Simovski, and S. Tretyakov, "A bianisotropic metasurface with resonant asymmetric absorption," *IEEE Trans. Antennas Propag.*, vol. 63, no. 7, pp. 3004–3015, 2015.

[53] Y. Yang, I. I. Kravchenko, D. P. Briggs, and J. Valentine, "All-dielectric metasurface analogue of electromagnetically induced transparency," *Nat. Commun.*, vol. 5, p. 5753, 2014.

[54] C. Pfeiffer and A. Grbic, "Metamaterial Huygens' surfaces: tailoring wave fronts with reflectionless sheets," *Phys. Rev. Lett.*, vol. 110, no. 19, p. 197401, 2013.

[55] ——, "Bianisotropic metasurfaces for optimal polarization control: Analysis and synthesis," *Phys. Rev. Appl.*, vol. 2, no. 4, p. 044011, 2014.

[56] J. P. Wong, M. Selvanayagam, and G. V. Eleftheriades, "Design of unit cells and demonstration of methods for synthesizing Huygens metasurfaces," *Photonics Nanostructures: Fundam. Appl.*, vol. 12, no. 4, pp. 360–375, 2014.

[57] T. Niemi, A. O. Karilainen, and S. A. Tretyakov, "Synthesis of polarization transformers," *IEEE Trans. Antennas Propag.*, vol. 61, no. 6, pp. 3102–3111, 2013.

[58] Y. Zhao, X. X. Liu, and A. Alù, "Recent advances on optical metasurfaces," *J. Opt.*, vol. 16, no. 12, p. 123001, 2014.

[59] S. A. Tretyakov, "Metasurfaces for general transformations of electromagnetic fields," *Philos. Trans. R. Soc. A*, vol. 373, no. 2049, p. 20140362, 2015.

[60] T. Yue, Z. H. Jiang, and D. H. Werner, "Compact, wideband antennas enabled by interdigitated capacitor-loaded metasurfaces," *IEEE Trans. Antennas Propag.*, vol. 64, no. 5, pp. 1595–1606, 2016.

[61] W. E. I. Liu, Z. N. Chen, X. Qing, J. Shi, and F. H. Lin, "Miniaturized wideband metasurface antennas," *IEEE Trans. Antennas Propag.*, vol. 65, no. 12, pp. 7345–7349, Dec 2017.

[62] G. Zheng, H. Mühlenbernd, M. Kenney, G. Li, T. Zentgraf, and S. Zhang, "Metasurface holograms reaching 80% efficiency," *Nat. Nanotechnol.*, vol. 10, no. 4, p. 308, 2015.

[63] q. Wang, X. Zhang, Y. Xu, J. Gu, Y. Li, Z. Tian, R. Singh, S. Zhang, J. Han, and W. Zhang, "Broadband metasurface holograms: toward complete phase and amplitude engineering," *Sci. Rep.*, vol. 6, p. 32867, 2016.

[64] L. Li, T. J. Cui, W. Ji, S. Liu, J. Ding, X. Wan, Y. B. Li, M. Jiang, C. W. Qiu, and S. Zhang, "Electromagnetic reprogrammable coding-metasurface holograms," *Nat. Commun.*, vol. 8, no. 1, p. 197, 2017.

[65] A. K. Azad, A. V. Efimov, S. Ghosh, J. Singleton, A. J. Taylor, and H. T. Chen, "Ultra-thin metasurface microwave flat lens for broadband applications," *Appl. Phys. Lett.*, vol. 110, no. 22, p. 224101, 2017.

[66] R. Paniagua-Dominguez, Y. F. Yu, E. Khaidarov, S. Choi, V. Leong, R. M. Bakker, X. Liang, Y. H. Fu, V. Valuckas, L. A. Krivitsky *et al.*, "A metalens with a near-unity numerical aperture," *Nano lett.*, vol. 18, no. 3, pp. 2124–2132, 2018.

[67] X. Ni, Z. J. Wong, M. Mrejen, Y. Wang, and X. Zhang, "An ultrathin invisibility skin cloak for visible light," *Science*, vol. 349, no. 6254, pp. 1310–1314, 2015.

[68] N. M. Estakhri and A. Alù, "Ultra-thin unidirectional carpet cloak and wavefront reconstruction with graded metasurfaces," *IEEE Antennas Wirel. Propag. Lett.*, vol. 13, pp. 1775–1778, 2014.

[69] Y. Li, X. Li, L. Chen, M. Pu, J. Jin, M. Hong, and X. Luo, "Orbital angular momentum multiplexing and demultiplexing by a single metasurface," *Adv. Opt. Mater.*, vol. 5, no. 2, p. 1600502, 2017.

[70] S. Xiao, J. Wang, F. Liu, S. Zhang, X. Yin, and J. Li, "Spin-dependent optics with metasurfaces," *Nanophotonics*, vol. 6, no. 1, pp. 215–234, 2016.

[71] Y. Ran, J. Liang, T. Cai, and H. Li, "High-performance broadband vortex beam generator using reflective Pancharatnam–Berry metasurface," *Opt. Commun.*, vol. 427, pp. 101–106, 2018.

[72] S. Pandi, C. A. Balanis, and C. R. Birtcher, "Design of scalar impedance holographic metasurfaces for antenna beam formation with desired polarization," *IEEE Trans. Antennas Propag.*, vol. 63, no. 7, pp. 3016–3024, 2015.

[73] H. Yang, X. Cao, F. Yang, J. Gao, S. Xu, M. Li, X. Chen, Y. Zhao, Y. Zheng, and S. Li, "A programmable metasurface with dynamic polarization, scattering and focusing control," *Sci. Rep.*, vol. 6, p. 35692, 2016.

[74] Y. Vahabzadeh, K. Achouri, and C. Caloz, "Simulation of metasurfaces in finite difference techniques," *IEEE Trans. Antennas Propag.*, vol. 64, no. 11, pp. 4753–4759, Nov 2016.

[75] Y. Vahabzadeh, N. Chamanara, and C. Caloz, "Generalized sheet transition condition FDTD simulation of metasurface," *IEEE Trans. Antennas Propag.*, vol. 66, no. 1, pp. 271–280, 2018.

[76] X. Liu, F. Yang, M. Li, and S. Xu, "Reflectarray element analysis based on generalized sheet transition conditions," in *2017 11th European Conference on Antennas and Propagation (EUCAP)*, March 2017, pp. 2330–2333.

[77] M. Selvanayagam and G. V. Eleftheriades, "Polarization control using tensor huygens surfaces," *IEEE Trans. Antennas Propag.*, vol. 62, no. 12, pp. 6155–6168, 2014.

[78] M. Albooyeh, S. Tretyakov, and C. Simovski, "Electromagnetic characterization of bianisotropic metasurfaces on refractive substrates: General theoretical framework," *Ann. Phys.*, vol. 528, no. 9-10, pp. 721–737, 2016.

[79] K. Achouri and C. Caloz, "Design, concepts, and applications of electromagnetic metasurfaces," *Nanophotonics*, vol. 7, no. 6, pp. 1095–1116, 2018.

[80] G. Lavigne, K. Achouri, V. S. Asadchy, S. A. Tretyakov, and C. Caloz, "Susceptibility derivation and experimental demonstration of refracting metasurfaces without spurious diffraction," *IEEE Trans. Antennas Propag.*, vol. 66, no. 3, pp. 1321–1330, 2018.

[81] J. A. Kong, "Theorems of bianisotropic media," *Proc. IEEE*, vol. 60, no. 9, pp. 1036–1046, 1972.

[82] B. D. Popovic, "Electromagnetic field theorems," *Proc. Inst. Elec., A,*, vol. 128, no. 1, pp. 47–63, 1981.

[83] E. Yablonovitch and D. Sievenpiper, "Circuit and method for eliminating surface currents on metals," 17 2001, uS Patent 6,262,495.

[84] D. Sievenpiper, L. Zhang, R. F. Broas, N. G. Alexopolous, E. Yablonovitch *et al.*, "High-impedance electromagnetic surfaces with a forbidden frequency band," *IEEE Trans. Microw. Theory Tech.*, vol. 47, no. 11, pp. 2059–2074, 1999.

[85] V. A. Fock, "Diffraction, refraction, and reflection of radio waves," Air Force Cambridge Research Labs HANSCOM AFB MA, Tech. Rep., 1957.

[86] T. A. Senior, "Impedance boundary conditions for imperfectly conducting surfaces," *Appl. Sci. Res., Sec. B*, vol. 8, no. 1, p. 418, 1960.

[87] D. K. Cheng, *Field and Wave Electromagnetics (2nd Edition)*. Pearson;, 1989.

[88] S. A. Schelkunoff, "On teaching the undergraduate electromagnetic theory," *IEEE Trans. Educ.*, vol. 15, no. 1, pp. 15–25, Feb 1972.

[89] S. Tretyakov, *Analytical Modeling in Applied Electromagnetics*. Artech House, 2003.

[90] N. Chamanara, D. Sounas, and C. Caloz, "Non-reciprocal magnetoplasmon graphene coupler," *Opt. Express*, vol. 21, no. 9, pp. 11 248–11 256, May 2013.

[91] N. Chamanara, D. Sounas, T. Szkopek, and C. Caloz, "Terahertz magnetoplasmon energy concentration and splitting in graphene PN junctions," *Opt. Express*, vol. 21, no. 21, pp. 25 356–25 363, Oct. 2013.

[92] C. Berger, Z. Song, T. Li, X. Li, A. Y. Ogbazghi *et al.*, "Ultrathin epitaxial graphite: 2D electron gas properties and a route toward graphene-based nanoelectronics," *J. Phys. Chem. B*, vol. 108, no. 52, pp. 19 912–19 916, 2004.

[93] D. C. Tsui, S. J. A. Jr, R. A. Logan, A. Kamgar, and S. N. Coppersmith, "High frequency conductivity in silicon inversion layers: Drude relaxation, 2D plasmons and minigaps in a surface superlattice," *Surf. Sci.*, vol. 73, pp. 419–433, 1978.

[94] H. Ammari and S. He, "Effective impedance boundary conditions for an inhomogeneous thin layer on a curved metallic surface," *IEEE Trans. Antennas Propag.*, vol. 46, no. 5, pp. 710–715, 1998.

[95] D.-S. Wang, "Limits and validity of the impedance boundary condition on penetrable surfaces," *IEEE Trans. Antennas Propag.*, vol. 35, no. 4, pp. 453–457, 1987.

[96] I. V. Lindell and A. H. Sihvola, "Realization of impedance boundary," *IEEE Trans. Antennas Propag.*, vol. 54, no. 12, pp. 3669–3676, 2006.

[97] R. Cicchetti and A. Faraone, "Exact surface impedance/admittance boundary conditions for complex geometries: Theory and applications," *IEEE Trans. Antennas Propag.*, vol. 48, no. 2, pp. 223–230, 2000.

[98] I. V. Lindell and A. H. Sihvola, "Realization of the PEMC boundary," *IEEE Trans. Antennas Propag.*, vol. 53, no. 9, pp. 3012–3018, 2005.

[99] ——, "Perfect electromagnetic conductor," *J. ELECTROMAGNET. WAVE*, vol. 19, no. 7, pp. 861–869, 2005.

[100] P. Kurasov, "Distribution theory for discontinuous test functions and differential operators with generalized coefficients," *J. Math. Anal. Appl.*, vol. 201, no. 1, pp. 297 – 323, 1996.

[101] K. Achouri, Y. Vahabzadeh, and C. Caloz, "Mathematical synthesis and analysis of a second-order magneto-electrically nonlinear metasurface," *Opt. Express*, vol. 25, no. 16, pp. 19 013–19 022, Aug 2017.

[102] A. Ishimaru, *Electromagnetic Wave Propagation, Radiation, and Scattering*, 2nd ed. Wiley-IEEE Press, 2017.

[103] J. A. Kong, *Electromagnetic Wave theory*, 2nd ed. John Wiley & Sons Inc, 1986.

[104] K. Achouri, "Synthesis and applications of electromagnetic metasurfaces," Ph.D. dissertation, École Polytechnique de Montréal, 2017.

[105] A. M. Wong and G. V. Eleftheriades, "Perfect anomalous reflection with a bipartite Huygens' metasurface," *Phys. Rev. X*, vol. 8, no. 1, p. 011036, 2018.

[106] M. S. Mirmoosa, Y. Ra'di, V. S. Asadchy, C. R. Simovski, and S. A. Tretyakov, "Polarizabilities of nonreciprocal bianisotropic particles," *Phys. Rev. Appl*, vol. 1, no. 3, p. 034005, 2014.

[107] H. Nematollahi, J. J. Laurin, J. E.Page, and J. A. Encinar, "Design of broadband transmitarray unit cells with comparative study of different numbers of layers," *IEEE Trans. Antennas Propag.*, vol. 63, no. 4, pp. 1473–1481, 2015.

[108] E. Topsakal, J. L. Volakis, and D. Ross, "Surface integral equations for material layers modeled with tensor boundary conditions," *Radio Sci.*, vol. 37, no. 4, pp. 1–6, 2002.

[109] M. Dehmollaian, G. Lavigne, and C. Caloz, "Comparison of tensor boundary conditions (TBCs) with generalized sheet transition conditions (GSTCs)," *arXiv:1901.10414*.

[110] E. Knill, R. Laflamme, and G. J. Milburn, "A scheme for efficient quantum computation with linear optics," *Nature*, vol. 409, no. 6816, p. 46, 2001.

[111] P. Hariharan, *Basics of Interferometry*. Academic Press, 1991.

[112] L. Novotny and B. Hecht, *Principles of nano-optics*. Cambridge University Press, 2006.

[113] O. M. Bucci and T. Isernia, "Electromagnetic inverse scattering: Retrievable information and measurement strategies," *Radio Sci.*, vol. 32, no. 6, pp. 2123–2137, 1997.

[114] K. I. Hopcraft and P. R. Smith, *An Introduction to Electromagnetic Inverse Scattering (Developments in Electromagnetic Theory and Applications).* Springer; 1992 edition, 1992.

[115] Y. Álvarez, F. Las-Heras, and M. R. Pino, "Reconstruction of equivalent currents distribution over arbitrary three-dimensional surfaces based on integral equation algorithms," *IEEE Trans. Antennas Propag.*, vol. 55, no. 12, pp. 3460–3468, 2007.

[116] J. L. A. Quijano and G. Vecchi, "Improved-accuracy source reconstruction on arbitrary 3-D surfaces," *IEEE Antennas Wirel. Propag. Lett.*, vol. 8, pp. 1046–1049, 2009.

[117] J. Babington, *Basic Electromagnetic Theory (Essentials of Physics Series).* Mercury Learning & Information, 2016.

[118] T. Brown, C. Narendra, and P. Mojabi, "On the use of the source reconstruction method for metasurface design," 2018.

[119] T. Brown, C. Narendra, Y. Vahabzadeh, C. Caloz, , and P. Mojabi, "Macroscopic metasurface design using electromagnetic inversion," in *2019 IEEE International Symposium on Antennas and Propagation (APSURSI).* IEEE, 2019.

[120] X. Luo, M. Pu, X. Ma, and X. Li, "Taming the electromagnetic boundaries via metasurfaces: from theory and fabrication to functional devices," *Int J Antennas Propag*, vol. 2015, 2015.

[121] P. Baccarelli, F. Capolino, S. Paulotto, and A. B. Yakovlev, "In-plane modal analysis of a metalayer formed by arrayed pairs of dogbone-shaped conductors," *Metamaterials*, vol. 5, no. 1, pp. 26–35, 2011.

[122] F. Capolino, A. Vallecchi, and M. Albani, "Equivalent transmission line model with a lumped X-circuit for a metalayer made of pairs of planar conductors," *IEEE Trans. Antennas Propag.*, vol. 61, no. 2, pp. 852–861, 2013.

[123] A. Vallecchi, A. Schuchinsky, and F. Capolino, "Reconfigurable metasurface comprised of dogbone shaped conductor pairs," in *2015 IEEE International Symposium on Antennas and Propagation & USNC/URSI National Radio Science Meeting.* IEEE, 2015, pp. 1098–1099.

[124] A. H. Dorrah and G. V. Eleftheriades, "Bianisotropic Huygens' metasurface pairs for nonlocal power-conserving wave transformations," *IEEE Antennas Wirel. Propag. Lett.*, vol. 17, no. 10, pp. 1788–1792, 2018.

[125] B. O. Raeker and A. Grbic, "Compound metaoptics for amplitude and phase control of wave fronts," *Phys. Rev. Lett.*, vol. 122, no. 11, p. 113901, 2019.

[126] M. Danaeifar, N. Granpayeh, N. A. Mortensen, and S. Xiao, "Equivalent conductivity method: straightforward analytical solution for metasurface-based structures," *J. Phys. D Appl. Phys.*, vol. 48, no. 38, p. 385106, 2015.

[127] M. Danaeifar and N. Granpayeh, "Analysis of metasurface based structures by using equivalent conductivity method," in *2016 Days on Diffraction (DD)*. IEEE, 2016, pp. 118–122.

[128] S. Barzegar-Parizi, B. Rejaei, and A. Khavasi, "Analytical circuit model for periodic arrays of graphene disks," *IEEE J. Quantum Electron.*, vol. 51, no. 9, pp. 1–7, 2015.

[129] M. Ezawa, "Metallic graphene nanodisks: Electronic and magnetic properties," *Phys. Rev. B*, vol. 76, no. 24, p. 245415, 2007.

[130] M. Danaeifar and N. Granpayeh, "Analysis of the multi-spectral inhomogeneous metasurfaces consisting of different arrays of components," *Opt. Lett.*, vol. 40, no. 23, pp. 5666–5669, 2015.

[131] D. González-Ovejero and s. Maci, "Gaussian ring basis functions for the analysis of modulated metasurface antennas," *IEEE Trans. Antennas Propag.*, vol. 63, no. 9, pp. 3982–3993, 2015.

[132] M. A. Francavilla, E. Martini, S. Maci, and G. Vecchi, "On the numerical simulation of metasurfaces with impedance boundary condition integral equations," *IEEE Trans. Antennas Propag.*, vol. 63, no. 5, pp. 2153–2161, 2015.

[133] A. A. Salih, Z. N. Chen, and K. Mouthaan, "Characteristic mode analysis and metasurface-based suppression of higher order modes of a 2×2 closely spaced phased array," *IEEE Trans. Antennas Propag.*, vol. 65, no. 3, pp. 1141–1150, 2017.

[134] M. Kalantari, "Investigation into the behavior of metasurface by modal analysis," in *Metamaterials and Metasurfaces*. IntechOpen, 2018.

[135] P. Terekhov, V. E. Babicheva, K. V. Baryshnikova, A. S. Shalin, A. Karabchevsky, and A. B. Evlyukhin, "Multipole analysis of dielectric metasurfaces composed of nonspherical nanoparticles and lattice invisibility effect," *Phys. Rev. B*, vol. 99, no. 4, p. 045424, 2019.

[136] D. R. Smith, D. Schurig, and J. J. Mock, "Characterization of a planar artificial magnetic metamaterial surface," *Phys. Rev. E*, vol. 74, no. 3, p. 036604, 2006.

[137] C. L. Holloway, A. Dienstfrey, E. F. Kuester, J. F. O'Hara, A. K. Azad, and A. J. Taylor, "A discussion on the interpretation and characterization of metafilms/metasurfaces: The two-dimensional equivalent of metamaterials," *Metamaterials*, vol. 3, no. 2, pp. 100 – 112, 2009.

[138] C. Holloway, E. F. Kuester, J. Gordon, J. O'Hara, J. Booth, and D. Smith, "An overview of the theory and applications of metasurfaces: The two-dimensional equivalents of metamaterials," *IEEE Antennas Propag. Mag.*, vol. 54, no. 2, pp. 10–35, April 2012.

[139] Z. Kancleris, G. Slekas, and A. Matulis, "Modeling of two-dimensional electron gas sheet in FDTD method," *IEEE Trans. Antennas Propag.*, vol. 61, no. 2, pp. 994–996, Feb 2013.

[140] Y. Vahabzadeh and C. Caloz, "GSTC-based simulation of metasurfaces in finite difference techniques," in *2016 IEEE International Symposium on Antennas and Propagation (APS/URSI)*. IEEE, 2016, pp. 373–374.

[141] S. Sandeep, J. M. Jin, and C. Caloz, "Finite element modeling of metasurfaces with generalized sheet transition conditions," *IEEE Trans. Antennas Propag.*, vol. 65, no. 5, pp. 2413–2420, May 2017.

[142] S. A. Stewart, S. Moslemi-Tabrizi, T. Smy, S. Gupta *et al.*, "Scattering field solutions of metasurfaces based on the Boundary Element Method (BEM) for interconnected regions," *arXiv preprint arXiv:1812.04554*, 2018.

[143] N. Chamanara, K. Achouri, and C. Caloz, "Efficient analysis of metasurfaces in terms of spectral-domain GSTC integral equations," *IEEE Trans. Antennas Propag.*, vol. 65, no. 10, pp. 5340–5347, 2017.

[144] M. Selvanayagam and G. V. Eleftheriades, "Circuit modeling of Huygens surfaces," *IEEE Antennas Wirel. Propag. Lett.*, vol. 12, pp. 1642–1645, 2013.

[145] T. J. Smy, S. A. Stewart, and S. Gupta, "Time-domain circuit modelling of Huygens' metasurfaces," in *2017 IEEE International Symposium on Antennas and Propagation & USNC/URSI National Radio Science Meeting*. IEEE, 2017, pp. 1709–1710.

[146] S. A. Stewart, T. Smy, and S. Gupta, "Semi-analytical finite-difference technique for steady-state field characterization of space-time modulated Huygens' metasurfaces," in *2017 IEEE International Symposium on Antennas and Propagation & USNC/URSI National Radio Science Meeting*. IEEE, 2017, pp. 445–446.

[147] S. A. Stewart, T. J. Smy, and S. Gupta, "Finite-difference time-domain modeling of space–time-modulated metasurfaces," *IEEE Trans. Antennas Propag.*, vol. 66, no. 1, pp. 281–292, 2018.

[148] S. Gupta, T. Smy, S. A. Stewart *et al.*, "Floquet-mode solutions of space-time modulated Huygens' metasurfaces," *arXiv preprint arXiv:1701.05271*, 2017.

[149] S. Gupta and T. Smy, "Floquet analysis of parametric Huygens' metasurfaces," in *2017 IEEE International Symposium on Antennas and Propagation & USNC/URSI National Radio Science Meeting*. IEEE, 2017, pp. 1711–1712.

[150] T. J. Smy, S. A. Stewart, and S. Gupta, "Implicit and explicit FDTD methods for modelling EM metasurfaces," in *2018 International Applied Computational Electromagnetics Society Symposium (ACES)*. IEEE, 2018, pp. 1–2.

[151] T. J. Smy, S. Stewart, and S. Gupta, "Integrated generalized sheet transition conditions (GSTCs) in a Yee-cell based finite-difference time-domain (FDTD) simulation of electromagnetic metasurfaces," *arXiv:1706.10136*, Jun. 2017.

[152] A. Taflove and S. C. Hagness, *Computational Electrodynamics: The Finite-Difference Time-domain Method*. Artech House, 2005.

[153] M. Okoniewski, M. Mrozowski, and M. A. Stuchly, "Simple treatment of multi-term dispersion in FDTD," *IEEE Microw. Wirel. Compon. Lett.*, vol. 7, no. 5, pp. 121–123, 1997.

[154] K. Hosseini and Z. Atlasbaf, "PLRC-FDTD modeling of general GSTC-based dispersive bianisotropic metasurfaces," *IEEE Trans. Antennas Propag.*, vol. 66, no. 1, pp. 262–270, Jan 2018.

[155] Y. Vahabzadeh, N. Chamanara, and C. Caloz, "Dispersive metasurface sheet analysis using GSTC-FDTD," *arXiv: arXiv:1710.00044*, Oct. 2017.

[156] R. C. Rumpf, "Simple implementation of arbitrarily shaped total-field/scattered-field regions in finite-difference frequency-domain," *PIER B*, vol. 36, pp. 221–248, 2012.

[157] A. Z. Elsherbeni, E. Alkan, and V. Demir, *Double-Grid Finite-Difference Frequency-Domain (DG-FDFD) Method for scattering from chiral objects*. Morgan & Claypool Publishers, 2013.

[158] G. L. Erwin and E. Popov, *Diffraction Gratings and Applications*, ser. Optical Science and Engineering. CRC Press, 1997.

[159] K. Achouri and C. Caloz, "Space-wave routing via surface waves using a metasurface system," *Sci. Rep.*, vol. 8, no. 1, p. 7549, 2018.

[160] K. Yee, "Numerical solution of initial boundary value problems involving Maxwell's equations in isotropic media," *IEEE Trans. Antennas propag.*, vol. 14, no. 3, pp. 302–307, 1966.

[161] L. D. Landau, L. P. Pitaevskii, and E. Lifshitz, *Electrodynamics of Continuous Media: Volume 8*. Butterworth-Heinemann, 1984.

[162] A. Shaltout, A. Kildishev, and V. Shalaev, "Time-varying metasurfaces and Lorentz non-reciprocity," *Opt. Mater. Express*, vol. 5, no. 11, pp. 2459–2467, Nov 2015.

[163] J. Y. Dai, J. Zhao, Q. Cheng, and T. J. Cui, "Independent control of harmonic amplitudes and phases via a time-domain digital coding metasurface," *Light: Sci. Appl.*, vol. 7, no. 1, p. 90, 2018.

[164] A. A. Rukhadze and V. P. Silin, "Electrodynamics of media with spatial dispersion," *Sov. Phys. Uspekhi.*, vol. 4, no. 3, p. 459–484, 1961.

[165] J. D. Jackson, *Classical Electrodynamics*, 3rd ed. Wiley, 2012.

[166] H. M. Nussenzveig, *Causality and Dispersion Relations*. Academic Press, 2012.

[167] J. G. V. Bladel, *Electromagnetic Fields*, 2nd ed. Wiley-IEEE Press, 2007.

[168] C. J. F. Bottcher and P. Bordewijk, *Theory of Electric Polarization: Dielectrics in Static Fields*, 2nd ed. Elsevier Science, 1973.

[169] B. Gustavsen, "Computer code for rational approximation of frequency dependent admittance matrices," *IEEE Trans. Power Del.*, vol. 17, no. 4, pp. 1093–1098, Oct 2002.

[170] B. Gustavsen and A. Semlyen, "Rational approximation of frequency domain responses by vector fitting," *IEEE Trans. Power Del.*, vol. 14, no. 3, pp. 1052–1061, Jul 1999.

APPENDIX A LIST OF PUBLICATIONS

Book Chapter

- K. Achouri, **Y. Vahabzadeh**, and C. Caloz, "Electromagnetic Metasurface Synthesis, Analysis and Applications", in: Surface Electromagnetics with Applications in Antenna, Microwave, and Optical Engineering, IEEE-Wiley, (2017)

Peer-Reviewed Journal Publications

- **Y. Vahabzadeh**, K. Achouri and C. Caloz, "Simulation of Metasurfaces in Finite Difference Techniques", IEEE Trans. Antennas Propag., vol. 64, no. 11, pp. 4753-4759, Nov. (2016).
- **Y. Vahabzadeh**, N. Chamanara, and C. Caloz, "Generalized Sheet Transition Condition FDTD Simulation of Metasurface", IEEE Trans. Antennas Propag., vol. 66, no. 1, pp. 271-280, Jan. (2018).
- K. Achouri, **Y. Vahabzadeh**, and C. Caloz, "Mathematical synthesis and analysis of a second-order magneto-electrically nonlinear metasurface", Opt. Express 25, 19013-19022 (2017).
- **Y. Vahabzadeh**, N. Chamanara, K. Achouri, and C. Caloz, "Computational Analysis of Metasurfaces", in IEEE J. Multiscale and Multiphys. Comput. Techn., vol. 3, pp. 37-49, (2018).
- **Y. Vahabzadeh**, N. Chamanara, and C. Caloz, "Efficient GSTC-FDTD Simulation of Dispersive Bianisotropic Metasurface", Submitted to IEEE Trans. Antennas Propag. on Aug, (2018).
- N. Chamanara, **Y. Vahabzadeh** and C. Caloz, "Simultaneous Control of the Spatial and Temporal Spectra of Light with Space-Time Varying Metasurfaces", Accepted for publication on IEEE Trans. Antennas Propag., Early accessible on the IEEE website.
- X. Jia, **Y. Vahabzadeh** and C. Caloz, "Synthesis of Spherical Metasurfaces Based on Susceptibility Tensor GSTCs", Accepted for publication on IEEE Trans. Antennas Propag., Early accessible on the IEEE website.

Conference Papers

- **Y. Vahabzadeh**, N. Chamanara, and C. Caloz, "Simulation of Space-Time Varying Metasurface Using Finite-Difference Time-Domain Technique", Oral presentation in 2017 IEEE AP-S Symposium on Antennas and Propagation and USNC-URSI Radio Science Meeting, San Diego, California, USA, July (2017).

- **Y. Vahabzadeh**, and C. Caloz, "Field moving metasurface", Oral presentation in 2017 IEEE AP-S Symposium on Antennas and Propagation and USNC-URSI Radio Science Meeting, San Diego, California, USA, July (2017).

- C. Caloz, K. Achouri, G. Lavigne, **Y. Vahabzadeh**, L. Chen, S. Taravati, and N. Chamanara, "A guided tour in metasurface land: Discontinuity conditions, design and applications", 2017 IEEE International Conference on Computational Electromagnetics (ICCEM), Kumamoto, pp. 310-311, April (2017).

- **Y. Vahabzadeh**, K. Achouri and C. Caloz "GSTC-Based Simulation of Metasurfaces in Finite Difference Techniques", Oral presentation in 2016 IEEE AP-S Symposium on Antennas and Propagation and USNC-URSI Radio Science Meeting, Puerto Rico, USA, June (2016).

- C. Caloz, K. Achouri, **Y. Vahabzadeh**, and N. Chamanara, "Space-time metasurfaces", 2016 Photonics North (PN), Quebec City, QC, pp. 1-2, Aug. (2016).

- N. Chamanara, **Y. Vahabzadeh**, K. Achouri and C. Caloz, "Spacetime processing metasurfaces: GSTC synthesis and prospective applications", IEEE Antennas and Propagation (APS/URSI), 2016 IEEE International Symposium on. (2016).

- N. Chamanara, **Y. Vahabzadeh**, K. Achouri and C. Caloz, "Exact Polychromatic Metasurface Design: The GSTC Approach", Advanced Electromagnetic Materials in Microwaves and Optics (METAMATERIALS), 10th International Congress on. (2016).